Title
Copper Oxide by Thermal Oxidation for Electrochemical Cells and Gas Sensors

Author
Limkrailassiri, Kevin

Publication Date
2013

Peer reviewed|Thesis/dissertation

Copper Oxide by Thermal Oxidation for Electrochemical Cells and Gas Sensors

By

Kevin Limkrailassiri

A dissertation submitted in partial satisfaction of the

requirements for the degree of

Doctor of Philosophy

in

Engineering – Mechanical Engineering

in the

Graduate Division

of the

University of California, Berkeley

Committee in charge:

Professor Liwei Lin, Chair

Professor Costas Grigoropoulos

Professor Roya Maboudian

Fall 2013

Copper Oxide by Thermal Oxidation for Electrochemical Cells and Gas Sensors

Kevin Limkrailassiri

Abstract

Copper Oxide by Thermal Oxidation for Electrochemical Cells and Gas Sensors

by

Kevin Limkrailassiri

Doctor of Philosophy in Mechanical Engineering

University of California, Berkeley

Liwei Lin, Chair

Advances in electrolytic and gas sensing technologies continue to be driven by careful selection and engineering of materials. Copper oxides—both cuprous oxide, Cu_2O, and cupric oxide, CuO—are abundant, environmentally friendly, and highly versatile. An attractive feature unique to both copper oxides is the ease of synthesis through a one-step thermal oxidation of copper foil in ambient environment, yielding various oxide compositions and morphologies according to the oxidation temperature and time. There are many possible applications for the copper oxide materials, including pigments in ceramics, catalysts, sensors, solar cells, and batteries, to name a few. This work presents applications in electrochemical cells, more specifically photocatalytic water splitting and CO_2 reduction, and gas sensors.

The synthesis processes of copper oxides are characterized in terms of processing parameters and inspected with X-ray diffraction measurements and scanning electron microscope (SEM). Three kinds of copper oxides were investigated for photocatalytic testing: 1 μm-thick, and 5 μm-thick Cu_2O films *via* 0.5 hr and 10 hr oxidation at 300 °C, respectively, and a 10 μm thick film Cu_2O with 8 μm tall vertically-aligned CuO nanowire array on top *via* a 2 hr oxidation at 500 °C. Under AM 1.5 illumination, photocurrents of 0.8, 1.3, and 1.7 mA/cm^2, respectively, were recorded for these samples, exceeding the performance of previously reported as-synthesized, co-catalyst-free copper oxide photocathodes. Possible explanations for the observed performance based on increased minority carrier diffusion length and enhanced surface electric field are discussed. Future prospects of highly photoactive and stable copper oxide-based photocathodes are also explored. The effectiveness of surface passivation for the copper oxide photocathodes using pristine and hydrogenated TiO_2 thin films are quantified through prolonged photoelectrochemical testing. Photocathodes protected with TiO_2 films of 50 nm thickness deposited by atomic layer deposition exhibited excellent stability, but the photocurrent dropped to ~0.06 mA/cm^2. The results of CO_2 reduction using electrochemically reduced Cu sites from copper oxide electrodes as precursors for CO_2 reduction is also demonstrated. The proportion of reaction products H_2, CO, HCOOH, and CH_3COOH is shown to be tunable according to the surface morphology and composition of the original oxide electrode. Therefore, these electrodes exhibit the potential for highly selective liquid fuel production, including a measured H_2/CO

product ratio of ~2.6 for maximized production of liquid fuels using the Fischer-Tropsch process.

A simple gas sensing architecture taking advantage of the vertically-aligned growth of CuO nanowires is demonstrated. Complete devices are formed instantly following CuO nanowire synthesis by affixing a pair of electrode pads of a second substrate on top of the nanowire array to form a complete electrical circuit. This device architecture offers simple and facile integration of nanowires into a working device. A resistance change R/R_0 of ~6 was observed for 8.1% H_2 concentration increasing to ~26 for 25.5% H_2 concentration. Recovery time is excellent at ~0.5 min or less. A description for the formation of facile microheater-integrated devices is outlined as a promising next step. A process flow to fabricate this device along with heat transfer analysis to predict the temperature distribution in the device is provided and the power consumption may be further minimized with a proposed pulsed heating strategy.

Acknowledgements

I could never have imagined when I first entered the graduate program that my graduate school experience would turn out the way it did. The past five and a half years have been the most academically challenging years of my life. If I counted the number of times I contemplated quitting graduate school, it would almost certainly exceed the number of pages in this dissertation. This is why I believe this Acknowledgements section is integral to this work, as it directs proper thanks to all the people who supported and encouraged me these past several years. While I did learn a fair amount of engineering concepts and techniques that will serve me well in my professional career, the experience of persevering through this program with the aid of so many precious individuals is something that I will cherish for the rest of my life.

No one deserves more thanks than my adviser Professor Liwei Lin, who mentored me starting from my sophomore year of college. From then, I have been a recipient of so much of his wisdom, patience, and encouragement. Given the difficulties I experienced on an ongoing basis in my PhD research, I really think Professor Lin is the only professor who would shoulder the burden with me and continue guiding me with utmost patience. I know that my PhD really did not have to be this way, but because he faithfully led me through the most stressful junctures of the program, I am now on the brink of finally finishing. I want to thank Professor Lin from the bottom of my heart.

To Professor Dorian Liepmann, I offer heartfelt thanks. He was the chair of my Qualifying Exam committee, and through the initial 'Adjournment' decision to finally passing on my second sitting, he advised me through many long hours of chatting in his office about my research—which was not at all related to his own work—and also offered practice life advice to help me deal with test-taking anxiety. For that period of time, he treated me as if I was his own student, making himself available any time I needed to talk. It is rare to find a professor like Professor Liepmann; I know I am extremely fortunate to have worked with him even if it was only for a few months.

Special thanks go to the KAUST team: Professor Kazuhiro Takanabe, Angel Garcia, and Dr. Weili Yu. I am immensely grateful for their guidance during the most exciting and productive span of my PhD. They are a big reason my research took on very interesting directions that I would not have pursued on my own.

Hearty thanks go out to all the people I had the opportunity to work with in the LinLab. Through Dr. Brian Sosnowchik's example, I learned how to methodically approach interesting and challenging research topics. His zeal for tackling scientifically relevant problems is contagious. I am particularly grateful to Dr. Chieh Chang for allowing me the opportunity to work with him on the electrospinning project; I can confidently say that the success of this project was a major reason I considered pursuing a PhD. I shared office space with Dr. Heather Chiamori for a significant portion of my PhD, and there was no end to our constant grumbling over the state of the Cal football team. I will always remember the brainstorming sessions we had, wondering if the outlandish ideas we came up with were ever feasible. Many thanks go out to Dr. Qin Zhou and Dr. Yingqi Jiang, who were never too busy to offer all sorts of help. Their brilliance and expertise in carbon-based materials were strong motivations for me to pursue my studies with

greater diligence. Roseanne Warren and Alina Kozinda were major contributors to the projects I pursued in the latter portion of my PhD. It was a pleasure working with such talented and driven researchers.

I also want to thank my church community, more specifically all my friends in International Graduate Student Ministry of Gracepoint Church, who were family to me through all the ups and downs. I will never forget the long nights revising my Qualifying Exam PowerPoint slides with housemates who pursued unrelated research topics, yet carried the burden with me day by day leading up to the exam. They even conducted several mock exams to help me feel comfortable with getting grilled. This is in addition to the countless care packages, home-cooked meals, and prayers that I received each semester. Over and over, these acts of love came unconditionally, and they gave me a glimpse of the immensity of God's love for me. Without the presence of these brothers and sisters, my graduate school experience would have been far less meaningful. I am thoroughly undeserving of their love and care.

Lastly, I want to thank my father, mother, and brother. Pursuing graduate school in engineering meant far less frequent trips home, but through it all, I never heard them grumble. They wholeheartedly supported my studies and encouraged me to be the best that I could be. I am thankful for their boundless dreams for my life. With each of them I share the joy of finishing this graduate program.

Table of Contents

List of Figures

Chapter 1

Chapter 2

Chapter 3

Chapter 4

List of Tables

Chapter 1

Chapter 2

Chapter 3

Chapter 1: Introduction

1.1 Copper Oxide Overview

Metal oxide semiconductors are immensely attractive materials owing to their unique material properties. They are known to be earth-abundant, environmentally friendly, easy to synthesize, and cost-effective. These materials have been found to be useful for a variety of applications including catalysts,[1] sensors,[2] solar cells,[3] diodes,[4] and transistors.[5] The versatility of applications is especially applicable to copper(I) oxide, also known as cuprous oxide (Cu_2O), and copper(II) oxide, also known as cupric oxide (CuO). Recently, copper oxides have been receiving increased attention for their potential as solar cell materials with a growing number of publications.[6-8] Many techniques have been employed to synthesize copper oxide including electrodeposition,[7] electrochemical anodization,[9,10] and thermal oxidation of evaporated Cu thin films.[11] To date, only few papers report the utilization of thermally oxidized Cu foils for the aforementioned applications. This synthesis method is attractive owing to its extreme simplicity by growing copper oxides in ambient air with suitable oxidation temperature and duration to control the resulting thickness of each oxide.

1.1.1 Material Properties

Visually, the copper oxides are commonly known to exhibit the color tones as shown in the powders of **Fig. 1.1**. Cu_2O appears maroon in color, while CuO can appear dark grey or deep black. Structurally, Cu_2O takes on a cubic structure with the Cu atoms occupying the (000) positions while the O atoms occupy the (¼ ¼ ¼) positions in the unit cell. As for CuO, each Cu atom is coordinated by four O atoms in a square planar configuration. The atomic structures for both oxides are shown in **Fig. 1.2**. As semiconductor materials, Cu_2O is a *p*-type semiconductor with a direct band gap of ~2.0 eV, while CuO is a *p*-type semiconductor with an indirect band gap of ~1.4 – 1.8 eV in the bulk. The direct band gap of Cu_2O is particularly desirable for solar applications because the light absorption process involves an electron making a direct transition from the valence band to the conduction band without any change in momentum, while indirect band gaps require this momentum change with the energy coming from a phonon. Practically, this means that direct band gap semiconductors readily absorb photons and require much smaller

Figure 1.1 Visual appearance of copper(I) oxide, Cu_2O, (*left*) and copper(II) oxide, CuO, (*right*) in powder form.[12-13]

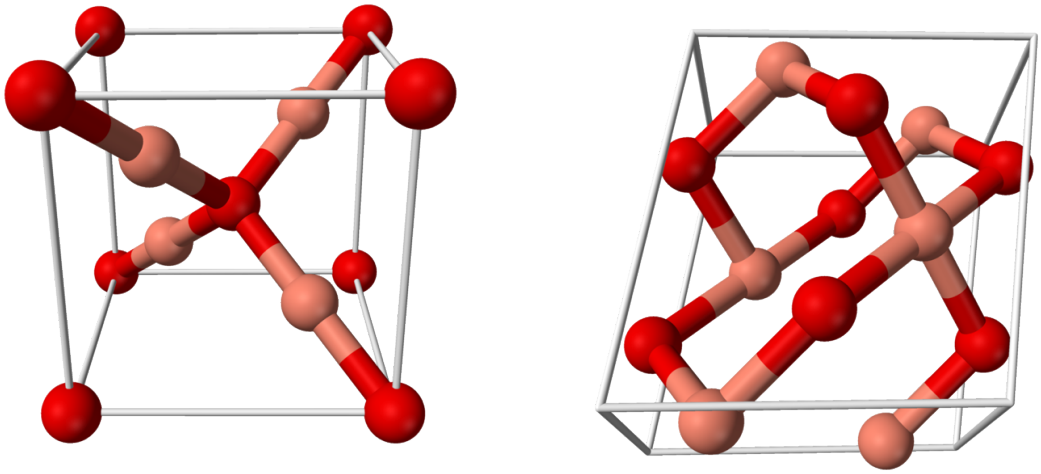

Figure 1.2 Unit cell of Cu_2O (*left*) and CuO (*right*) atomic structures, with the red atoms and pink atoms representing Cu and O, respectively. Cu_2O exhibits a cubic structure while CuO exhibits a monoclinic structure.[12-13]

thickness to absorb the same number of photons compared to indirect band gap semiconductors. This advantage, however, is paired with the disadvantage that these semiconductors more readily exhibit radiative recombination, whereas this process is more suppressed for indirect band gap semiconductors.

On the basis of the band gap energy, the theoretical maximum photocurrent under AM 1.5 illumination for Cu_2O is 14.7 mA/cm^2, corresponding to a sunlight-to-hydrogen conversion efficiency of 18%. Its conduction and valence bands straddle the water redox potentials, satisfying the requirement for driving overall water splitting. Additionally, its conduction band rests at ~0.7 V negative of the water reduction potential, providing a strong overpotential to drive hydrogen evolution. The literature reports a minority carrier diffusion length of 20-100 nm,[14] but since the absorption length is estimated to be ~10 μm,[15] it is probable that a large majority of photoexcited electrons will not be harvested before they are eliminated through recombination. Synthesizing Cu_2O in the form of nanowires is seen as a promising solution to mitigate recombination by decoupling light absorption and carrier collection.

As for CuO, although it could theoretically participate in overall water splitting as its conduction and valence bands narrowly straddle the water redox potentials, the sunlight to hydrogen conversion efficiency would be poor. The thermodynamic limit imposes a minimum band gap of 1.23 eV on the photoelectrode material, equal to the difference in energies of the water oxidation and reduction potentials, but when ohmic losses and overpotentials in the photoelectrochemical system are taken into account, the band gap should ideally be ~2.0 eV.[16] Nonetheless, CuO can participate in overall water splitting if it is combined in tandem with another semiconductor such as Cu_2O. Such a system would be beneficial in harnessing photons from two distinct wavelength regimes of the solar spectrum and separating photoexcited electron-hole pairs due to the Type-II misalignment. Moreover, the band gap of CuO is known to increase when it is synthesized in nanowire form. Kaur *et al*. measured a band gap of 2.03 eV for CuO nanowires grown *via* thermal oxidation of copper foils in the temperature range of 400

to 800 °C.[17] The nanowires ranged between 50 to 200 nm in diameter, so the increase in band gap energy is not attributed to quantum confinement effects, which are relevant in semiconductors for length scales less than 10 nm. Therefore, harnessing CuO in nanowire form may be suitable for photocatalytic water splitting. This is in addition to the obvious advantage of drastically increased surface area-to-volume ratio, which makes this material desirable not only for water splitting but also for any other applications demanding greater surface reactivity.

1.1.2 Synthesis Methods

Previous attempts to synthesize Cu_2O have largely been achieved using solution-based methods. One of the earliest attempts to evolve hydrogen from Cu_2O photocathodes used a hydrolysis method to prepare Cu_2O powder from CuCl. Vigorous stirring of Na_3PO_4 and NaCl solution yielded a yellow precipitate that was then heated at 400 °C for 24 hr and boiled in water. The powder Cu_2O photocathodes reported are the only Cu_2O-based cathodes that have ever achieved stable water splitting without the presence of passivation layers; photoactivity was maintained over a period of 1900 hr.[6] Gou *et al*. synthesized Cu_2O nanocubes through the reduction of Cu(II) salts in water with sodium ascorbate. The size of these nanocubes was tuned by altering the concentration of a surfactant.[18] A novel reduction method was employed by Wang *et al.* to synthesize Cu_2O nanowires. Solutions of NaOH and $N_2H_4 \bullet H_2O$ were added dropwise into $CuCl_2$ and PEG solution until the solution formed a blue precipitate that eventually turned red. TEM images confirmed that the resulting nanowires exhibited high crystallinity.[19] Overall, the wealth of literature reporting Cu_2O synthesis using solution-based methods confirms that these processes are well-established and reliable.

Electrodeposition is an inexpensive, low-temperature, commercially scalable synthesis technique that is also frequently used for Cu_2O growth. Switzer *et al*. deposited Cu/Cu_2O layered nanostructures in Cu(II) and lactate ion solutions with control of film thickness determined by applied current density.[9] Bohannan *et al*. synthesized similar layered nanostructures using a solution of Cu(II) sulfate pentahydrate, lactic acid, and sodium hydroxide. Control of applied current density determined not only the film thickness but also the final composition of the films in a range between pure Cu_2O and mostly Cu.[10] Electrodeposition has been a preferred method of synthesizing high quality Cu_2O, as evidenced by the recent report from Paracchino *et al*. achieving highly photoactive Cu_2O cathodes protected by oxide thin films.[7]

Several other synthesis methods for Cu_2O were also employed. High pressure sputtering was used by Taneja *et al*. to synthesize thin film nanocrystalline Cu_2O on several types of substrates. The sputtering was performed in 0.1–0.2 torr of Ar to promote collisions between the sputtered Cu atoms and residual O atoms in order to form Cu_2O nanoparticles. Particle size was controlled with stringent selection of substrate temperature, sputtering voltage, and gas pressure.[20] Figueiredo *et al*. thermally oxidized evaporated Cu thin films on glass substrates at temperatures between 100 °C and 450 °C. The oxidized thin films exhibited *p*-type or *n*-type characteristics depending on the annealing temperature.[11]

As for the growth of CuO nanomaterials, Hong *et al*. employed an alcohothermal process at various reaction temperatures to form CuO nanoparticles. Changes in the reaction temperature yielded nanoparticles with a range of diameter of 3 to 9 nm.[21] Balamurugan *et al.* produced

Cu_2O nanoparticles with sizes between 8 to 100 nm using an activated reactive evaporation process. The nanoparticles were found to be capped with a CuO surface layer to provide stabilization for large particle sizes.[22] Lastly, Borzi *et al*. milled samples of pure CuO for up to 10 hr to reduce the particle size to the range of ~9 to ~200 nm.[23]

These examples represent only a sampling of all the reports made in synthesizing Cu_2O and CuO through these particular methods. What is particularly interesting when analyzing this body of literature is the lack of attention towards device integration of oxides grown *via* thermally oxidized Cu substrates. This is likely largely attributed to the difficulty of growing large, uniform areas of copper oxide. A large stress is induced in the Cu_2O film at the completion of oxidation as the sample is returned to room temperature because of the large mismatch in the thermal expansion coefficients of Cu and Cu_2O, which are 17×10^{-6} °C^{-1} and 1.9×10^{-6} °C^{-1}, respectively.[24] When the stress in the Cu_2O film reaches a critical point as the Cu film shrinks rapidly, the Cu_2O begins to dislodge from Cu, resulting in a substrate with only patches of Cu_2O intact. Despite this synthesis challenge, copper oxides grown through this method should be highly desirable, as they would plausibly exhibit greater crystallinity as a result of the elevated synthesis temperature. Therefore, a strategy for synthesizing large areas of copper oxide films may open the possibility for enhanced performance of all copper oxide based technologies.

1.2 Copper Oxide *via* Thermally Oxidized Copper Foil

The synthesis of large, uniform areas of copper oxide was performed using starting copper substrates of 25 μm thickness. Substrates with this thickness possess sufficient pliability to relieve the stresses that develop in the oxide films during oxidation, preventing the flaking of square millimeter-sized oxide patches from the Cu foil. Initial thermal oxidation results revealed that the growth of CuO nanowires is sensitive to the pattern of air flow over the surface of the Cu foil. The CuO nanowires were grown using two methods: inside a quartz tube with closed ends within a tube furnace, and atop a hotplate. The resulting oxidized Cu foils are shown in **Fig. 1.3**. A visual comparison of the samples distinctly showed a much darker surface for the hotplate samples, suggesting excellent light-trapping capabilities afforded by the growth of dense CuO nanowire arrays. The pronounced contrast in the surface finish of the oxidized samples may be attributed to one fundamental difference in the synthesis conditions of the two processes. As no gases were transported into the quartz tube, and the temperature was uniform inside the tube furnace, it is expected that there was no bulk movement of air inside the quartz tube as the foils were oxidized. The hotplate presented a different situation: a heated surface surrounded by air at room temperature. The temperature gradient above the surface of the hotplate causes natural convection, which promotes the rising of heated air. This circulation of air above the hotplate may explain, at least in part, the distinct contrast in nanowire density on the surfaces of the samples. As air is circulated above the oxidizing Cu foil on the hotplate surface, the supply of oxygen near the Cu foil is continually replenished, providing sufficient oxygen to absorb onto the foil surface and drive nanowire growth. The furnace-grown nanowires likely experience the opposite effect: as oxygen is consumed near the Cu foil surface, the supply of oxygen is continually depleted, and growth proceeds at an asymptotic rate.

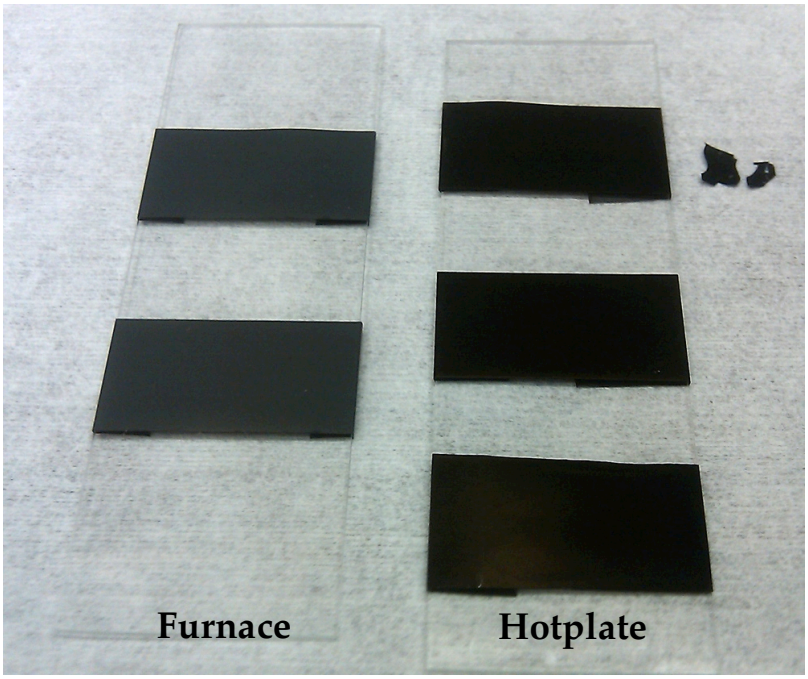

Figure 1.3 Comparison of copper oxides grown *via* thermal oxidation in a tube furnace and atop a hotplate. The CuO flakes placed adjacent to the slides are derived from thermal oxidation of thicker Cu sheets, which caused a delamination of the oxides from the Cu substrate upon cooling to room temperature. The hotplate samples yielded denser nanowire growth due to the continual replenishing of oxygen through natural convection atop the hotplate surface.

Furthermore, the average grain size of the starting Cu foil affects the density of the resulting CuO nanowire array. Cold rolled Cu foil with 99.9% purity purchased from McMaster-Carr was observed to yield less nanowire arrays compared to 99.98% purity Cu foil purchased from Sigma-Aldrich. It is known that CuO nanowire growth is largely promoted along grain boundaries, so it is possible that the expanded grains in the cold rolled Cu foil, and therefore the decreased density of grain boundaries, is responsible for the sparseness of the resulting CuO nanowires.[25] In the interest of encouraging dense CuO nanowire growth for larger surface area and enhanced catalytic properties, all experiments henceforth were performed using the 99.98% purity Cu foil from Sigma-Aldrich atop a hotplate. The thermal oxidation recipes of the three main types of copper oxide samples used for the bulk of the studies discussed in this dissertation—henceforth referred to as 'red,' 'deep red,' and 'black'—are summarized in **Table 1.1**.

Type	Oxidation Temperature (°C)	Oxidation Time (hr)	Composition
'Red'	300 °C	0.5	1 μm Cu_2O
'Deep red'	300 °C	10	5 μm Cu_2O
'Black'	500 °C	2	10 μm Cu_2O, 8 μm CuO NW

Table 1.1 Summary of thermal oxidation temperature, duration, and composition for the 'red,' 'deep red,' and 'black' samples used for the bulk of the studies discussed in this dissertation.

1.2.1 Planar Cu_2O

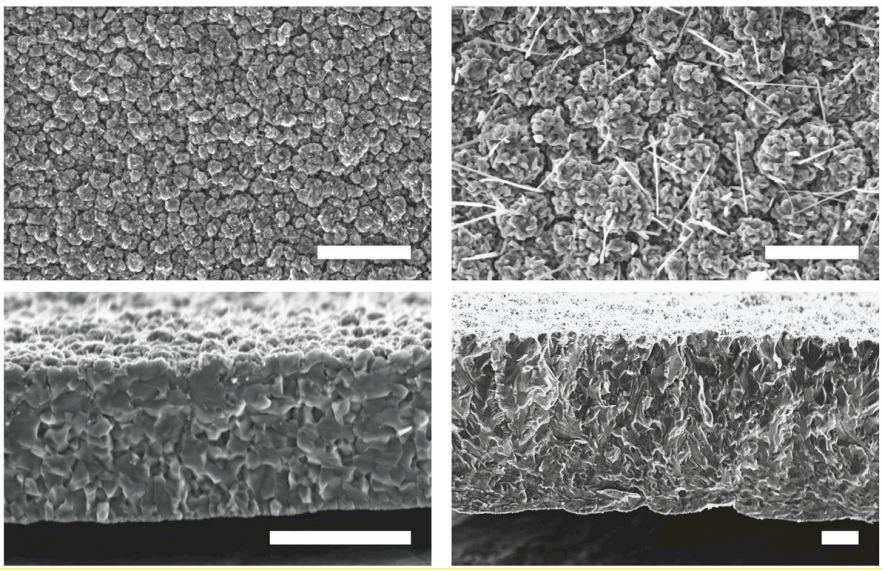

Figure 1.4 SEM micrographs of Cu foil thermally oxidized for 0.5 hr showing the top view (*top left*) and cross-sectional view (*bottom left*). Another sample was similarly oxidized for 10 hr; its top view (*top right*) and cross-sectional view (*bottom right*) are shown as well. Scale bar: 1 μm.

Thermal oxidation yielded Cu_2O films as shown in **Fig. 1.4**. Under 0.5 hr of thermal oxidation at 300 °C, the Cu foils show a coarse, granular surface with particles of size 100 to 300 nm diameter. The cross-sectional view reveals voids in between grains. This Cu_2O layer has a thickness of ~1.2 μm. Prolonging oxidation time to 10 hr extends the thickness of the Cu_2O to ~4.9 μm. These thicknesses are consistent with prior reports characterizing the growth rate of Cu_2O at 300 °C.[26] Two salient features to note are the onset of CuO nanowire growth on the surface as well as the denser packing in the Cu_2O film as observed in the cross-section. The improved crystallinity of the Cu_2O translates to improved carrier transport properties in this film. Both samples are shown detached from the underlying Cu substrate. This is explained by the mismatch in thermal expansion coefficients between Cu and Cu_2O, causing the Cu_2O film to delaminate from the Cu substrate during thermal oxidation.

1.2.2 Planar Cu_2O with CuO Nanowires

Planar Cu_2O covered with a layer of vertically-aligned CuO nanowires was formed at an oxidation temperature of 500 °C for 2 hr. A top view SEM micrograph and close-up view are shown in **Fig. 1.5.** Nanowire growth is uniformly dense across the foil surface. The nanowires have an average length of 8 μm and diameter ranging between 50 to 150 nm. As was the case for the planar Cu_2O films without CuO nanowires, the Cu_2O is delaminated from the Cu substrate due to the large thermal expansion coefficient mismatch during thermal oxidation. While this could conceivably lead to poor electrical contact for the resulting photocathode, the active areas used for photoelectrochemical testing were large enough to ensure sufficient physical contact for low resistance, ohmic contact between the Cu substrate and Cu_2O film. The SEM micrograph of

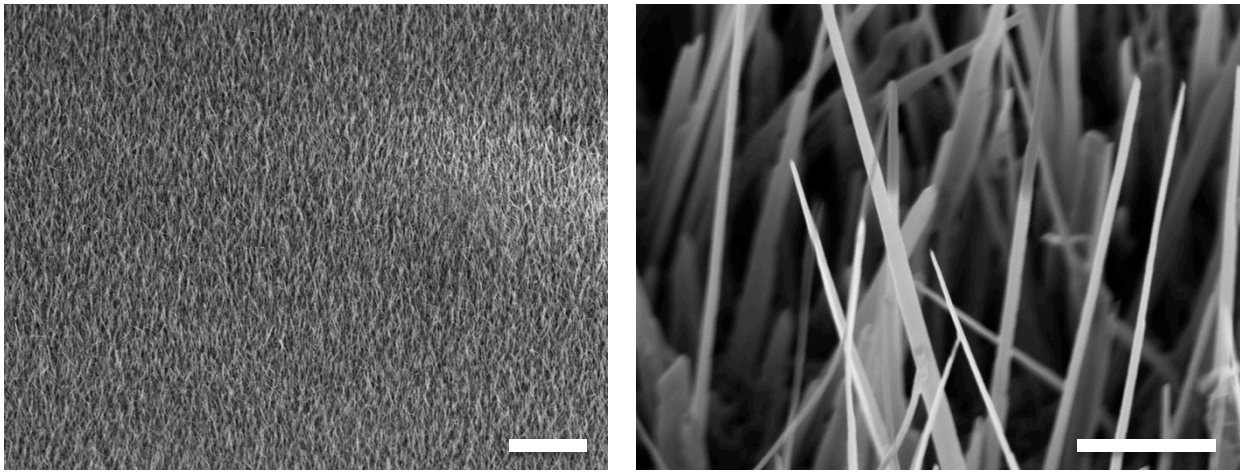

Figure 1.5 SEM top view micrograph of a Cu foil oxidized at 500 °C for 2 hr (*left*). Nanowire growth is uniformly dense across the surface. Scale bar: 20 μm. A close-up of the nanowires reveals a rectangular cross-section (*right*). The nanowires average 8 μm in length and range between 50 to 150 nm in diameter. Scale bar: 1 μm.

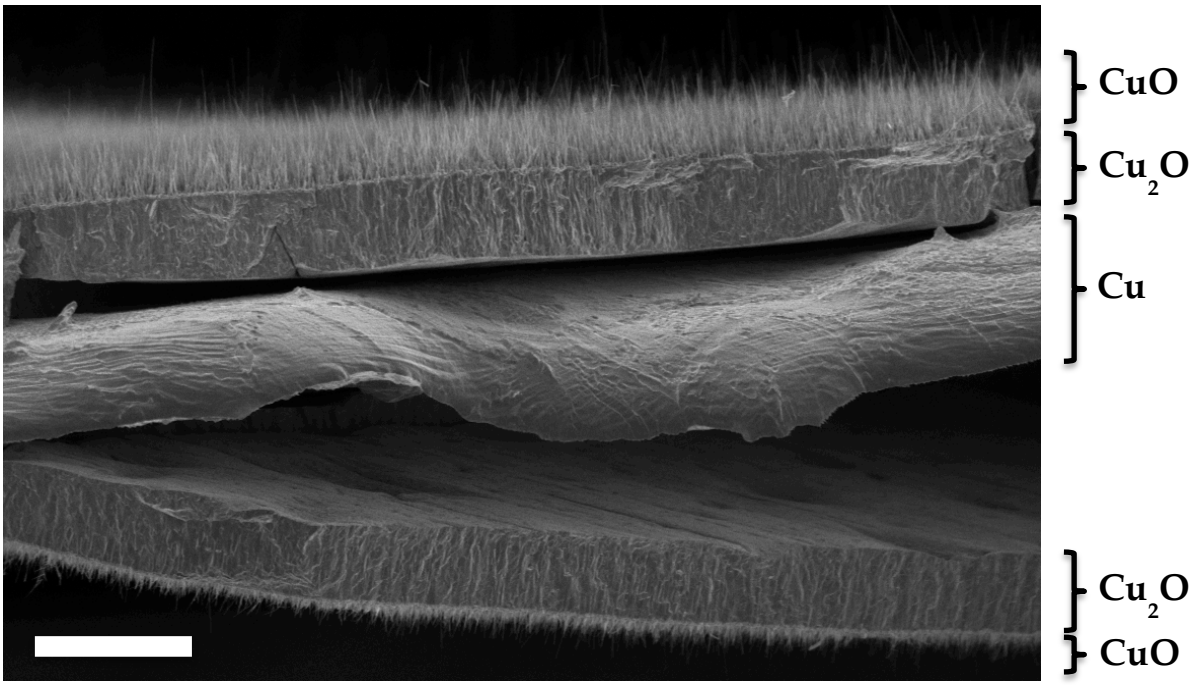

Figure 1.6 SEM micrograph of a full cross-section of an oxidized Cu foil. Both Cu_2O and CuO were grown on opposite faces of the foil. The asymmetric growth is attributed to unequal availability of oxygen between the top and bottom surfaces. Scale bar: 20 μm.

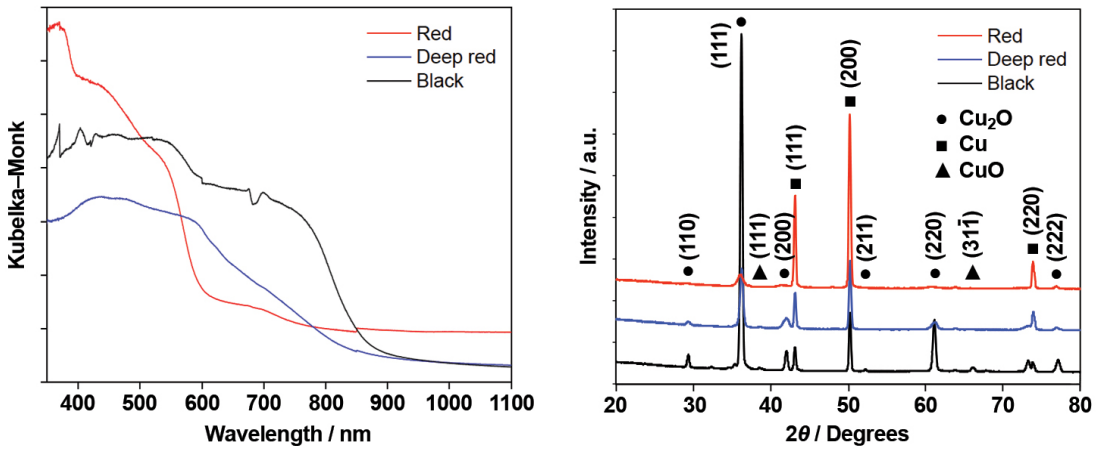

Figure 1.7 UV-Vis absorption spectra derived from the Kubelka-Monk function (*left*) and *x*-ray diffraction pattern (*right*) for the 'red,' 'deep red,' and 'black' samples.

Fig. 1.6 shows the cross-section of a Cu foil with oxidation occurring both on the top and bottom surfaces. Notably, the Cu_2O layers seem to be of identical thickness, but the top CuO nanowires appear to be longer than those on the bottom surface. Since the foil is wrapped tightly around microscope slides, the bottom surface is not freely exposed to air as is the top surface. One very plausible explanation, then, for the difference in average CuO nanowire length between the top and bottom surfaces is the depletion of oxygen supply on the bottom side of the foil during thermal oxidation. When one O atom is needed for every two Cu atoms to form Cu_2O, the oxygen supply on the back surface is still sufficient to allow Cu_2O to proceed at the same rate as on the top surface, but when two O atoms are needed for every two Cu atoms to form CuO above the Cu_2O layer, the enclosed space near the back surface does not provide enough O atoms for CuO nanowire growth to proceed at the same rate as on the top surface. Consequently, the CuO nanowires grow to shorter lengths on the back surface.

UV-Vis diffuse absorption spectra derived from the Kubelka-Munk method are shown in **Fig. 1.7**, providing band gap energy estimates of ~2.0 eV, ~1.4 eV, and ~1.4 eV for the red, deep red, and black samples, respectively. The black sample shows a downward trend that is steeper than the slope of the deep red sample even though Cu_2O is a direct band gap semiconductor and CuO is an indirect band gap semiconductor. The direct band gap properties of the black sample may be caused by the enhanced light-trapping properties of the CuO nanowire array. Compared to the deep red and black samples, the red sample is more highly absorbing at both short and long wavelengths. This may be explained by the presence of a thicker underlying Cu layer due to a shorter oxidation time. Cu is reflective at long wavelengths, and therefore photons can be given additional opportunities to be absorbed by Cu_2O upon reflection from the Cu layer. At short wavelengths, Cu is absorptive, so the large Kubelka-Monk function can be attributed to absorption by both Cu_2O and Cu.

The weak CuO signals in the XRD pattern of **Fig. 1.7** despite the highly dense growth of CuO nanowires is attributed to the presence of a much thicker and space-efficient Cu_2O layer. As expected, the XRD peaks show the shortening of Cu signals and heightening of Cu_2O signal while transitioning from red to deep red to black samples. This is in accord with increased Cu

consumption and conversion to Cu_2O with increasing oxidation time and temperature. The sharp Cu_2O (111) peak, the tallest of all the Cu_2O signals, suggests that the Cu_2O layer is highly crystalline.

1.3 Dissertation Overview

The synthesis and characterization of high-quality copper oxide films by thermal oxidation of Cu foil is the fundamental technology used in this dissertation and **Figure 1.8a** shows typical synthesis results from the direct oxidation of Cu films. The applications of copper oxide for electrocatalysis and gas sensing are detailed in **Chapter 2** and **Chapter 3**, as illustrated in **Figs. 1.8b & c,** respectively. In the area of photocatalytic water splitting, both planar Cu_2O

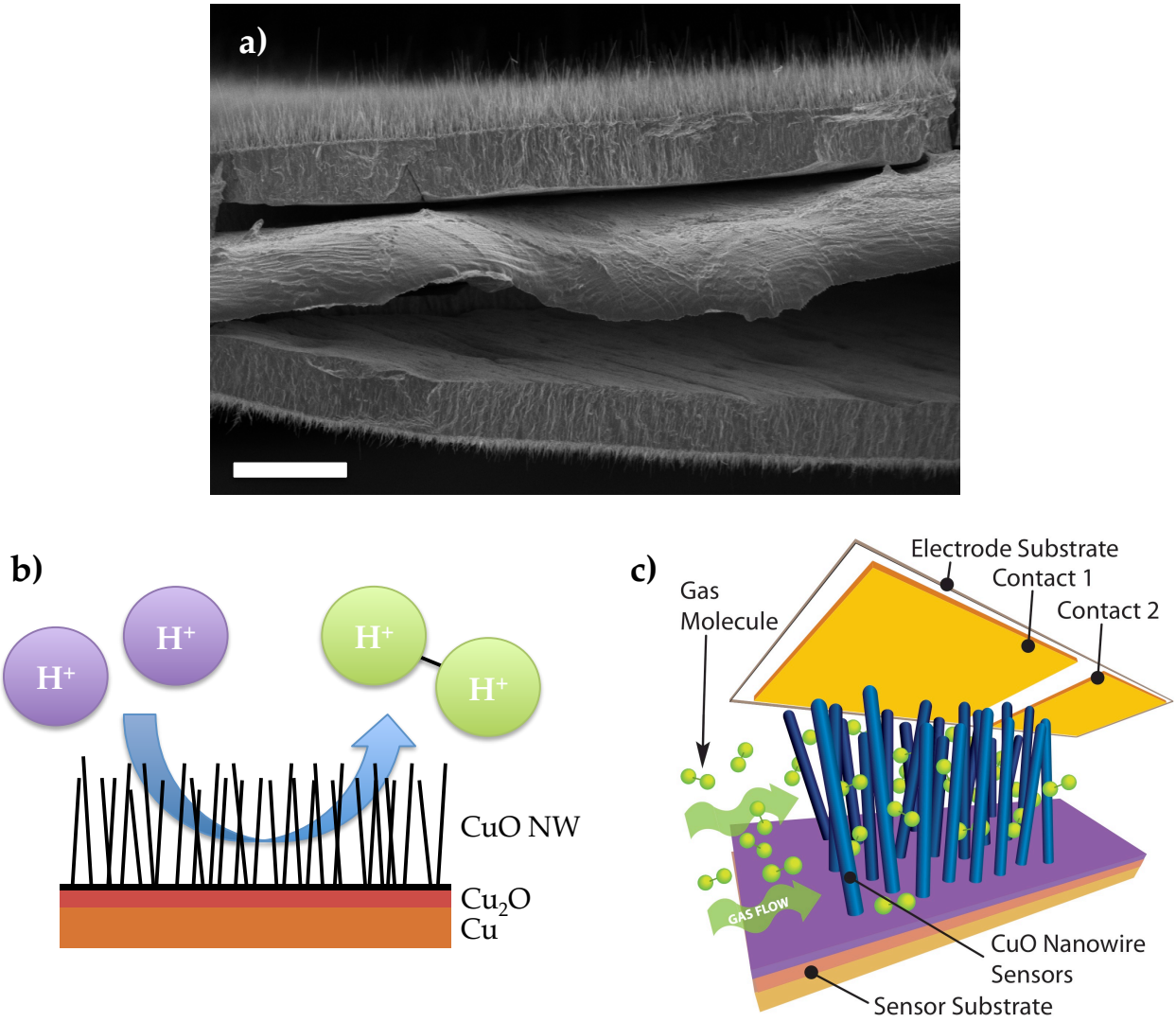

Figure 1.8 **(a)** SEM cross-sectional micrograph of copper oxides grown *via* one-step thermal oxidation of Cu foil in air. Copper oxides prepared in this manner are useful for **(b)** electrocatalysis as well as **(c)** gas sensing. Scale bar: 20 μm.

photocathodes and planar Cu_2O with CuO nanowire photocathodes are studied, and interesting photocurrent results are discussed in light of the high crystallinity and large carrier concentration of the copper oxide films. These results provide useful future studies in developing highly photoactive and stable copper oxide photocathodes for water splitting. Copper oxide electrodes can also be used as precursors to Cu driven lysis of CO_2 through the electrochemical reduction of copper oxide. The oxidation conditions for the copper oxides dictate the proportion of H_2, CO, HCOOH, and CH_3COOH formed during CO_2 reduction. The flexibility in product formation to be further described in this dissertation means that these electrodes can be designed to preferentially favor the production of certain liquid fuel products. On the other hand, possible sensing applications for copper oxides are also investigated. CuO nanowire based H_2 sensors with facile top contacts are assembled and tested in this work. This device architecture is a new device paradigm that takes advantage of highly sensitive nanowires without many of the laborious, fabrication intensive techniques of existing nanowire based devices. The diversity of these applications lends credence to the highly versatile nature of this material.

The dissertation is organized in four chapters to describe the research and development efforts. **Chapter 1** briefly introduces and motivates the use of copper oxide. The basic synthesis process and characterizations of both Cu_2O and CuO structures are described, with attention directed to surface morphology and elemental composition. These copper oxides are the active material of the electrocatalysis and gas sensing work described in the subsequent chapters.

In **Chapter 2**, the application of copper oxide for photocatalytic water splitting and CO_2 reduction is discussed. An overview of previous work on metal oxide semiconductors for water oxidation and water reduction is provided. The specific material properties of copper oxide that render it a desirable material for water splitting are briefly outlined. The materials and techniques used for copper oxide growth and characterization are described. Growth results detailing the composition of the oxide films are displayed, along with corresponding photoelectrochemical results for planar Cu_2O, planar Cu_2O with CuO nanowires, and finally planar Cu_2O with CuO nanowires protected by TiO_2. The significance of the large photocurrent observed during photoelectrochemical testing is discussed at length and preliminary results for Cu_2O–H:TiO_2 core-shell nanowire photocathodes is provided. The application for CO_2 reduction is also investigated. An overview of the technological challenges in this field is provided along with a short summary of recent work using Cu_2O for CO_2 reduction. Following a brief description of the techniques used to quantify CO_2 reduction activity, chronoamperometry data is provided to show the electrochemical reduction history of Cu_2O to reveal Cu sites for CO_2 lysing. The proportions of CO, H_2, HCOOH, and CH_3COOH produced are provided in detail, and prospects for syngas conversion to liquid fuels are discussed.

In **Chapter 3**, the application of copper oxide for gas sensing with facile contact integration is detailed. The challenges of assembling nanowire-based gas sensors surmounted by this technology are discussed. Following an analysis of the optimal number of nanowires to be connected for sensitive operation, the experimental procedure is described. Resistance data in response to increasing H_2 concentration is provided, and a concluding analysis that details potential sensitivity improvement based on the number of connections is given.

The significance of the results for each technology is summarized in **Chapter 4**. Future research directions are proposed for the characterization of the electrical properties of Cu_2O as a function of thermal oxidation conditions as well as Cu_2O photocathodes protected by graphene for stable and efficient hydrogen evolution.

Chapter 2: Copper Oxide for Electrochemical Cells

2.1 Photocatalytic Water Splitting

2.1.1 Motivation

Solar energy presents an attractive alternative to continued reliance on the combustion of fossil fuels to meet current global energy demands. Growing concern over greenhouse gas emissions and the depleting fossil fuel supply have accelerated and focused the search for clean, renewable energy sources. Among all the available renewable energy technologies, solar is by far the most promising owing to the quantity of power incident on the surface of the Earth from the sun, an estimated 120,000 Terawatts. This far surpasses the power consumption of the global population in 2011—15 TW. This number is expected to increase to 30 TW by 2050. In comparison, geothermal, biomass, wind, and hydroelectric energy sources can theoretically contribute only about 12, 10, 4, and 2 TW, respectively.[27, 28]

In spite of the stratospheric promise of solar energy, it continues to be an insignificant player in the current renewable energy landscape. According to the U.S. Energy Information Administration, solar generated less than 1% of all renewable energy in the United States in 2012.[29] The mismatch in the potential and current realization of solar energy is strongly attributed to the difficulty of harnessing solar energy affordably. Silicon remains as the workhorse of photovoltaic innovation, but advances in silicon photovoltaic technology are yielding only diminishing returns due to the inherent need for expensive, high-quality, defect-free silicon for high solar energy conversion efficiency. For solar to maintain its position as a promising renewable energy technology to meet the world's future energy needs, exploring other potential materials for energy harvesting is needed.

Compounding this challenge is the heavily climate-dependent availability of solar energy. Regions that receive intermittent sunshine will require a means of harnessing sunlight and storing it for use during the nighttime and when the sun is obscured by overcast conditions. This challenge can be addressed through solar water-splitting, a photocatalytic reaction that converts water to hydrogen and oxygen gas. The stored hydrogen fuel can then be burned at a later time for use as electricity. This combustion process releases water vapor as a byproduct and produces no carbon emission. The added benefit of solar water-splitting over traditional photovoltaics—storable energy in the form of hydrogen fuel—does not come without cost. Solar water-splitting places much more stringent demands on the material properties of the active material compared to photovoltaics, which explains why the efficiencies of state-of-the-art photoanodes for solar hydrogen production have only begun to exceed 5%,[30] whereas commercial silicon-based photovoltaics are approaching 20%. In addition to the requirements of photosensitivity to the solar spectrum and efficient charge separation and transport, water-splitting demands that the conduction and valence bands of the semiconductor straddle the reduction and oxidation potentials of water. Practically speaking, the photoelectrode must also withstand prolonged exposure to sunlight while submerged in an electrolyte, so the semiconductor must be resistant to photocorrosion. For the case of photoanodes, this means that the thermodynamic oxidation potential of the semiconductor should lie below either its valence band maximum or the water

oxidation potential. For the case of photocathodes, the opposite is true: the thermodynamic reduction potential should lie above either its conduction band minimum or the water reduction potential. Added to this is yet another requirement that the semiconductor surface be populated with an abundance of catalytically active sites. This is usually induced through co-catalyst nanoparticle islands deposited on the surface of the semiconductor photoelectrode. Finally, the semiconductor material must be earth-abundant and synthesized in a cost-effective manner. Given the laundry list of requirements to be satisfied in the design of an ideal photoelectrode material, it is understandable that there is much work to be done in this field. The study of copper oxide-based photocathodes, the focus of this chapter, is an endeavor in the search for this ideal material.

2.1.2 The Photoelectrochemical Cell

Photoelectrochemical water splitting can be divided into three fundamental processes: light absorption, charge separation, and charge transfer. These processes will now be described separately, in the order that these processes take place from the moment a photon is absorbed by the semiconductor to the formation of a molecule of H_2.

The electronic band structure of a semiconductor dictates the nature of light absorption occurring in the material, which has implication on the thickness of material needed to absorb a certain quantity of photons. If a photoexcited electron requires only a change of energy in transitioning from the valence band to conduction band with no change in momentum, the semiconductor is regarded as a direct band gap semiconductor. Otherwise, a semiconductor that requires an additional change in momentum is known as an indirect band gap semiconductor. This momentum change is the reason that indirect band gap semiconductors such as Si have an absorption length of 1 mm near its band gap energy. As a long absorption length implies the need for greater material consumption for absorption, a wealth of literature has been devoted to exploring micro- and nano-texturing strategies to promote enhanced light-trapping in thin-film solar cells. Direct band gap semiconductors, in contrast, can more readily absorb photons to generate electron-hole pairs.

The photoexcited electron-hole pair must now be spatially separated to prevent the occurrence of radiative recombination. This can be done in the presence of an electric field, which is formed in the semiconductor near the semiconductor-electrolyte interface. Taking the example of a semiconductor photocathode, the relative positions of the water reduction potential and Fermi level of the semiconductor cause a bending of the conduction and valence bands as illustrated in **Fig. 2.1**. Electrons and holes generated in this depletion region are directed into opposite directions through electric field induced carrier drift. Electron-hole pairs may also be photoexcited in the semiconductor bulk, but carrier transport occurs only through the random-walk mechanism of carrier diffusion. Along with radiative recombination, Shockley-Read-Hall recombination, which occurs at defect sites in the crystal lattice, and Auger recombination, a process commonly observed at high carrier concentrations, are also causes of carrier annihilation.

A long minority carrier diffusion length ensures that the electron transfers safely through the semiconductor toward the semiconductor-electrolyte interface. This value can be as large as

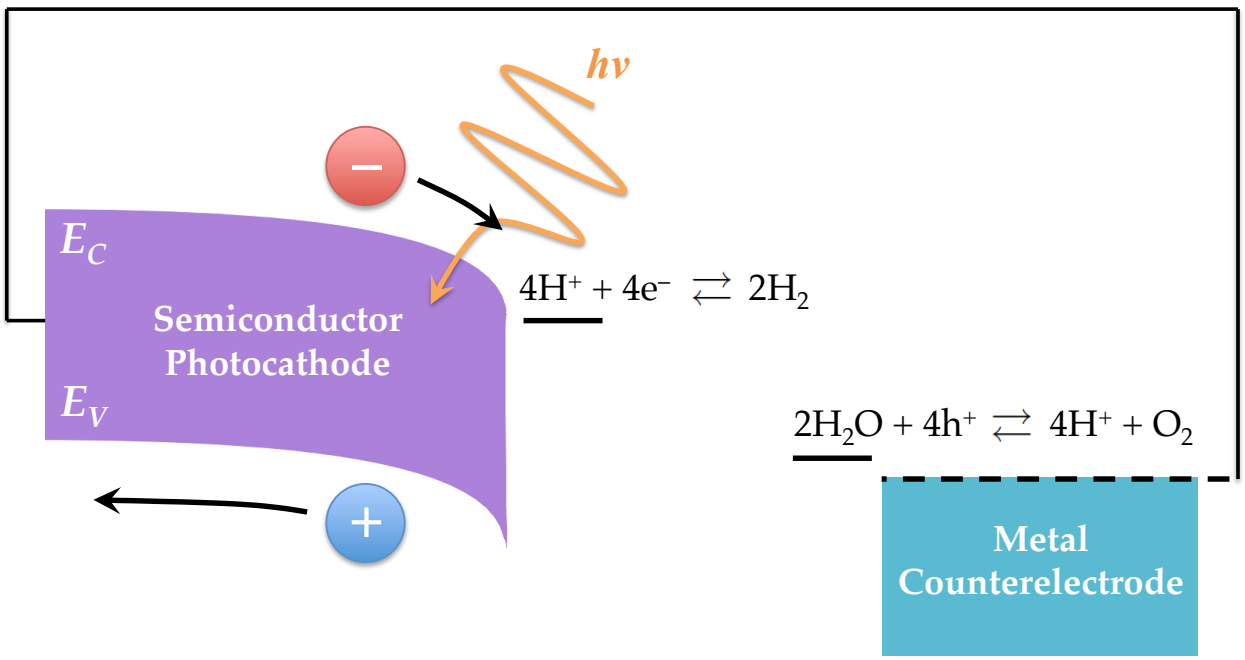

Figure 2.1 Schematic of a basic two electrode setup showing the working electrode, counterelectrode, and the relative positions of the water oxidation and reduction reactions. Electrons and holes are separated by the electric field in the depletion region. Holes are transported to the counterelectrode and participate in the water oxidation reaction there. Meanwhile, electrons participate in the water reduction reaction at the semiconductor photocathode.

30 μm for single crystalline Si but only several tens or hundreds of nanometers for metal oxides.[31] From there, a semiconductor surface with strong catalytic activity is required to shuttle the electron into the electrolyte. Among the metal oxides, TiO_2 is especially known to possess highly catalytic surfaces suitable for water-splitting, while most other semiconductors require the aid of a co-catalyst to enhance surface reactivity.

For a photocathode immersed in an acidic electrolyte, electrons transported from the semiconductor react with excess protons in the electrolyte to form hydrogen molecules according to **Eq. 2.1**:

$$4H^+ + 4e^- \rightleftarrows 2H_2 \qquad \textbf{(2.1)}$$

Meanwhile, holes travel through the back contact toward the counter electrode in the photoelectrochemical cell, where they react with hydrogen molecules to oxidize water and form protons according to **Eq. 2.2**:

$$2H_2O + 4h^+ \rightleftarrows 4H^+ + O_2 \qquad \textbf{(2.2)}$$

These processes are possible because the water redox potentials are straddled by the semiconductor valence and conduction bands, and therefore these reactions are energetically favored. This is true of both copper oxides, Cu_2O and CuO, as illustrated in **Fig. 2.2**.

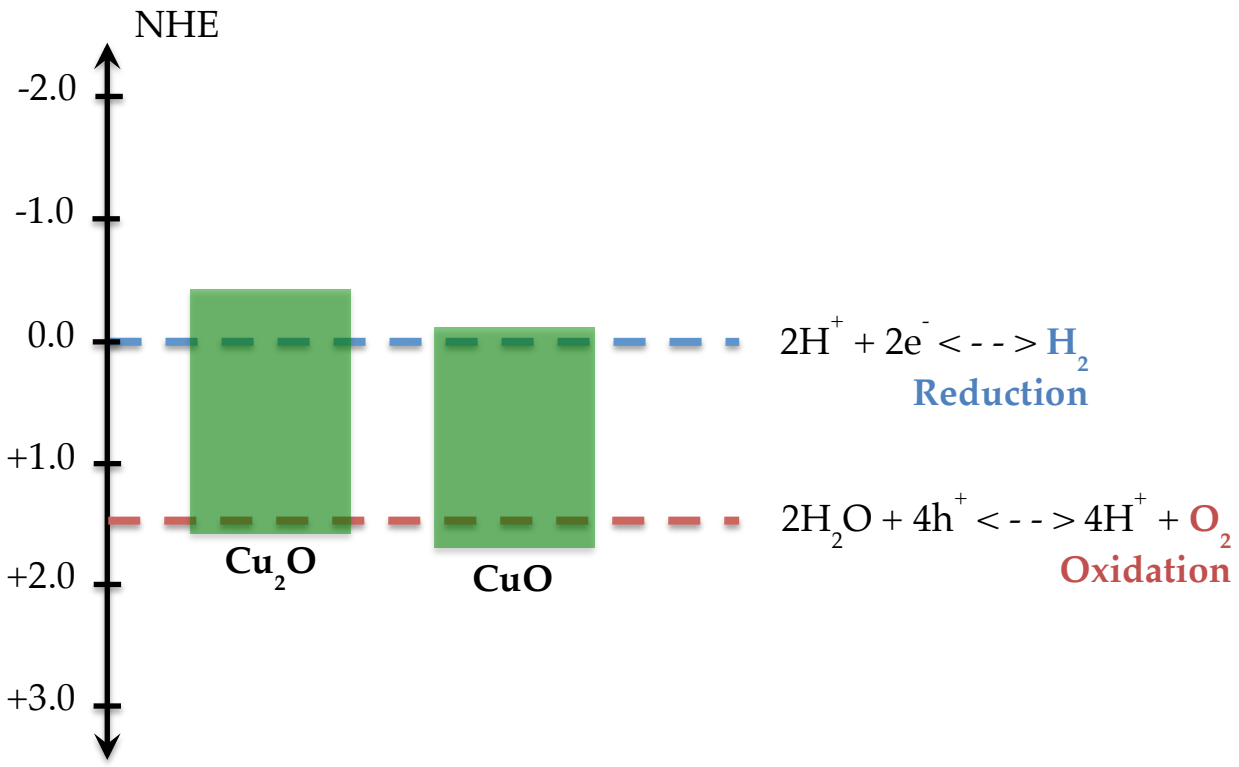

Figure 2.2 Electronic band gap positioning for Cu_2O and CuO relative to the water redox potentials on the NHE scale. Both band gaps straddle the water redox potentials, making them suitable for overall water splitting.

A standard photoelectrochemical setup is depicted in **Fig. 2.3**. This setup features an H-cell with two compartments, one for both the working and reference electrodes, and the other for the counter electrode. The compartments are partitioned by a permeable membrane to maintain an electrically conductive path between the cells while separating evolving hydrogen and oxygen gases. The gas is transported through the ports and collected in a gas chromatograph for gas volume measurement. To ensure replenished supplies of water molecules and protons near the counterelectrode and working electrodes, respectively, the electrolyte in each cell is agitated with a magnetic stir bar. For tests requiring illumination, simulated sunlight is directed at the working electrode through a quartz window on the side of the cell. All three electrodes are connected to a potentiostat for data acquisition and analysis.

2.1.3 Current Outlook

Metal oxide semiconductors are an attractive materials system considering the need for photoelectrodes composed of earth-abundant materials and produced with scalable processing methods. By far, the well-studied metal oxides is TiO_2, which is known to be highly stable and non-corrosive, possess highly catalytic surfaces, and exhibit long electron-hole pair lifetime. Liu *et al.* reported a photocurrent of ~2.8 mA/cm^2 for a TiO_2 nanowire photoanode containing mixed anatase and rutile phases,[32] and Wang *et al.* employed a simple hydrogenation process to raise the photocurrent of their TiO_2 nanowire arrays to ~2.5 mA/cm^2.[33] The perennial challenge of

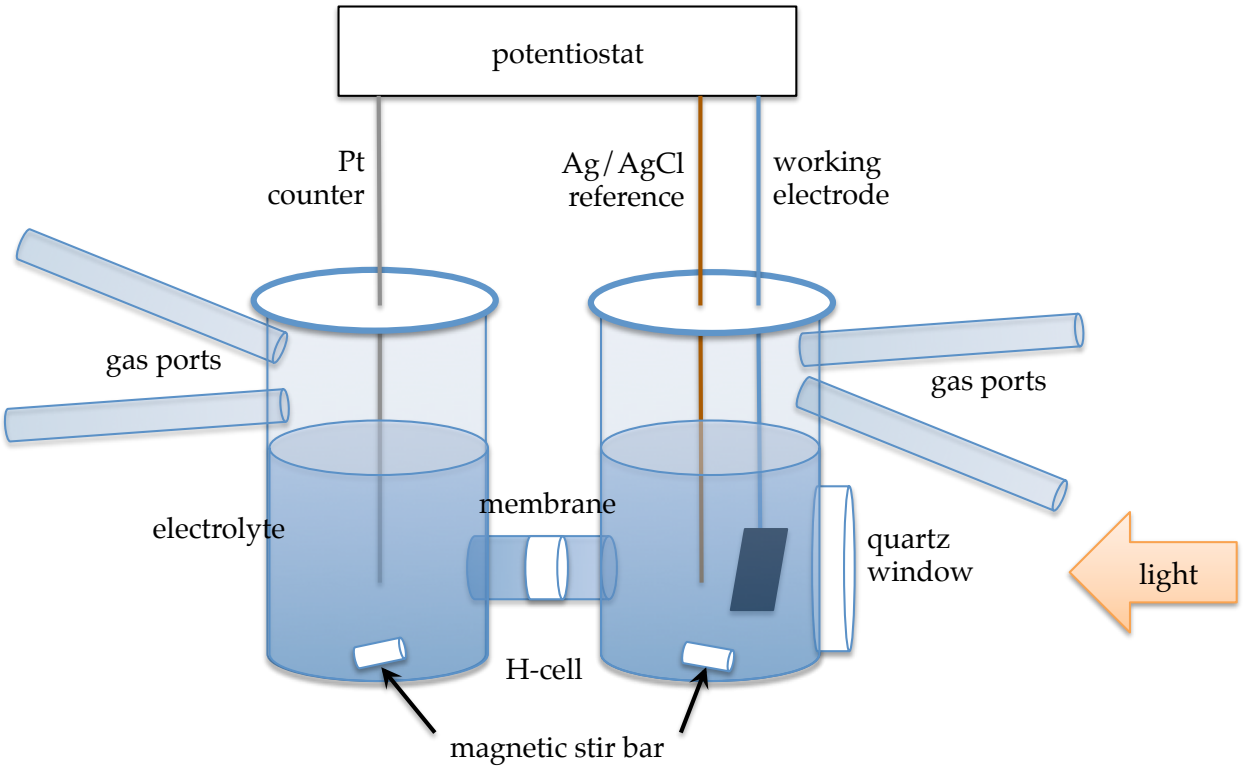

Figure 2.3 A typical three electrode photoelectrochemical cell featuring a working electrode, counter electrode, and Ag/AgCl reference electrode. The membrane separates O_2 and H_2 gas products but is porous enough to allow an electrically conductive path through the electrolyte between the two cells. Gas ports allow the collection of gas products by a gas chromatograph. Magnetic stir bars agitate the electrolyte and replenish the supply of reactants on the surface of the electrodes.

TiO_2 centers on the improvement of its sensitivity to the visible range, as its large band gap energy of ~3.2 eV allows for the absorption of photons primarily in the ultraviolet range, as well as rapid recombination of electron-hole pairs. Other well-studied metal oxides include ZnO and WO_3, but these materials face similar challenges due to their large band gap energies. A promising alternative is hematite, α-Fe_2O_3, which has a more favorable band gap of ~2.0 eV. Recently, Kim *et al.* achieved a sunlight-to-hydrogen conversion efficiency of 5.3% using single-crystalline, nanostructured hematite photoanodes doped with Pt and modified with cobalt phosphate as co-catalyst on the surface. This conversion efficiency is the highest ever reported for oxygen evolving photoanodes.[30] Fast recombination and short hole diffusion length are seen as the primary barriers limiting the performance of hematite photoanodes.[16] Another well-studied material is $BiVO_4$, which is also sensitive to visible light, but as its conduction band lies just positive of the water reduction potential, it cannot participate in overall water splitting without the aid of surface modifications, doping, or an additional semiconductor acting in tandem.[34]

2.1.4 Experimental Setup

The procedure for assembling thermally oxidized Cu_2O photocathodes is as follows. Copper foil of 25 μm thickness and 99.98% purity obtained from Sigma-Aldrich was cut into coupons of size 1 cm × 2.5 cm. These coupons were then tightly wrapped around glass microscope slides as illustrated in **Fig. 2.4** and placed atop a hotplate set at 300 °C for 0.5 ('red') and 10 hr ('deep red'). The same procedure is followed for obtaining CuO nanowires atop a planar film of Cu_2O, except that the hotplate temperature is 500 °C for a duration of 2 hr ('black'). At the end of the oxidation period, samples were removed from the hotplate and returned to room temperature on a chilling plate. Oxides are formed both on the top and bottom faces of the microscope slide. Following oxidation, the samples are analyzed in a Siemens D5000 x-ray diffractometer to confirm the elemental composition of the oxides. Low-resistance ohmic contacts are formed by mechanically abrading the oxide on the bottom side of the slide to reveal the underlying Cu layer, applying silver paste on the exposed Cu, and attaching an electrical wire with epoxy. The rest of the foil except for an active area of ~1 cm^2 was also covered with epoxy to complete the assembly of the photocathode.

Samples with protective TiO_2 thin film were inserted into a Picosun atomic layer deposition reactor prior to mechanical abrasion and electrical wire attachment. The TiO_2 film was deposited at a temperature of 275 °C and a pressure of 10 hPa with alternating pulses of water and titanium tetraisopropoxide precursor. Each cycle deposited approximately 0.25 Å of TiO_2.

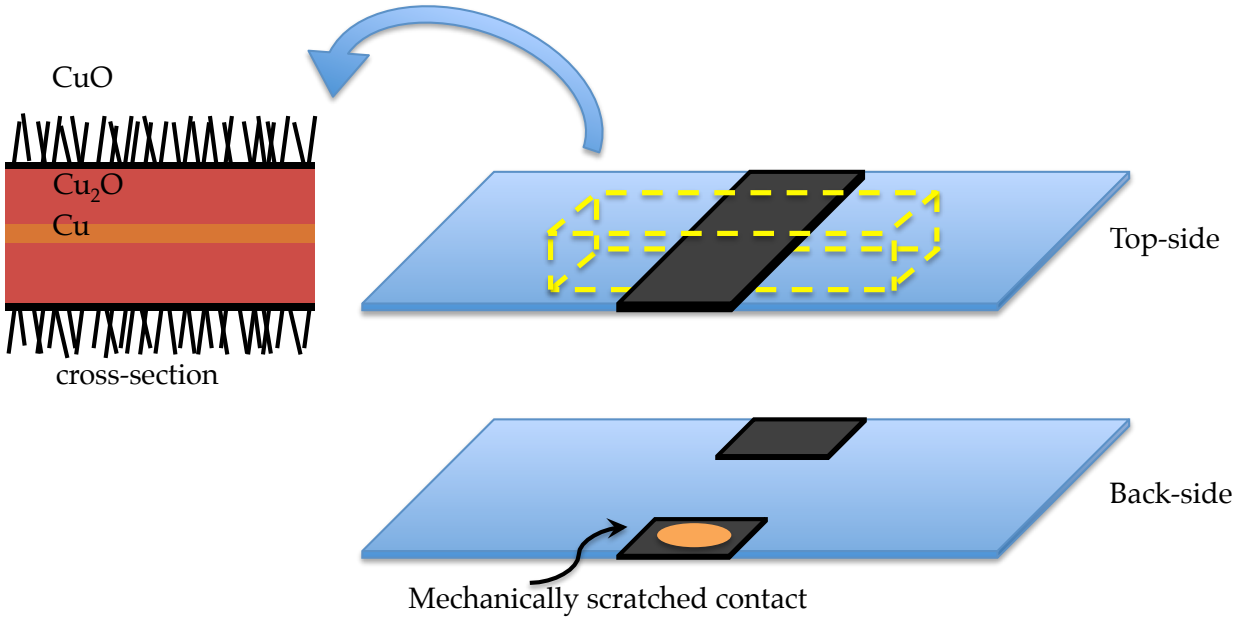

Figure 2.4 Illustration of photocathode assembly consisting of a Cu foil wrapped tightly around a microscope glass slide. Cu is exposed on the backside of the oxidized foil through mechanical abrasion to allow for the attachment of electrical wire. A cross-section of the oxidized foil showing distinct Cu_2O and CuO films is also illustrated.

Photoelectrochemical testing was performed in a three-electrode configuration consisting of the copper oxide photocathode as the working electrode, Pt wire as the counterelectrode, and Ag/AgCl in saturated KCl as the reference electrode. The electrolyte was 1 M Na_2SO_4 buffered at pH 4.9. The photocathode was subjected to chopped 100 mW/cm^2 AM 1.5 illumination from a Peccell PEC-L15 Solar Simulator, and the spectral light intensity was confirmed with an Eko Instruments LS-100 spectroradiometer. The scan rate for linear sweep voltammetry and cyclic voltammetry was fixed at 10 mV/s. All data was acquired and analyzed with a Gamry Reference 3000 potentiostat.

2.1.5 Results

2.1.5.1 As-grown Copper Oxide

Photoelectrochemical current as a function of applied bias for red, deep red, and black samples along with photocurrent average and standard deviation specifically at applied biases of 0 V and 0.26 V *vs.* RHE is shown in **Fig. 2.5**. At zero bias, the photocurrent for the red and deep red samples are ~0.8 and ~1.3 mA/cm^2, respectively. The onset potential of ~0.5 V matches well with the Cu_2O conduction band positioning relative to the water reduction potential. The photocurrent values are remarkably high in comparison to published work reporting values under 0.3 mA/cm^2.[35, 36] Another report from Paracchino *et al.* measured photocurrents of only several microamperes per square centimeter for 1.3 μm thick electrodeposited Cu_2O films and observed a thousandfold photocurrent increase after Pt co-catalysts were electrodeposited on the surface.[7] Placed in this context, the red and deep red samples made of mainly Cu_2O perform exceptionally well. The black samples also fare well, reaching a photocurrent of ~1.7 mA/cm^2 and surpassing a previous report of copper oxide composite photocathodes obtaining a photocurrent of 1.54 mA/cm^2.[37]

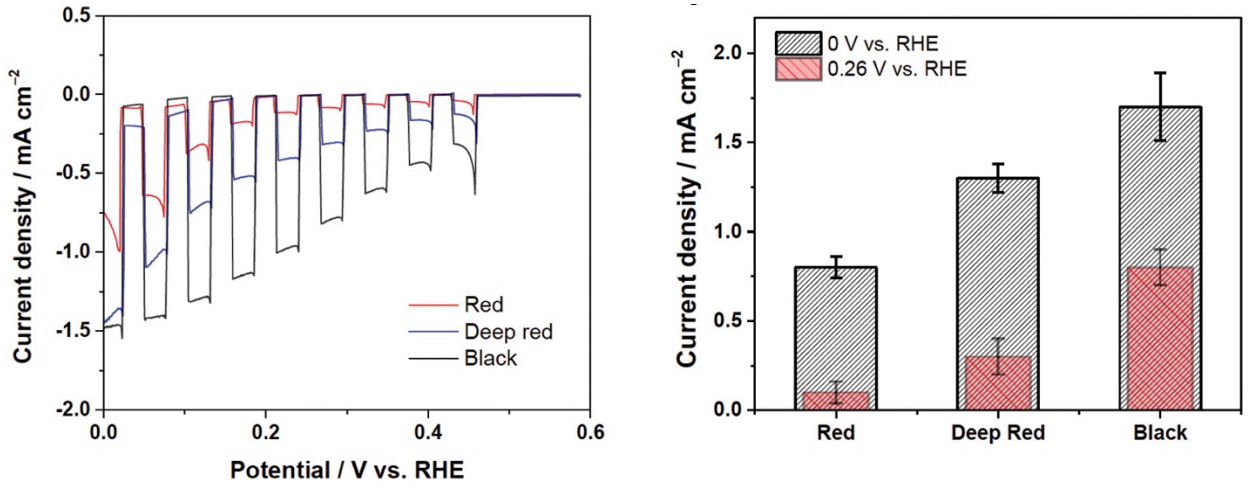

Figure 2.5 Photoelectrochemical current for red, deep red, and black samples immersed in Na_2SO_4 electrolyte buffered at pH 4.9 and subjected to 100 mW/cm^2 AM 1.5 illumination (*left*), and a comparison of photocurrent average and standard deviation for each sample at biases of 0 V and 0.26 V *vs.* RHE (*right*).

It should be noted, however, that most groups do not report gas chromatograph data showing hydrogen and oxygen gas evolution over time. This is a more direct indicator of photoelectrochemical water splitting performance compared to photocurrent because Cu_2O is prone to corrosion in acidic environments, which is caused by photogenerated free carriers reducing Cu_2O to Cu. This means that the photocurrent data will tend to inflate the water splitting capability of Cu_2O because a portion of the carriers are lost towards the reduction of Cu_2O. Unfortunately, gas chromatograph measurements were attempted for the red and deep red samples to no avail. The significance of the large photocurrent values for these samples will be further discussed in **Chapter 2.1.6.1**.

The standard deviation values shown in **Fig. 2.5** highlight the excellent photocurrent reproducibility of the Cu_2O photocathodes. The standard deviation is less than ~0.4 mA/cm^2 for all samples at 0 V. and 0.26 V. *vs*. RHE. An ongoing concern of powder-based photoelectrodes, which are promising due to their low-cost and ease of synthesis, is the difficulty in controlling the bulk electronic properties of the photoelectrode from sample to sample.[38] These Cu_2O photocathodes are therefore an attractive alternative for cost-effectiveness, ease of synthesis, and reproducibility.

Photoelectrochemical current data are plotted in **Fig. 2.6** showing the performance of photocathodes of planar Cu_2O with CuO nanowires under prolonged testing. Cyclic voltammetry scans were repeated for 30 cycles at a scan rate of 10 mV/s for a total duration of 50 min. Photocurrent decays rapidly from ~2.7 to ~1.1 mA/cm^2 through the first five cycles; by the 30th cycle, the photocurrent seems to stabilize at 0.2 mA/cm^2. It is interesting to note that this decaying trend was not observed in a recent report of CuO nanowire based photocathodes that showed good stability for prolonged testing. Zhang *et al.* used an anodization and calcination strategy to fabricate a copper oxide composite on a transparent conducting oxide substrate. Their photocathode attained a photocurrent of 1.54 mA/cm^2 with 74.4% stability after 20 min of illumination.[37] No rationale was provided to explain why the CuO nanowire layer surface served as a protective layer for the underlying Cu_2O film. Theoretically, the requirement for resistance to corrosion for photocathodes is that its thermodynamic reduction potential is positioned above the water reduction potential or its conduction band minimum.[39] CuO, in fact, satisfies neither requirement. The potential for reduction of CuO to Cu_2O rests at +0.6 V. *vs.* NHE while the conduction band minimum rests at –0.23 V. *vs*. NHE. Therefore, CuO should be fairly similar to Cu_2O in its corrosion resistance considering that the reduction potential for conversion of Cu_2O to Cu is +0.47 V. *vs.* NHE. More investigations are needed before CuO can be regarded as a legitimate passivation layer for Cu_2O.

2.1.5.2 Planar Cu_2O with CuO Nanowires Protected by TiO_2 Thin Film

Clearly, the poor stability of as-grown planar Cu_2O photocathodes and planar Cu_2O with CuO nanowire photocathodes is a major concern. Much work has been devoted towards improving the stability of Cu_2O photocathodes, and several passivation strategies have been employed with considerable success. Sunkara *et al.* reported a stable photocurrent of 0.1 mA/cm^2 for Cu_2O films protected with 20 nm of TiO_2 deposited *via* atomic layer deposition to

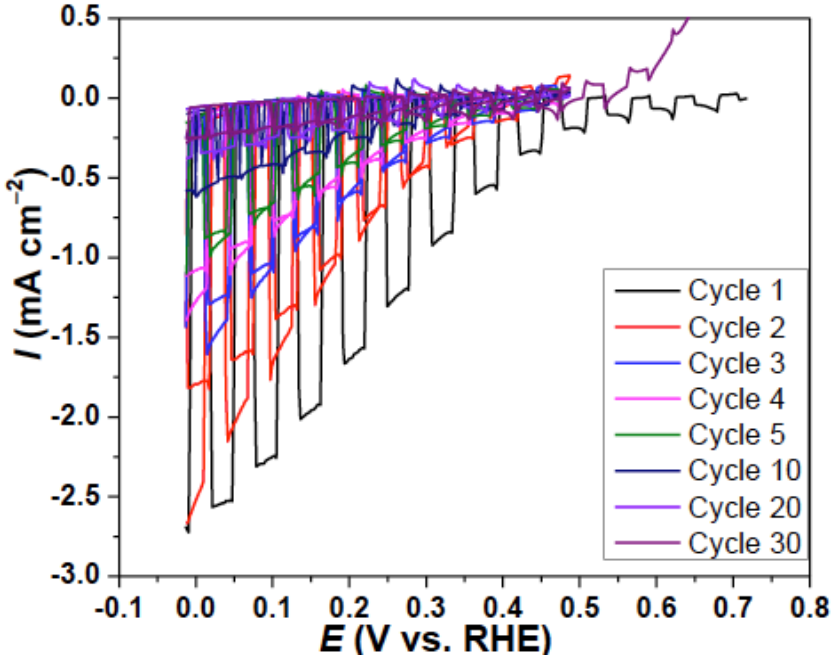

Figure 2.6 Photoelectrochemical current as a function of potential for photocathodes of planar Cu_2O with CuO nanowires under chopped 100 mW/cm^2 AM 1.5 illumination. The potential was scanned up to 30 cycles between 0 and 0.5 V *vs.* RHE at a scan rate of 10 mV/s to reveal the stability of the photocathode over time. The passage of 30 cycles equates to a testing duration of 50 min.

achieve a conformal barrier.[40] Likewise, Paracchino *et al.* used multiple stacks of ZnO, Al_2O_3 and TiO_2 to attain a photocurrent of 7.6 mA/cm^2 at a stability of 33% after 20 min of continuous illumination. It is worthwhile to mention that elemental analysis of the protective layers *via* XPS and XRD revealed that the Cu_2O was perfectly protected and remained unaltered after photoelectrochemical testing. The photocurrent degradation was instead attributed to the increase of Ti^{3+} traps in the TiO_2 layer.[7] Zhang *et al.* found a different approach through the use of 20 nm of carbon, achieving a photocurrent of 3.95 mA/cm^2 at a stability of 80.7% for their Cu_2O nanowire photocathodes. This is a marked increase over the photocurrent of the unprotected photocathodes, which was reported to be 2.28 mA/cm^2. The authors explained the increase in performance as a result of enhanced electron transfer from Cu_2O into the electrolyte *via* the electrically conductive carbon layer.[41] Noting that the as-grown planar Cu_2O with CuO nanowire photocathodes already yielded a photocurrent as high as 2.7 mA/cm^2, judicious selection of the passivation material could conceivably give rise to a similar increase in performance and stability.

To explore this possibility, 50 nm of TiO_2 was deposited onto the photocathodes. This thickness was chosen to ensure complete coverage of the CuO nanowires and prevent any exposure of the nanowires or underlying Cu_2O film. A representation of the energy band alignment of each material is shown in **Fig. 2.7**. Since the CuO and TiO_2 interface exhibits a Type-II misaligned band alignment, with both the conduction and valence bands of TiO_2 positioned below the corresponding bands for CuO, electrons are expected to assume a lower

energy state by preferentially transferring from CuO to TiO_2, while holes are expected to preferentially transfer from TiO_2 to CuO. This suggests that the addition of TiO_2 as a passivation layer presents the added benefit of improved charge separation, thereby increasing photocurrent. As CuO is known to possess short electron diffusion length, promoting electron transfer into the TiO_2 layer can protect a large fraction of electrons from recombination. Caution should be exercised, however, in the thickness of TiO_2 deposited. Owing to its band gap of 3.2 eV, TiO_2 can participate in the absorption of photons while generating only a small proportion of electron-hole pairs, as only photons in the ultraviolet range have enough energy to bridge the band gap. For this reason, its sunlight to hydrogen conversion efficiency is less than 2.2% under AM 1.5 illumination.[42] Therefore, excessively thick TiO_2 will cause only a fraction of incident photons to be absorbed by the more photosensitive copper oxides.

A magnified SEM micrograph of the CuO nanowires covered with 50 nm of TiO_2 is shown in **Fig. 2.8**. The uniform increase in the diameters of the structures along the lengths of the nanowires suggests that the deposition was conformal. The presence of nodular defects along the nanowires can likely be eliminated through subsequent annealing. The prolonged photoelectrochemical test shows excellent stability with no reduction in photocurrent during 1 hr of chopped illumination. The photocurrent at 0 V. *vs*. RHE is ~0.06 mA/cm^2.

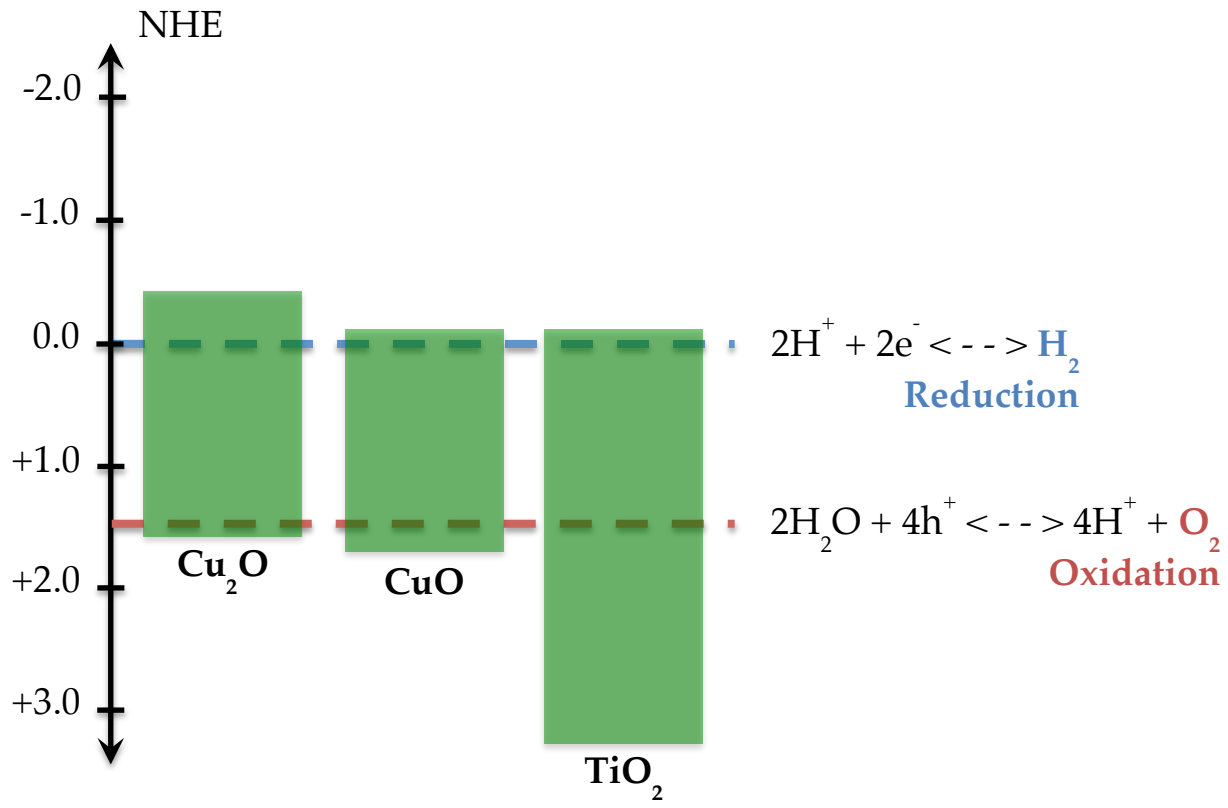

Figure 2.7 Electronic band gap positioning for Cu_2O and CuO in addition to TiO_2 relative to the water redox potentials on the NHE scale. This band structure represents the materials system composed of CuO nanowires covered by TiO_2 thin film.

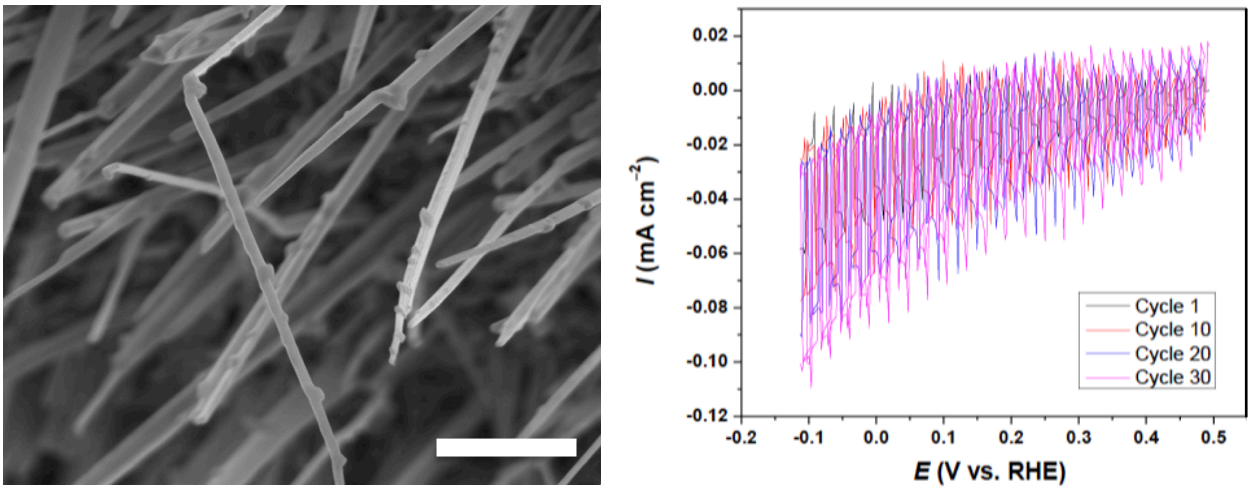

Figure 2.8 SEM micrograph of CuO nanowires coated with 50 nm of TiO_2 *via* atomic layer deposition (*left*) and photoelectrochemical testing under chopped 100 mW/cm^2 AM 1.5 illumination over 30 cycles at a scan rate of 10 mV/s (*right*). The total duration is 1 hr. Scale bar: 2 μm.

To discern the influence of TiO_2 on the stability of the CuO nanowire photocathode, the photocurrent over time was normalized to the initial photocurrent for each photocathode and plotted in **Fig. 2.9**. The unprotected photocathode exhibits a sharp decrease in photocurrent after only 8 min, dropping to less than ~10% of the original photocurrent by the end of 25 min.

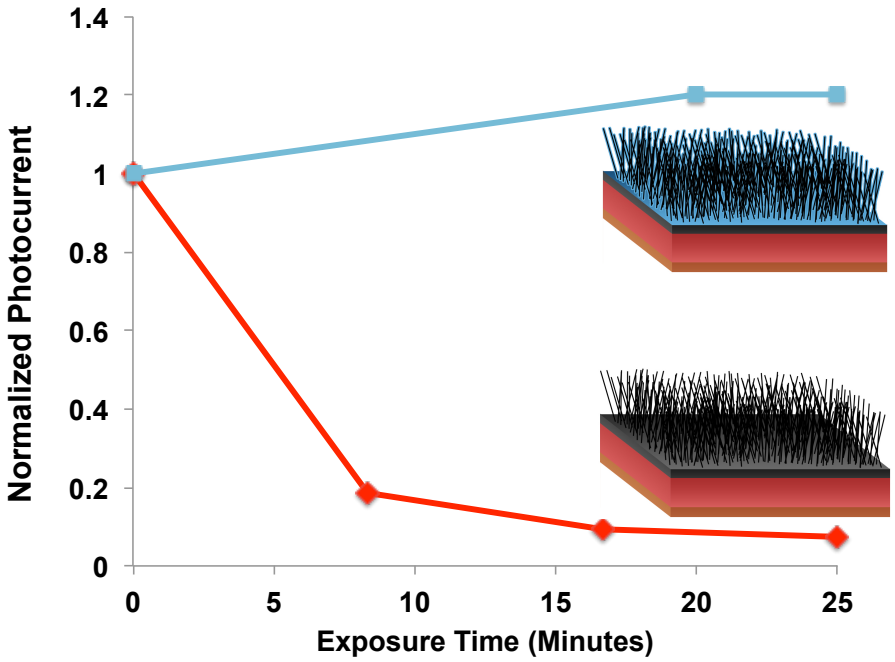

Figure 2.9 Comparison of normalized photocurrent over time for the pristine CuO nanowire photocathode and the TiO_2-protected CuO nanowire photocathode.

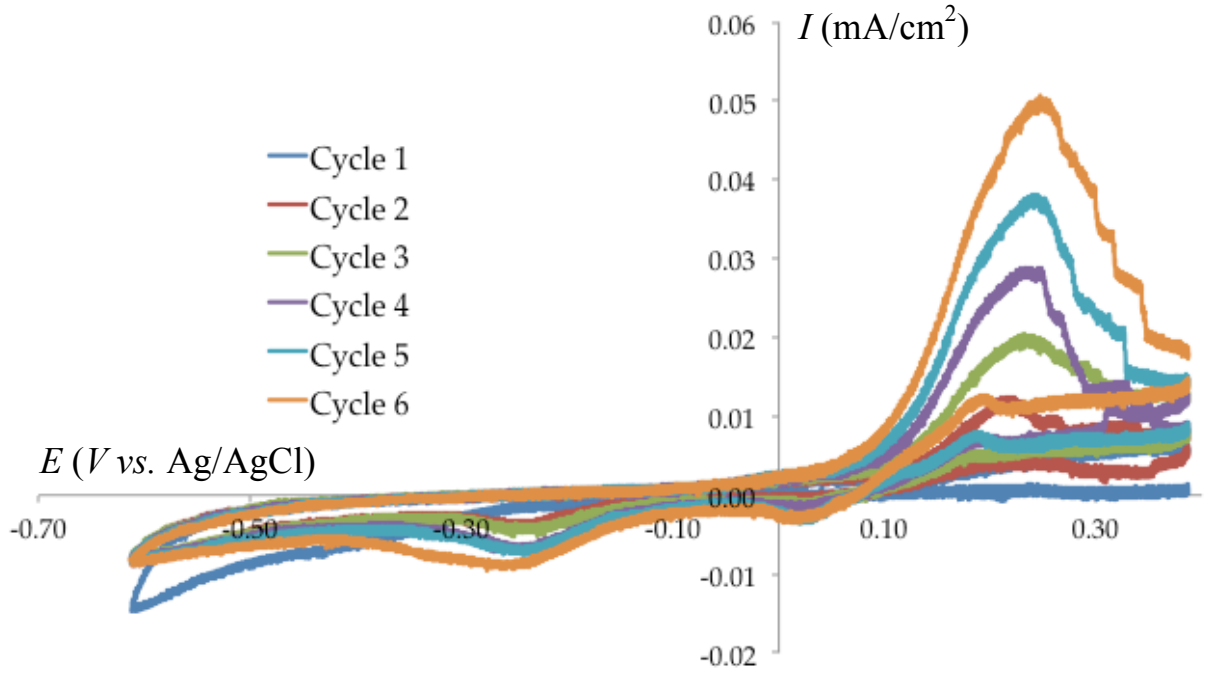

Figure 2.10 Cyclic voltammetry of 5 μm Cu_2O with 10 nm TiO_2 protection layer. The cathode was immersed in 1 M Na_2SO_4 at pH 7.0.

In contrast, the 50 nm thick TiO_2 film performs exceptionally well as a protective layer to prevent the photocorrosion of the planar Cu_2O film and CuO nanowires, as the photocurrent never decreases over the duration of the test. The slight photocurrent increase may be attributed to a conductivity increase of the TiO_2 film as electrons occupy trapped states with each subsequent cycle.[43]

For comparison, 10 nm of TiO_2 was deposited by atomic layer deposition on the deep red samples and subjected to cyclic voltammetry testing for six cycles, the equivalent of 20 min, as shown in **Fig. 2.10**. The cathodic peaks at -0.60 and -0.25 V *vs.* Ag/AgCl and the anodic peak at ~0.25 V *vs.* Ag/AgCl reveal that the photocathode is fairly unstable even with the presence of the TiO_2 thin film. The peaks grow in magnitude with each additional cycle because the oxides that are reduced during the cathodic potential sweep are reoxidized during the anodic potential sweep, which are then re-reduced once again for the next cathodic potential sweep, and so on. This repeated re-reduction and re-oxidation becomes more magnified over time as more and more of the original thermally oxidized Cu is encroached into. From this observation, it is clear that 10 nm of TiO_2 is not enough to protect planar Cu_2O photocathodes. The next step for future work, therefore, is to simultaneously achieve high photocurrent while maintaining stability by evaluating many samples with varying TiO_2 thicknesses greater than 10 nm and less than 50 nm to pinpoint one thickness that achieves this optimal balance between performance and stability.

2.1.6 Discussion

2.1.6.1 Investigation of Anomalously Large Photocurrent

The large photocurrent of the planar Cu_2O photocathode deserves a closer investigation. As stated previously, most manuscripts regarding Cu_2O-based photocathodes report photocurrent data without the accompanying gas chromatography measurement of gas evolution during photoelectrochemical testing. For a material prone to corrosion such as Cu_2O, both pieces of data are crucial because the photoexcited electrons in the semiconductor can be used towards the reduction of Cu_2O to Cu, and therefore the volume of hydrogen gas evolved may be significantly less than what is implied by the measured photocurrent.

Nonetheless, although the unprotected photocathodes at present are impractical for commercial deployment due to their instability, discovering the source of their large photocurrent can be immensely helpful for future work. To explore this further, consider a pool of electrons photoexcited in the copper oxides undergoing one of several processes: (1) transport through the semiconductor and transfer into the electrolyte, (2) recombination, (3) elimination at charged traps, or (4) reduction of the semiconductor. Of these four possibilities, only the first is desirable, as the latter three cause electrons to be wasted or consumed in corroding the cathode. The intriguing scenario is if the latter three processes can be suppressed such that only the first process is favored. For the case of the copper oxides, if there is a means of shuttling electrons out of the semiconductor and into the electrolyte quickly, before they have the chance to reduce the semiconductor, the result is not only an increase in photocurrent but also an increase in stability.

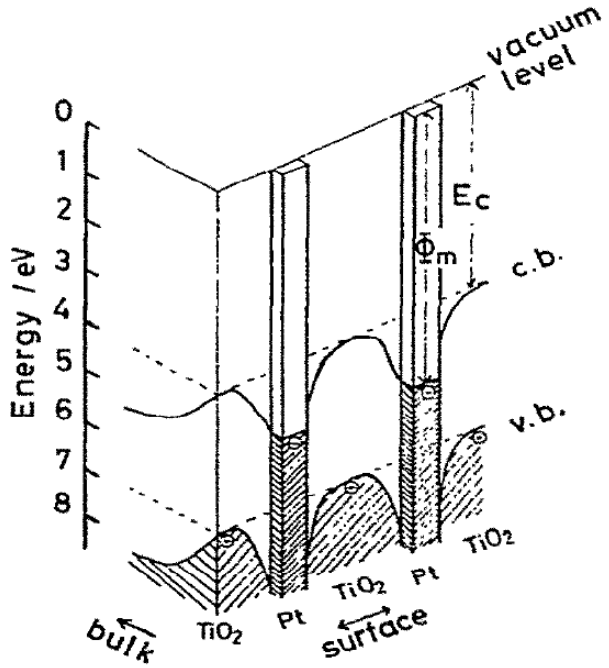

Figure 2.11 Schematic of the band structure of a TiO_2 photoanode modified with Pt nanoparticle islands on the surface.[44]

Furthermore, the high photocurrent is even more promising in light of the fact that no co-catalysts were used. Expensive noble metal co-catalysts are commonly electrodeposited onto the surface of the photocathode to enhance surface reactivity and serve as charge collection centers before they are transferred into the electrolyte. For Cu_2O in particular, Pt has been the co-catalyst material of choice. Paracchino *et al.* reported photocurrents of only several microamperes per square centimeter for bare, 1.3 μm thick electrodeposited Cu_2O films. Once Pt co-catalyst islands were electrodeposited onto the Cu_2O films, they observed a thousand-fold photocurrent increase, leading to a final photocurrent of 7.6 mA/cm^2. It is reasonable, then, to wonder if the thermally oxidized copper oxide photocathodes possess a property that mimics the catalytic and charge transfer properties of Pt co-catalysts.

One way to study the semiconductor-electrolyte interface where these phenomena take place is through the perspective of semiconductor physics. Treating the interface as a semiconductor-metal junction, knowledge of the built-in electric field and depletion width can provide clues to the photocathode's propensity to transfer electrons into the electrolyte. To provide a standard of comparison, the influence of co-catalyst islands on the band structure of the semiconductor in the bulk and surface will be described first. **Fig. 2.11** depicts the concept of Nosaka *et al.* for the model system of TiO_2 decorated with Pt nanoparticle islands, but the same concept applies to Cu_2O decorated with Pt. This illustration shows that the co-catalyst islands do not alter the band structure of the semiconductor in the bulk. Rather, the co-catalyst islands induce the formation of local electric fields only on the semiconductor surface. All in all, the influence of the co-catalyst is largely limited to the surface and has no influence on the bulk of the semiconductor.[44]

Turning to the evaluation of band structure for the thermally oxidized copper oxide photocathodes, electrochemical impedance measurements were performed at several frequencies to construct the Mott-Schottky plots of **Fig. 2.12**. The curves were plotted according to the Mott-Schottky equation:

$$\frac{1}{C^2} = \frac{2}{e\varepsilon\varepsilon_0 N_A}\left(E - E_{fb} - \frac{kT}{e}\right). \tag{2.3}$$

The down-sloping curves suggest that the semiconductor is *p*-type, as expected. Linear extrapolation of the curves to the *x*-axis yield flat-band voltage, and carrier concentration can be extracted from the slope of the curves. Given these two parameters, the depletion width x_j,

$$x_j = \sqrt{\frac{2\varepsilon_s(V_{fb}-V_a)}{qN_A}} \tag{2.4}$$

and maximum electric field ε_{max} in the depletion region,

$$\varepsilon_{max} = \frac{qN_A x_j}{\varepsilon_s} \tag{2.5}$$

can be calculated. All values for both photocathodes, as well as reference values from Paracchino *et al.*, are summarized in **Table 2.1**. It should be noted that the values of Paracchino

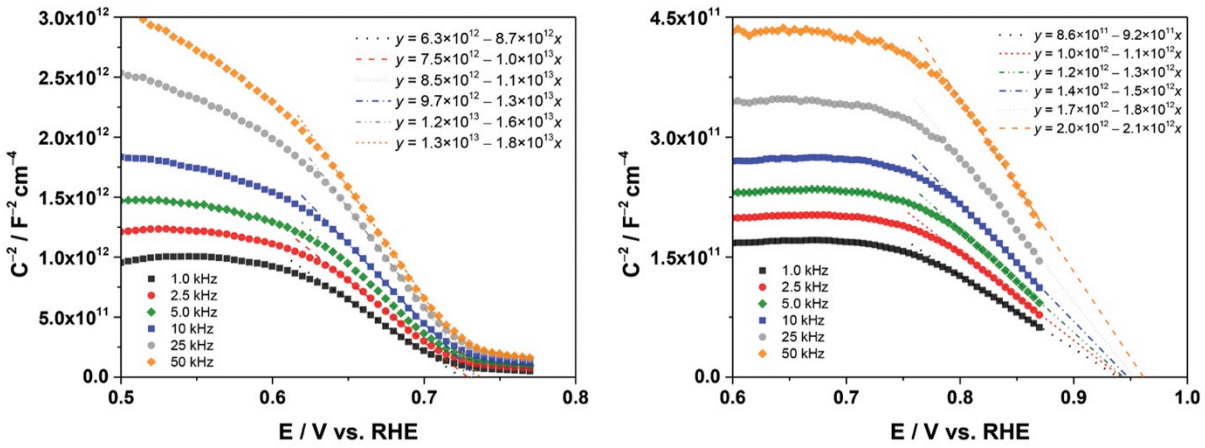

Figure 2.12 Mott-Schottky plots for the red (*left*) and deep red (*right*) samples for the evaluation of carrier concentration and flat-band voltage. The Mott-Schottky tests were performed in 0.1 M sodium acetate electrolyte at pH 7.9.

Photocathode	N_A (cm^{-3})	V_{fb} (V)	x_j (nm)	ε_{max} (V/cm)
Red	1.6×10^{18}	0.74	18.36	8.1×10^5
Deep red	1.4×10^{19}	0.95	7.03	2.7×10^6
Paracchino *et al*. (2012)	5.0×10^{17}	0.75	33.07	4.5×10^5

Table 2.1 Summary of carrier concentration, flat-band voltage, depletion width, and maximum electric field for the planar Cu_2O photocathodes.

et al. were recorded with the presence of Pt co-catalyst islands on the electrodeposited Cu_2O photocathode. They achieved a photocurrent of 2.4 mA/cm^2 under 100 mW/cm^2 AM 1.5 illumination.[7] Conversely, measurements were performed for the red and deep red samples as-grown, without co-catalysts or any other modification. Photocurrents were measured to be as large as 2.0 mA/cm^2.

By virtue of the larger carrier concentration of thermally-oxidized Cu_2O, the deep red photocathode in particular exhibits a strong electric field of 2.7×10^6 V/cm limited to a depth of 7.03 nm from the semiconductor surface. This surface-localized electric field is reminiscent of the metal co-catalyst islands, which generate electric fields locally on the semiconductor surface. According to Lewis *et al*., the electric field in semiconductor photoelectrodes is known to be as large as 10^5 V/cm.[45] Evaluated by this standard, these planar Cu_2O photoelectrodes are particularly effective in shuttling electrons from the semiconductor into the electrolyte. The high carrier concentration arising from the unique and facile synthesis process of thermal oxidation is a compelling explanation for the large photocurrent.

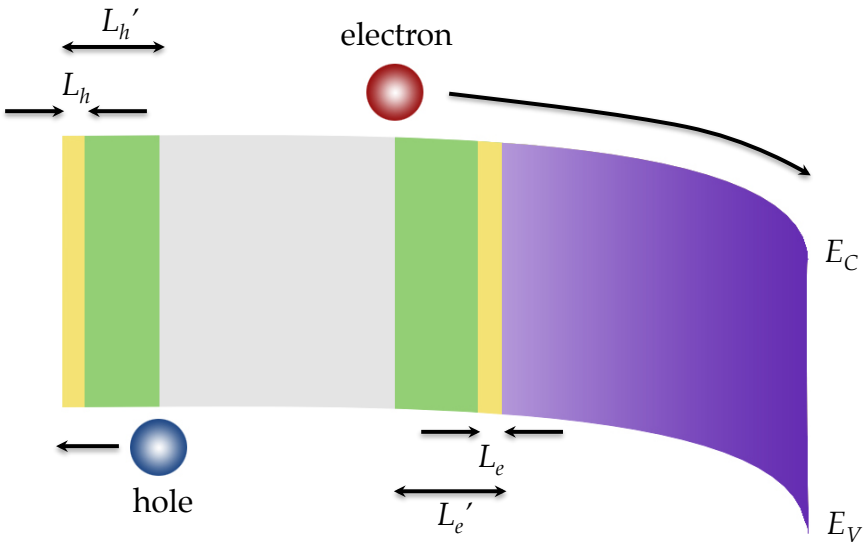

Figure 2.13 Schematic of Cu_2O band structure showing the influence of diffusion lengths L_e and L_h, denoted in yellow, extended to L_e' and L_h', respectively, stretching into the green regions. An elongation of diffusion length expands the volume of semiconductor from which photoexcited carriers can be harvested for photoelectrochemical water splitting.

It could be argued that the large photocurrent of the dead red samples is more closely related to the thickness of the deep red samples, which are 5 μm compared to 1.3 μm for Paracchino *et al.* Considering that the absorption depth of Cu_2O is ~10 μm, the 5 μm photocathode should certainly generate more electron-hole pairs, but not all these free carriers will be harvested. The minority carrier diffusion length must also be taken into account. Compared to electrodeposited Cu_2O, thermally oxidized Cu_2O should possess higher crystallinity and therefore larger minority carrier diffusion length. As illustrated in **Fig. 2.13**, a semiconductor with electron diffusion length L_e and hole diffusion length L_h will have only those carriers excited in the yellow regions harvested, but extending these diffusion lengths to L_e' and L_h', respectively, will expand the volume from which these carriers are extracted into the green regions. A report studying the mobility of thermally oxidized Cu thin films deposited by sputtering measured a fourfold mobility enhancement over typical values for electrodeposited Cu_2O.[26] However, it would be difficult to justify the large photocurrent of the planar Cu_2O on this basis alone given that the photocurrent for pristine electrodeposited Cu_2O reported by Paracchino *et al.* was only on the order of several microamperes per centimeter. Even a tenfold increase in minority carrier diffusion could not completely account for a thousandfold improvement in photocurrent.

The implications of these results are promising. Since this Cu_2O photocathode obtained *via* thermal oxidation is highly photoactive, a large pool of electrons could participate in water reduction if the electrons are quickly shuttled into the electrolyte. Furthermore, this photocurrent is possible without the aid of expensive co-catalysts like Pt, which typically drive this charge transfer process into the electrolyte for overall water splitting. Although Pt has been shown to be extremely effective in catalyzing hydrogen evolution, continued investigations into alternatives to noble metal co-catalysts, including the use of transition metals like Ni and Cu,[46] core-shell

nanoparticles,[47] bimetallic alloys,[48] and transition metal carbides[47] clearly show the urgent need to replace this costly noble metal co-catalyst. The large photocurrent obtained by these Cu_2O photocathodes therefore represents an encouraging step towards highly efficient and cost-effective hydrogen evolution.

2.1.6.2 Hydrogenation of Nanowires from CuO-TiO_2 to Cu_2O-H:TiO_2

A possible strategy towards enhancing both photoactivity and stability through the hydrogenation of Cu_2O-TiO_2 core-shell nanowire photocathodes was also investigated. To describe the concept of this strategy, the core and shell materials will be discussed separately. The literature reports highly successful visible light sensitization of TiO_2 through hydrogen annealing at elevated temperatures. Wang *et al.* observed a photocurrent increase from ~0.6 to 2.5 mA/cm^2 following hydrogenation of TiO_2 nanowire arrays at 350 °C for 30 min.[33] Chen *et al*. used hydrogenation to create lattice disorder in TiO_2 nanocrystals while simultaneously introducing hydrogen dopants, which stabilize mid band gap states that extend optical absorption into the visible range.[49] To date, hydrogenation has been a highly successful strategy towards improving the light absorption of TiO_2 while minimizing the deleterious effects of charged trap states.

Meanwhile, in the case of the CuO nanowires, hydrogenation can serve a similar purpose. Exposing CuO to a reducing atmosphere for conversion to Cu_2O should improve its sensitivity to visible light, as Cu_2O is a direct band gap semiconductor while CuO is an indirect band gap semiconductor. Moreover, Cu_2O exhibits much larger minority carrier diffusion length compared to CuO, which should allow photoexcited electrons a higher likelihood of being transported into the electrolyte. Synthesizing Cu_2O in the form of nanowires will only further enhance its photoactivity because its absorption length is much larger than its minority carrier diffusion length. This is the challenge of thin film systems, whose absorption and carrier collection pathways share the same direction orthogonal to the plane of the thin film. The nanowire morphology decouples these pathways with light absorption adjusted by the length of the nanowires while carrier collection is tuned by the diameter of the nanowires. With control of these two geometric parameters, the light absorption and carrier collection can be optimized separately.

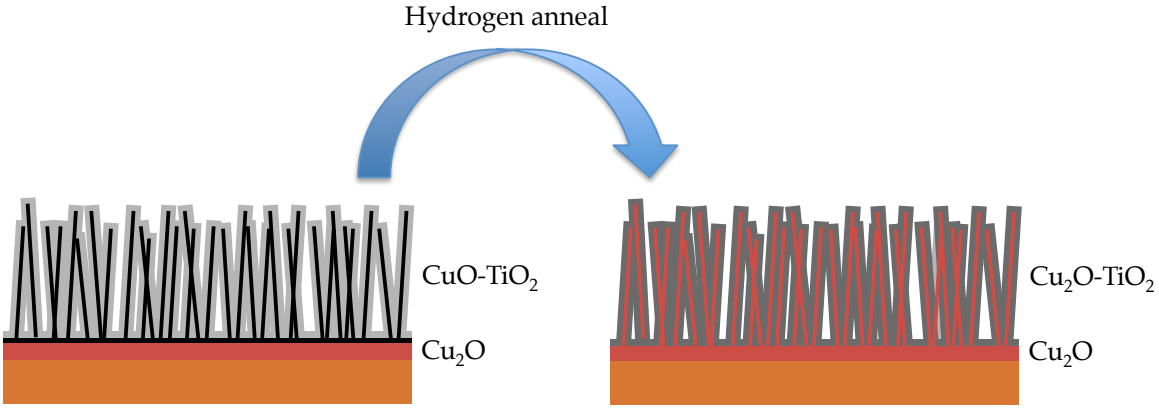

Figure 2.14 Schematic of hydrogen anneal process illustrating the formation of Cu_2O-TiO_2 core-shell nanowires through the reduction of nanowires from CuO to Cu_2O.

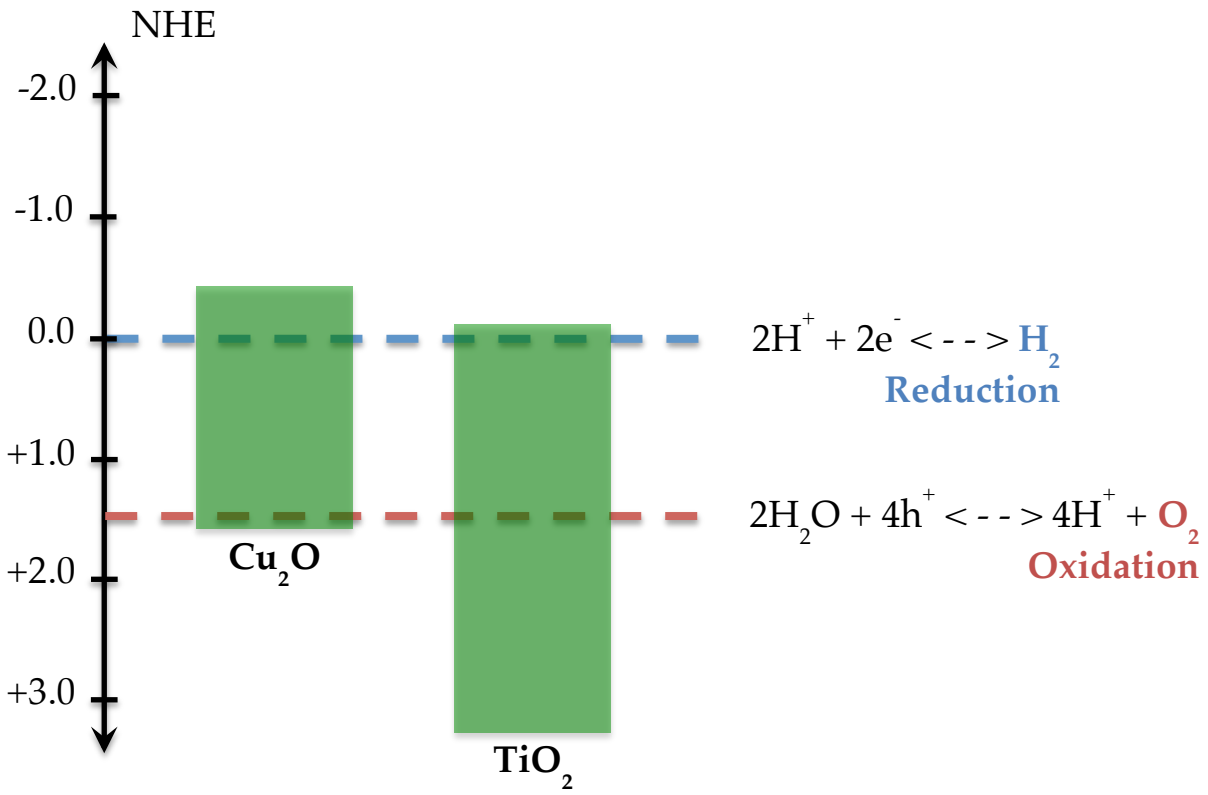

Figure 2.15 Electronic band gap positioning for Cu_2O and TiO_2 relative to the water redox potentials on the NHE scale. This band structure represents the materials system composed of Cu_2O nanowires covered by TiO_2 thin film.

Considering the advantages of hydrogenation for TiO_2 and CuO, combining these two materials should give rise to an interesting materials system for photocatalysis. A schematic of this system is illustrated in **Fig. 2.14**. In contrast to the system discussed in **Chapter 2.1.5.2**, the hydrogenated TiO_2 in this system would not only serve as a protective layer for Cu_2O, but also participate in light absorption. It is also important to note that the Cu_2O-TiO_2 heterojunction will maintain the Type-II misaligned band gap structure, which will promote charge separation of photoexcited electrons and holes. The band structure of the entire system in reference to the water redox potentials is shown in **Fig. 2.15.**

This concept was examined by depositing 50 nm of TiO_2 on the CuO nanowires *via* atomic layer deposition. There was concern that starting with a thinner layer could make the subsequent hydrogenation process challenging, as a hydrogenation that is slightly too hot or too long in duration could possibly reduce CuO completely to Cu. To prevent this, a thicker TiO_2 film of 50 nm was deposited to allow for a larger margin of error in hydrogenation temperature and time. Compared to the CuO-TiO_2 core-shell nanowires that were not subjected to hydrogenation as shown in **Fig. 2.8**, the hydrogenated samples of **Fig. 2.16** appear significantly roughened. As one of the intended functions of the TiO_2 film is to inhibit corrosion of the nanowires with highly conformal protective coating, this significant morphological modification due to hydrogenation further emphasizes the importance of carefully controlling hydrogenation

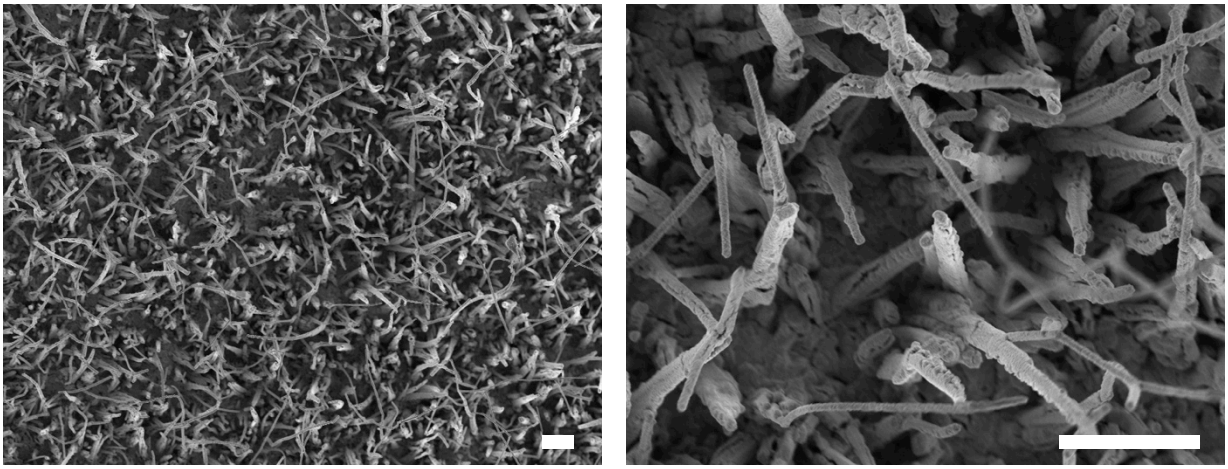

Figure 2.16 SEM micrograph showing a CuO nanowire array following TiO_2 deposition and a subsequent hydrogenation performed at 350 °C for 30 min. (*left*), and a close-up view showing the roughened surface (*right*). Scale bar: 2 μm.

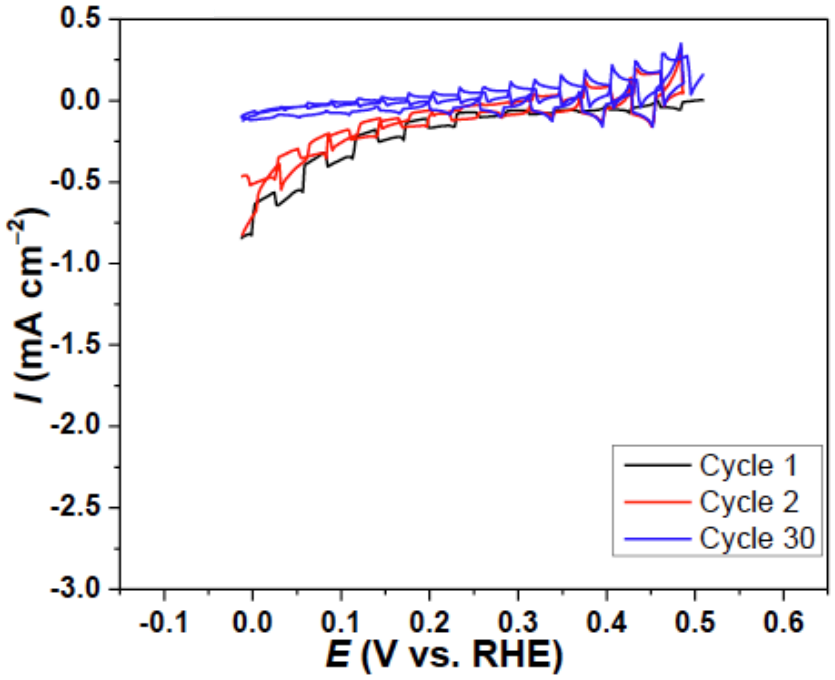

Figure 2.17 Photoelectrochemical testing of CuO-TiO_2 core-shell nanowire photocathodes following hydrogenation at 350 °C for 3 min in a 100% hydrogen environment. The test was performed in 1 M Na_2SO_4 buffered at pH 4.9. The scan rate was 10 mV/s.

temperature and time so that the CuO nanowire is reduced to Cu_2O without opening structural defects in the TiO_2 film, leaving the core vulnerable to corrosion.

Extended photocurrent tests were performed under chopped AM 1.5 illumination to evaluate the performance and stability of these photocathodes as shown in **Fig. 2.17**. Note that the hydrogenation was reduced to 3 min to minimize structural modification of the TiO_2 film. The large dark current of ~0.7 mA/cm^2 at 0 V. *vs.* RHE during the first cycle is attributed to photoreduction of the CuO. This dark current decreased to ~0.5 mA/cm^2 after the second cycle and finally to ~0.1 mA/cm^2 after the thirtieth cycle. Meanwhile, the photocurrent also decreased from an initial value of ~0.2 mA/cm^2 to ~0.1 mA/cm^2 and eventually 0 mA/cm^2 after the thirtieth cycle. This decay in photocurrent is justified in light of the continual reduction of CuO. When no copper oxide remains and the dark current is nearly zero, the photocathode cannot produce any more photocurrent. It is important to note that there is a sizeable oxidation current for the thirtieth cycle that can be observed at a bias of 0.5 V *vs.* RHE. Since this current appears to increase with each subsequent cycle and eventually dominates the reduction current, it suggests that the material has no other option but to be oxidized because it has already been reduced completely in previous cycles.

In light of these results, attention should be directed to retarding the hydrogenation process in order to minimize morphological changes and inhibit reduction of Cu_2O further to Cu. Future directions for investigation include lowering the hydrogenation temperature to slow down the reduction of Cu_2O or introducing inert gases to lower the concentration of hydrogen in the environment.

2.2 Copper Oxide for CO_2 Reduction

2.2.1 Motivation

While the development of renewable energy technologies continues to progress rapidly, there remains growing concern over the increasing rate of carbon emission from the combustion of fossil fuels. The National Renewable Energy Laboratory estimates that by 2050, 80% of the electricity demand in the United States can be supplied by renewable technologies.[50] In the meantime, carbon dioxide levels in the atmosphere will continue to climb. Measurements of global mean CO_2 concentration over the past 800,000 years compiled by the Scripps Institution of Oceanography as shown in **Fig. 2.18** reveal that CO_2 levels are reaching unprecedented marks. Although CO_2 concentration has routinely varied between 180 to 280 ppm during this time span, a concentration of 400 ppm was recently measured in May 2013 and is expected to continue climbing exponentially. Compared to a 0.90 ppm per year increase in the years between 1963 to 1972, the annual increase over the last decade has vaulted to 2.07 ppm per year (**Fig. 2.19)**.[51] At this rate, irreparable damage will be inflicted on the environment if CO_2 emissions are allowed to increase unhindered.

In addition to reducing future CO_2 emissions, a proactive approach to addressing the high CO_2 concentration is to chemically reduce CO_2 into liquid fuel or a mixture of CO and H_2, known as syngas, en route to liquid fuel. The concept of scavenging CO_2 to produce useful fuels

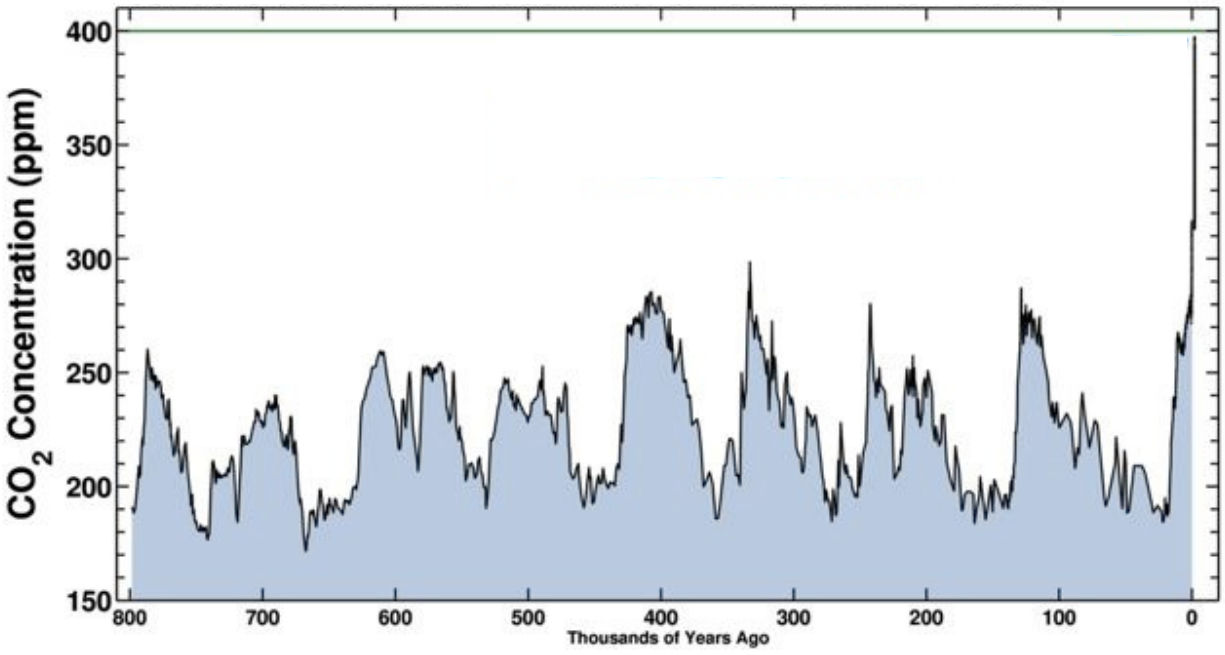

Figure 2.18 Atmospheric CO_2 concentration levels dating back 800,000 years from the present day. Measurements of concentrations before 1958 were sampled from CO_2 in air bubbles preserved in ice cores from Antarctica. Concentrations after 1958 were sampled at Mauna Loa Observatory in Hawaii. Carbon dioxide concentration recently topped an unprecedented level of 400 ppm.[51]

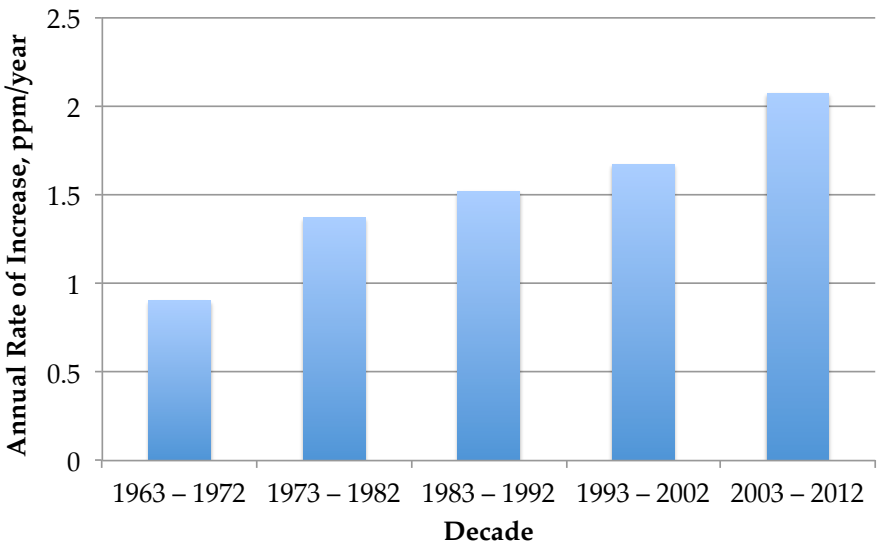

Figure 2.19 Annual rate of increase of atmospheric CO_2 concentration in units of ppm per year.[51]

is an attractive strategy for diminishing the concentration of atmospheric CO_2, but practically speaking, reducing CO_2 is very challenging because it is a simple and stable molecule. The liquid fuels, in contrast, possess more complex molecular structure, requiring several proton-coupled, multi-electron reactions. Constructing these fuels from CO_2 therefore calls for the significant restructuring of existing C-O bonds and formation of C-H and C-C bonds.

Two strategies are generally employed. One approach is to follow a less kinetically demanding pathway to produce a mixture of CO and H_2, which are then converted to liquid fuels through the well-known Fischer-Tropsch process. Alternatively, CO_2 can be converted directly to a liquid fuel through a series of reactions in which different catalysts activate each reaction in sequence. Finding a catalyst that can execute either approach efficiently, require only small overpotentials, and selectively favor the production of one fuel over many other possible fuels, has been the primary challenge. Many different materials have been explored with these goals in mind. Solid oxide electrolytic cells operating at temperatures exceeding 750 °C were demonstrated to efficiently reduce only CO_2 to CO. However, for cost effective CO_2 conversion, a catalyst enabling operation near room temperature would be more desirable.

Products	HCOOH	CO	CH_4, C_2H_4	H_2
Metal electrodes	Pb, Hg, In, Sn Cd, Tl, Bi	Au, Ag, Zn Pd, Ga	Cu	Ni, Fe Pt, Ti

Table 2.2 Summary of primary products formed during CO_2 reduction on various metal electrodes.

For this purpose, several polycrystalline metals have been observed to be suitable electrode materials. Hori *et al*. performed CO_2 reduction tests on several metal electrodes in 0.1 M $KHCO_3$ at room temperature and classified them into four primary categories depending on the primary products produced; these categories are summarized in **Table 2.2**.[52] The first category, which favors HCOOH production, is known for large overpotentials for water reduction and poor CO adsorption. The second category exhibits poor CO adsorption and effectively breaks the C-O bond in CO_2, resulting in the formation of CO as the main product. Cu is an intriguing electrode material owing to its ability to generate CO and further drive subsequent reduction processes to yield CH_4 and C_2H_4. Lastly, the fourth category exhibits low overpotentials to water reduction and strong CO adsorption, resulting in H_2 as the primary product. All these metals are limited either due to the need for large overpotential, poor selectivity, or preferential reduction of H_2 over CO_2.

2.2.2 The Challenges of CO_2 Reduction

The delicate nature of CO_2 reduction associated with the multiple possible reaction products is depicted in the energy band diagram of **Fig. 2.20**. Near 0 V. *vs.* NHE rests several reduction potentials corresponding to the production of HCOOH, CO, HCOH, CH_3OH, and CH_4 along with the water reduction potential; the proton-coupled, multi-electron reactions for each product are listed in **Eq. 2.6-2.9**. Herein lies the inherent difficulty of preferentially generating

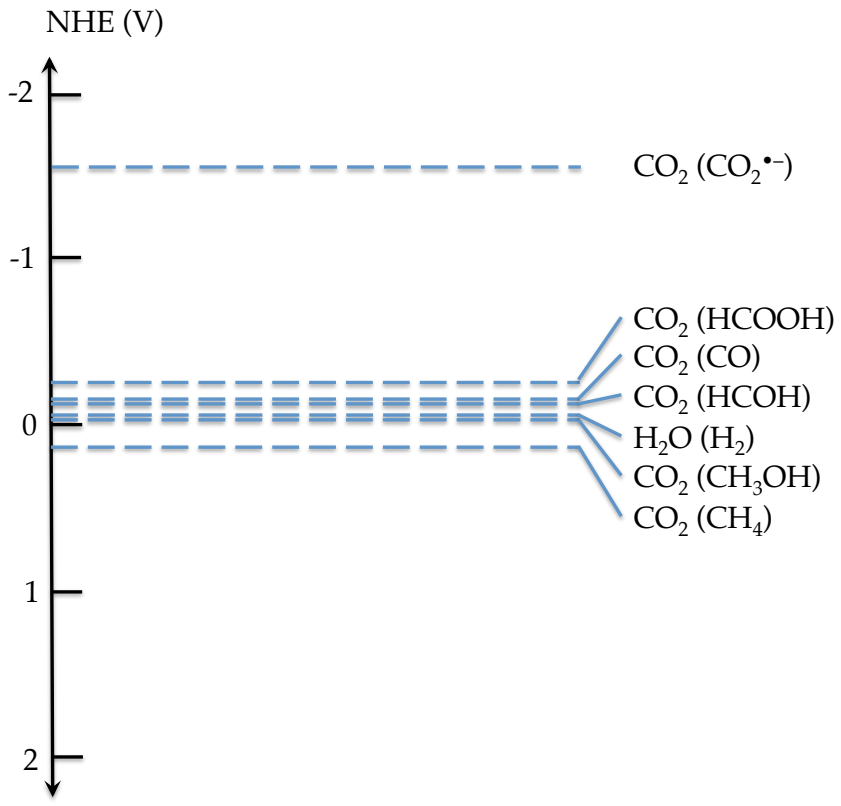

Figure 2.20 Positions of the H_2O and CO_2 reduction potentials on the NHE scale at pH 1.0.

$$CO_2 + 2H^+ + 2e^- \rightarrow CO + H_2O \quad \textbf{(2.6)}$$

$$CO_2 + 2H^+ + 2e^- \rightarrow HCO_2H \quad \textbf{(2.7)}$$

$$CO_2 + 6H^+ + 6e^- \rightarrow CH_3OH + H_2O \quad \textbf{(2.8)}$$

$$CO_2 + 8H^+ + 8e^- \rightarrow CH_4 + 2H_2O \quad \textbf{(2.9)}$$

$$CO_2 + e^- \rightarrow CO_2^{\bullet -} \quad \textbf{(2.10)}$$

one product over the others: the reduction potentials lie in close proximity to one another, so an applied potential that favors one reaction will likely favor neighboring reactions simultaneously. Compounding this challenge further is the presence of the water reduction potential in the midst of the CO_2 reduction potentials. This is particularly problematic for the metals Ni, Fe, Pt, and Ti because their surfaces strongly absorb CO, and consequently H_2 becomes the primary product instead of CO.

Yet, amidst these concerns, the biggest challenge continues to be the large overpotential requirement, which significantly limits energy efficiency. This overpotential is caused by an intermediate reaction that forms the $CO_2^{\bullet -}$ radical anion represented by **Eq. 2.10**. This reaction is positioned at –1.90 V. *vs.* NHE at pH 7, significantly more negative than any of the other reactions of **Eq. 2.6-2.9**. As $CO_2^{\bullet -}$ is a necessary precursor en route to subsequent reduction reactions that form the products of **Eq. 2.6-2.9**, the formation of this anion presents a large energetic barrier to the initiation of CO_2 reduction and is the rate-limiting step. Thereafter, $CO_2^{\bullet -}$ gives rise to the formation of $HCOO^-$ or CO. For the case of $HCOO^-$, $CO_2^{\bullet -}$ combines with a proton from H_2O to form $HCOO^\bullet$ followed by a reduction step at the electrode to yield $HCOO^-$. Alternatively, a hydrogen evolution reaction running in conjunction can provide adsorbed hydrogen to react with $CO_2^{\bullet -}$ to form $HCOO^-$. The formation of CO follows a similar pathway, but the proton bonds with $CO_2^{\bullet -}$ at the oxygen atom rather than the carbon atom. A subsequent reduction then yields CO. Similarly, CO can also be formed with $CO_2^{\bullet -}$ directly reacting with adsorbed hydrogen. $HCOO^-$ and CO serve as the precursors for subsequent reactions to yield the desired liquid fuels.

2.2.3 Current Outlook

Metal-based electrodes have received greater attention for CO_2 reduction over the past 20 years. In a survey of several metals, Hori *et al.* discovered that the metals yielding the highest Faradaic efficiencies for the production of CH_4 and C_2H_4, CO, and HCOOH are Cu (33.3% and 25.5%), Au (87.1%), and Hg (99.5%) respectively.[52] The prevailing concern with Cu is the large overpotential needed for CO_2 reduction, which has been reported to be as high as 0.7 V.[53] Nonetheless, Cu continues to receive considerable attention due to its high catalytic performance in producing hydrocarbons. Through the emergence of unique Cu surface morphology *via* electrochemical reduction of thick Cu_2O films, Li *et al.* successfully lowered the overpotential for CO_2 reduction to less than 0.4 V. Faradaic efficiency for the formation of CO peaked at ~45% for an overpotential of ~0.25 V; for HCO_2H, it reached ~40% for an overpotential of ~0.35 V. Additionally, they achieved stable operation for several hours, a marked improvement

over previous reports that observed deactivation of polycrystalline Cu electrodes.[53] Chen *et al*. employed a similar strategy to synthesize oxide-derived Au nanoparticles that reduce CO_2 to CO at an exceedingly low overpotential of 140 mV.[54] The Au nanoparticles maintained their reactivity over the course of 8 hr. In comparison, polycrystalline Au electrodes subjected to the same operating conditions required at least 340 mV and rapidly deactivated. Hg is known to be especially effective in selectively forming HCOOH over H_2, but this performance comes at the cost of very large overpotentials needed to drive CO_2 reduction.[55]

2.2.4 Experimental Setup

Oxidized Cu foils were prepared by cutting Cu sheets, 99.98% purity obtained from Sigma-Aldrich, into coupons of area ~3 cm^2. The coupons were cleaned in 1 M HCl for 1 min, rinsed in deionized water, and dried. Prior to thermal oxidation, the coupons were tightly wrapped around glass microscope slides to facilitate handling thereafter. Six copper oxides of various composition and thickness were grown; the thermal histories implemented for each sample during oxidation are as follows. A ~1 μm thick Cu_2O layer was grown on the Cu foil through a heat treatment in air consisting of an initial 0.5 hr ramp up to 300 °C, soaking at a constant 300 °C for 0.5 hr, followed by a 4 hr cooling step to return the sample to room temperature. A similar thermal history was employed to grow a ~5 μm thick Cu_2O layer; the ramp up time to reach 300 °C was extended to 1 hr, followed by an oxidation period of 10 hr at a constant 300 °C, and finally ending with a cooling step over 4 hr to reach room temperature. Lastly, four more samples were grown at an oxidation temperature of 500 °C; the oxidation periods of these samples were 0.5, 2, 5, and 10 hr. The ramp up and ramp down steps for each of these samples were fixed at 1 hr and 4 hr, respectively. The photographs of **Fig. 2.21** show the color and surface finish of the resulting oxidized foils. While the samples oxidized at 300 °C exhibited a difference in color but similar surface finish, allowing incident light to reflect from the surface, the sample oxidized at 500 °C exhibited an extremely dark, velvet-like texture associated with the exceptional light-trapping properties of CuO nanowires grown on the surface. Low-resistance ohmic contacts were made by gently abrading the surface to reveal the underyling Cu layer, and silver paste and epoxy were then applied to attach electrical wires at the abraded areas. The edges of the oxidized coupons were also sealed with epoxy to leave only an exposed area of ~1 cm^2 for electrolyte access.

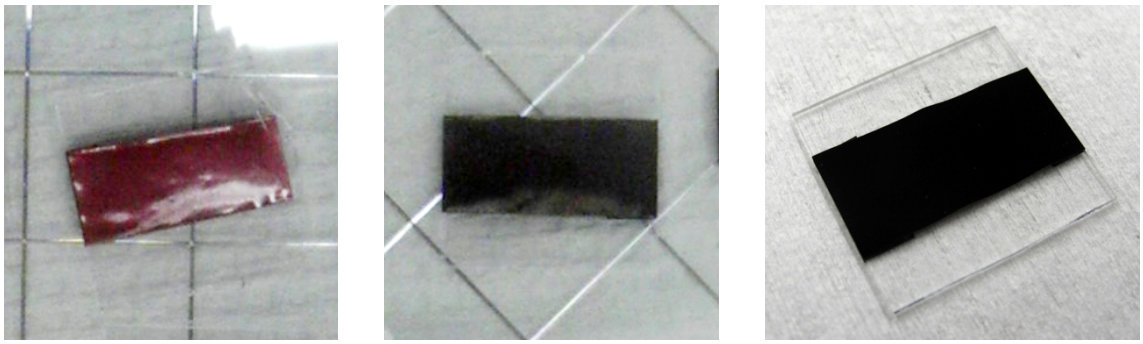

Figure 2.21 Photographs of Cu foils following thermal oxidation in air. These samples were subjected to oxidation conditions of 300 °C for 0.5 hr (*left*), 300 °C for 10 hr (*middle*), and 500 °C for 2 hr (*right*).

A standard three-electrode configuration was employed for CO_2 reduction tests. The oxidized foils served as the working electrode, an Ag/AgCl electrode saturated with KCl as the reference electrode, and Pt wire as the counterelectrode. These electrodes were all immersed in 0.1 M $KHCO_3$ at pH 8.9. A constant CO_2 flow rate of 5.3 mL/min was maintained for all tests. The two-chamber electrolytic cell used for testing was continuously flushed with CO_2. At the start of each test, Cu reaction sites for CO_2 reduction were exposed by electrochemically reducing the oxidized foils at a fixed current of –5 mA while gas phase products were continuously monitored by a gas chromatograph. Step-like reduction of potential signaled the onset of CO and H_2 formation. Chronopotentiometry data, as well as chronoamperometry data for a fixed overpotential of –0.5 V *vs.* RHE, was acquired and analyzed with a Gamry Reference 3000 potentiostat.

2.2.5 Results and Discussion

Electrochemical reduction of the oxidized Cu foils was performed to reveal reduction sites of Cu, readying the surface for CO_2 reduction. Each of the chronoamperometry curves of **Fig. 2.22** exhibited stabilized potentials near ~ –0.05 V and ~ –0.40 V *vs.* RHE; these potentials correspond to the reduction of CuO to Cu_2O and finally to Cu. The sample oxidized at 300 °C for 10 hr reached a stable potential of ~ –0.5 V after ~9 min, while the other samples oxidized at 500 °C for 0.5, 2, 5, and 10 hr stabilized after ~50, ~90, ~100, and ~140 min, respectively. The longer required reduction times correspond with increasing oxide thickness: thicker Cu_2O and CuO layers demand longer reduction times in order to be converted into Cu. In the meantime, the overpotentials at which CO_2 reduction was initiated were also reduced; this may be explained by a lowered overall system resistance due to larger thicknesses of Cu participating in CO_2 reduction. These reduction times, along with the corresponding charge required to reduce the copper oxides, are summarized in **Table 2.3**. At the instant the potentials reached the final potential floor, CO and H_2 products began to form. The formation of formic acid beginning at the onset of these stabilized potentials provided further confirmation that the reduction of the oxides had sufficiently progressed and activated the surface with Cu for CO_2 reduction. The linear trend in formic acid produced for the sample oxidized at 500 °C for 0.5 hr, plotted in **Fig. 2.22** with the zeroth hour denoting the start of CO_2 reduction, also suggests that this electrode remained stable over a 1.5 hr period.

The concentrations of CO and H_2 generated during CO_2 reduction are projected atop the reduction curves in **Fig. 2.23**. For the thinnest oxide, grown at 300 °C for 0.5 hr, H_2 was the dominant product, stabilizing at a concentration of ~0.9% after 1 hr; negligible CO was produced for this sample. Extending the oxidation time to 10 hr gave rise to a stable production of CO at a concentration of ~0.1%. The concentration of H_2 formed was comparably less than in the case of the oxide grown at 300 °C for 0.5 hr, although CO concentration continued to increase even at the end of 2 hr. For the oxide grown at 500 °C for 2 hr, which possesses a significantly different surface morphology consisting of vertically aligned CuO nanowires, CO became the more dominant product. By the end of 3 hr, the CO concentration reached ~0.28% while the H_2 concentration was about ~0.22%. It appears that the CuO nanowires, which were reduced to Cu prior to CO_2 reduction, may have introduced unique crystal orientations of Cu that are conducive to lysing C-O bonds in CO_2 and poorly adsorb CO, resulting in higher CO generation.

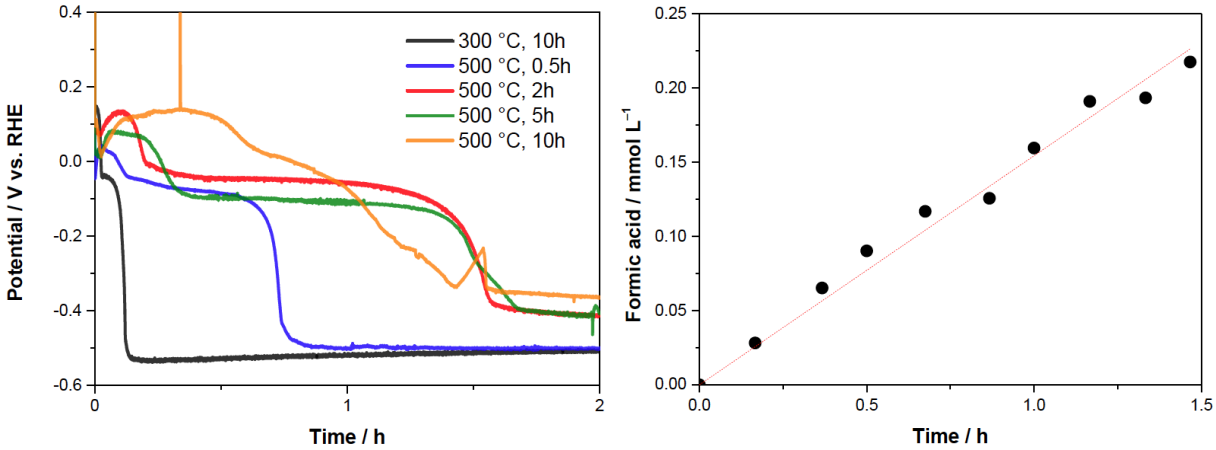

Figure 2.22 Chronoamperometry detailing electrochemical reduction history for five samples at a fixed current of –5 mA (*left*), and formic acid production for the sample oxidized at 500 °C for 0.5 hr, which began the moment the potential stabilized (*right*).

Oxide Growth Conditions		Electrochemical Reduction Conditions	
Temperature (°C)	**Time (hr)**	**Time of Reduction (s)**	**Charge Provided (C)**
300	0.5	171	0.86
300	10	547	2.7
500	0.5	3069	15.4
500	2	5659	28.3
500	5	6050	30.3
500	10	8408	42.0

Table 2.3 Electrochemical reduction time and charge required to activate the oxidized Cu samples for CO_2 reduction.

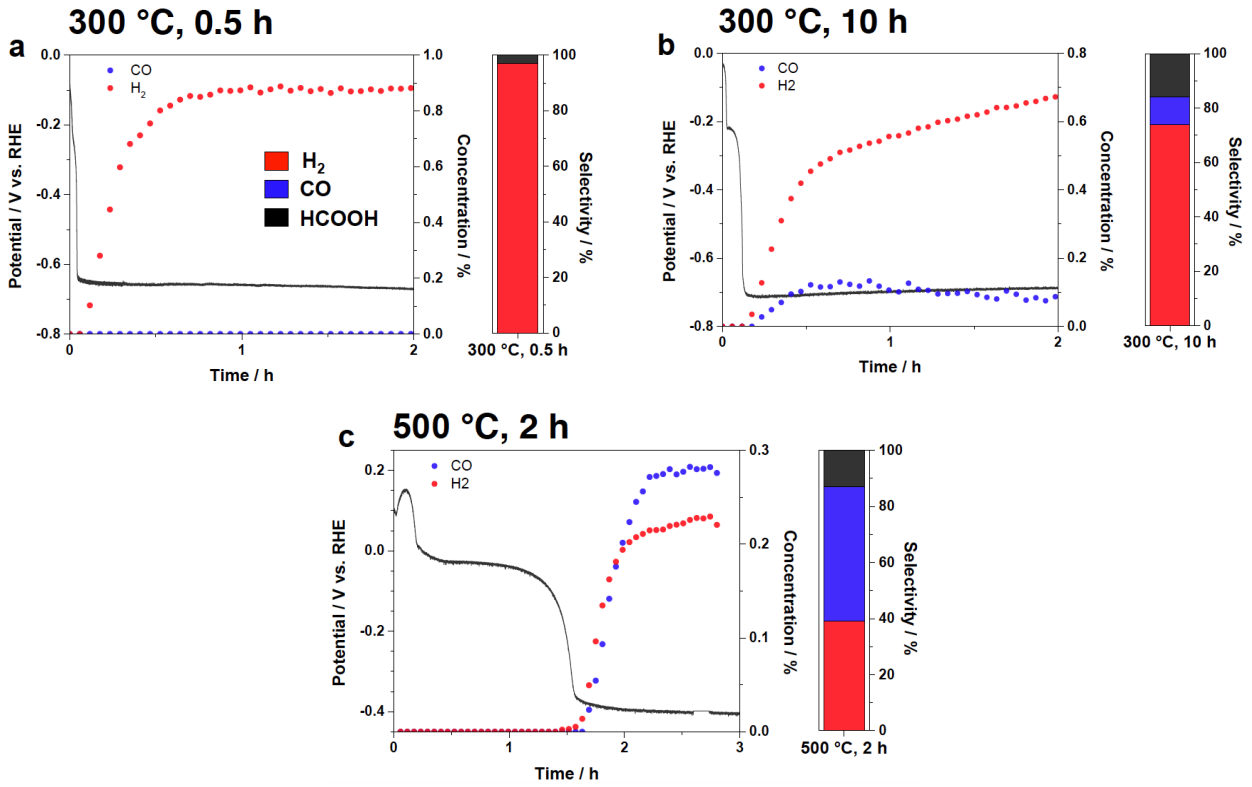

Figure 2.23 Chronoamperometry detailing CO_2 reduction progress for three copper oxide samples at a fixed current of –5 mA.

Faradaic efficiencies extracted from chronopotentiometry measurements of samples oxidized at 500 °C were collected to ascertain the influence of oxide thickness on the efficiency of H_2, HCOOH, CO, and CH_3COOH formation as plotted in **Fig. 2.24**. Apart from a peak and valley in Faradaic efficiency for HCOOH at oxidation times of 5 and 10 hr, respectively, the efficiencies for each product did not exhibit significant trends with increasing oxidation time. The Faradaic efficiencies for H_2, CO, and CH_3COOH formation stabilized at ~35%, ~15%, and ~5%, respectively, for oxidation duration up to 10 hr, while the efficiency for HCOOH formation took on values between ~15% and ~35%. Combined with the observations of **Fig. 2.23**, it appears that the change in oxide composition from bare Cu_2O to Cu_2O with CuO nanowires caused CO to supplant H_2 as the dominant product. The reason that the Faradaic efficiencies remain relatively constant with oxidation time is because the surface morphology does not exhibit significant changes as oxidation time is increased. For comparison, Li *et al*. observed a continual increase in Faradaic efficiency of HCOOH formation with both oxidation temperature and time simultaneously increasing, but it is unclear whether their electrodes would behave similarly for a change of oxidation temperature only.[53]

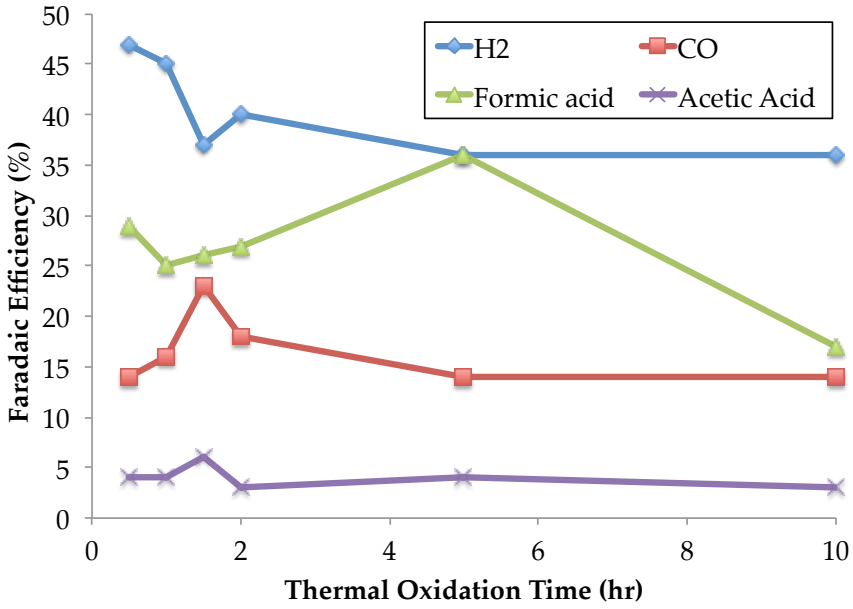

Figure 2.24 Trends in Faradaic efficiencies for the formation of H_2, HCOOH, CO, and CH_3COOH according to thermal oxidation time of the Cu foils at 500 °C. Potential was fixed at –0.5 V *vs.* RHE for all samples.

The diversity of product composition through the adjustment of thermal oxidation conditions, leading to control of the surface morphology, affords this material tremendous versatility and marks a promising step towards addressing the longstanding challenge of product selectivity. The goal of subsequent tests, then, is to determine the degree to which the production of certain liquid fuels may be favored. The more that unwanted products are suppressed, the more that electrons are fruitfully directed towards producing only the liquid fuel of interest. In terms of producing fuels such as methanol and ethanol as final products, the current results showing the dramatic shift in selectivity towards CO is extremely promising given that CO is a precursor to these fuels. Alternatively, the significant production of H_2 alongside CO at both oxidation temperatures should not arouse too much concern, as the Fischer-Tropsch process is a proven and reliable method for converting these gases, known collectively as syngas, into useful fuels such as gasoline or diesel.

A comparison of selectivities for H_2, CO, HCOOH, and CH_3COOH according to thermal oxidation time at 500 °C is provided in **Fig. 2.25**. The average selectivities for H_2, CO, HCOOH, and CH_3COOH are 47%, 18%, 32%, and 3%, respectively, and they appear to be insensitive to changes in oxidation time. It is worth noting the specific proportions of CO and H_2 gas formed here, a H_2/CO ratio of ~2.6 on average. The ideal H_2/CO ratio for maximized production of liquid fuels from syngas *via* the Fischer-Tropsch process is 2.[56] Since the H_2/CO ratio was less than 1 for the case of Cu foil oxidized at 500 °C for 2 hr and reduced at a constant current of –5 mA as shown in **Fig. 2.23**, it is conceivable that any ratio between 1 and 2.6, including the ideal ratio of 2, can be obtained with the appropriate combination of thermal oxidation conditions during copper oxide growth and electrochemical conditions during copper oxide reduction.

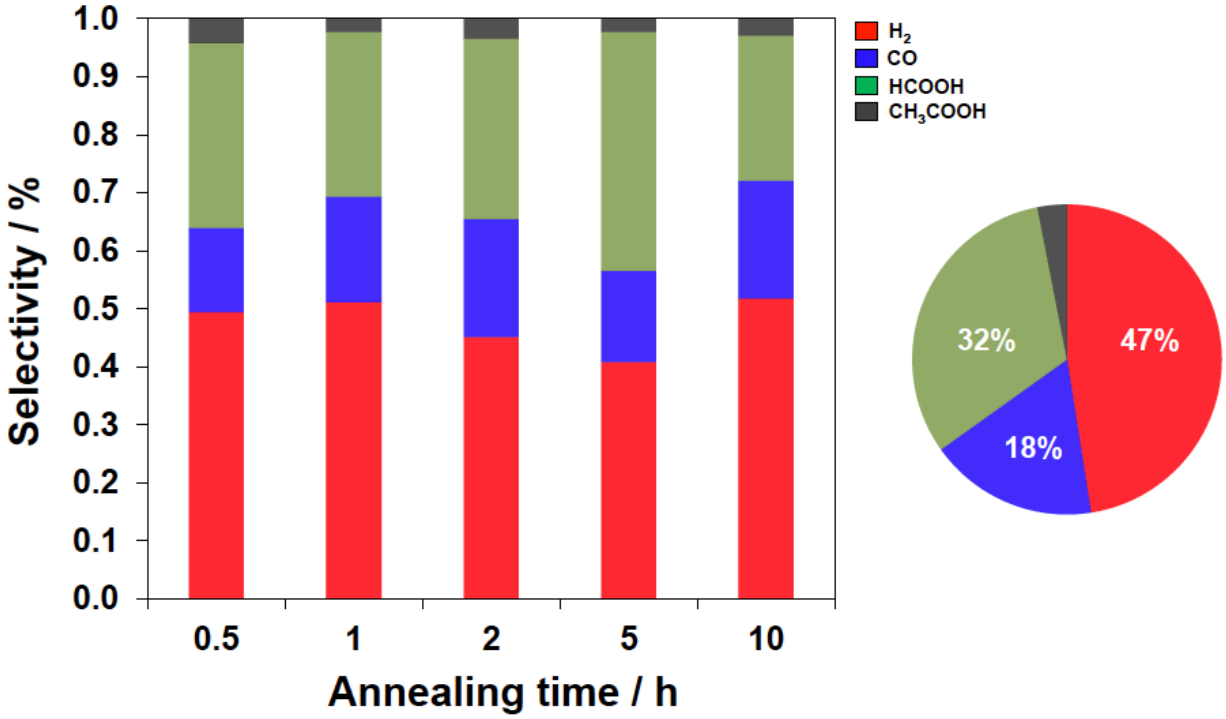

Figure 2.25 Selectivities of the formation of H_2, CO, HCOOH, and CH_3COOH for samples thermally oxidized at 500 °C for 0.5, 1, 2, 5, and 10 hr. Potential was fixed at –0.5 V *vs.* RHE for all samples.

The results presented have far-reaching implications not only on Cu-based electrodes but also for metal-based electrodes in general. Consequently, the advantages of these electrodes are worth reiterating. A simple synthesis method was employed to grow copper oxide electrodes that are electrochemically reduced to reveal Cu sites for CO_2 reduction. The resulting surface morphology consisting of either planar Cu_2O or a vertically aligned array of CuO nanowires, subsequently give rise to different phases of Cu during electrochemical reduction. The end result is the formation of different proportions of H_2, CO, HCOOH, and CH_3COOH. The control of product composition by tuning thermal oxidation conditions could make preferential formation of certain liquid fuels very straightforward. For instance, the formation of CO can be favored for a specific combination of thermal oxidation temperature and time, while the formation of syngas with H_2/CO ratio of 2 can be favored for another set of oxidation conditions. It remains to be seen whether unwanted reactions can be completely suppressed, but the simplicity of tuning the proportions of each reaction product should be considered for future work as the search for reduction pathways and electrode materials continues with the goal of selective and efficient liquid fuel production at low overpotentials.

2.3 Conclusions

The versatility of copper oxide for electrocatalysis has been demonstrated for two specific applications: photocatalytic water splitting and CO_2 reduction. Both applications were enabled using one simple synthesis process for copper oxide: thermal oxidation of Cu foil. For photocatalytic water splitting, large photocurrents as large as 0.8, 1.3 mA/cm^2 for the planar

Cu_2O photocathodes and 2.7 mA/cm^2 for the planar Cu_2O with CuO nanowire photocathodes were measured under 100 mW/cm^2 AM 1.5 illumination at 0 V *vs.* RHE. These photocurrents are noteworthy as no Pt co-catalyst nanoparticles were used to enhance charge transfer and surface reactivity. For comparison, most prior studies report photocurrents as high as only 0.3 mA/cm^2 for pristine copper oxide photocathodes, and a recent study observed a photocurrent enhancement from several microamperes per square centimeter to 2.4 mA/cm^2 at 0.25 V *vs.* RHE. Therefore, the photocathodes synthesized by thermal oxidation of Cu foil fare extremely well. The results of this study highlight the possibility of high performance, cost-effective metal oxide photocathodes using facile synthesis methods. Two explanations were provided to explain the large photocurrent: improved carrier collection owing to larger diffusion length for electrons and holes, and a large electric field on the surface of the photocathode caused by a narrow depletion region. Although the photocurrent was not stable for prolonged illumination, the large photocurrent is a promising development for future work. Photocurrent decay is caused by electrons that are not quickly shuttled into the electrolyte and are allowed to participate in photocorrosion by reducing the copper oxides to Cu. If there is a method to quickly transfer all photogenerated electrons into the electrolyte before they reduce the copper oxides, both photocurrent and stability should improve.

For CO_2 reduction, copper oxide photocathodes served as precursors for CO_2 lysing on Cu active sites revealed during electrochemical reduction. Reaction products H_2, CO, HCOOH, and CH_3COOH were produced on these Cu sites in proportions strongly dependent on the conditions used for thermal oxidation of the Cu foil. It is presumed that the specific morphology on the surface of the oxidized foil is conducive to the production of specific products. An increase of oxidation temperature from 300 °C to 500 °C yielding the formation of CuO nanowires caused a reversal of dominant products produced, from an H_2 dominant process to a CO dominant process. The possibility of tuning the reaction products based on the original oxidation conditions may ultimately address the longstanding concern of low selectivity. Alternatively, H_2 can be allowed for the production of syngas with a H_2/CO ratio of 2. This ratio is optimal for the production of liquid fuels through the Fischer-Tropsch process. This simple control of product selectivity will hopefully encourage similar studies of other metal-based electrodes for CO_2 reduction.

Chapter 3: Copper Oxide for Gas Sensors

3.1 Motivation

Gas sensors based on metal oxide semiconductors are attractive gas sensing technologies owing to their simplicity of use, commercial cost-effectiveness, and versatility in the variety of gases that can be sensed. As is the trend for all sensing technologies, one of the goals of continuing research efforts is to improve sensitivity. To this end, Yamazoe reported one way of achieving this by reducing crystal grain size.[57] The guiding principle is illustrated in **Fig. 4.1**. In micro-sized grains, the depletion regions occupy only a fraction of each grain, so the bulk conductivity of the semiconductor is largely determined by the presence of non-depleted regions. When impinging gas species donate or remove free electrons, the change in bulk conductivity is insignificant because the material remains largely conductive. Conversely, in the case of nano-sized grains, the depletion regions fully occupy each grain, resulting in a significant decrease in the bulk conductivity of the semiconductor. In this case, when a free electron is donated or removed, the change in conductivity is much more pronounced, and therefore its sensitivity to impinging gas species is greater. The desire to reduce crystal grain size has been a motivator for heightened interest in nanostructured semiconductor gas sensing materials such as nanowires. The dramatic increase in surface area-to-volume ratio at these nanometer length scales provides gas species more surface area to react with the sensing material.

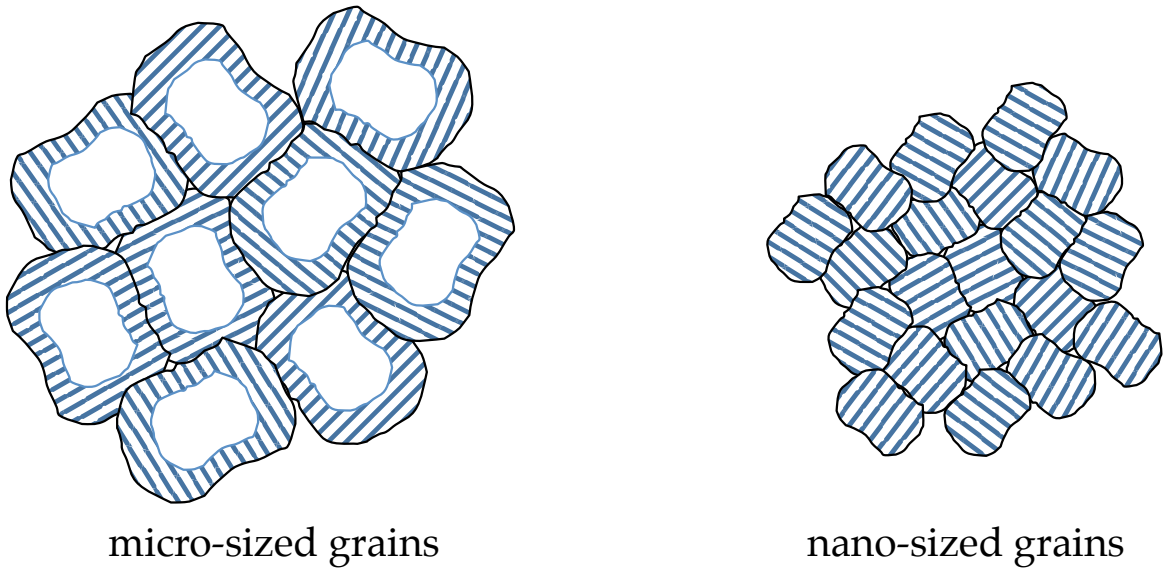

Figure 3.1 Comparison of the influence of grain size to bulk conductivity and gas sensitivity. Depleted regions are denoted with cross-hatching, and the non-depleted regions are denoted in white. When the grains shrink to nanometer scale, the grains are fully depleted, rendering them more sensitive to changes in carrier concentration caused by impinging gas species.

While the potential performance improvements afforded by metal oxide nanowires are quite promising, harvesting these nanowires for incorporation into gas sensing devices often requires laborious, expensive, and fabrication-intensive post-processing. Fundamentally, the nanowires must be electrically accessible through the formation of metal contacts, and some portion of the surface serving as the active region of the semiconductor must remain exposed to allow gas species to impinge and react. Blanketing the surface with a metal thin film *via* thermal evaporation or sputtering will provide the required electrical access, but no active areas will remain for the semiconductor to react with gas molecules.

To date, area-selective formation of metal contacts using electron-beam lithography is the most common method for establishing electrical access to nanowire-based gas sensors. For the case of single-nanowire gas sensor devices, this requires the nanowire to be removed from its growth substrate and then deposited onto the device substrate, typically through a dropcast method, followed by lithography and a metal lift-off process.[58] For the case of multiple-nanowire gas sensor devices, some have attempted to randomly deposit nanowires onto a substrate with preexisting comb electrodes.[59] Nanowires bridging the gap between the electrodes would then participate in gas sensing, although the likelihood that the nanowires would form low-resistance, ohmic contacts is poor. Nanoparticle-based gas sensors can be formed in a similar fashion with nanoparticles dropcast or spincast onto the device substrate.[60] Alternatively, others have also attempted to grow nanowires using a vapor-liquid-solution technique from

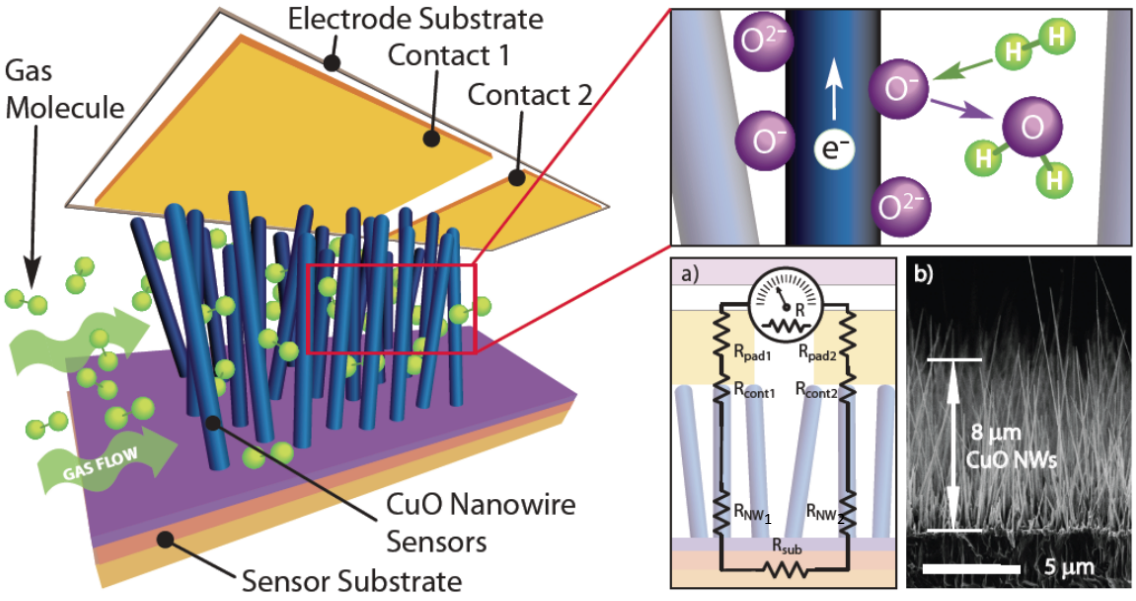

Figure 3.2 Concept of CuO nanowire array hydrogen sensor *via* facile top contact integration. The surfaces of the nanowires remain exposed, allowing gas molecules to enter the device and adsorb onto the CuO nanowires. The inset illustrates the reduction of preadsorbed O^- and O^{2-} anions to form water. Meanwhile, electrons are injected into the *p*-type CuO nanowires. (*a*) Circuit diagram of the system showing the pertinent resistances acting in series. (*b*) SEM cross-sectional micrograph showing the CuO nanowire array grown to an average height of 8 μm after a 2 hr oxidation at 500 °C.

interdigitating electrodes that serve as both the catalyst for nanowire growth and the base contact for the nanowires. Nanowires growing from each electrode that come into physical contact with one another construct an electrical pathway from one electrode to the other to complete the device.[61] Unfortunately, poor yield or repeatability due to the challenge of forming ohmic contacts and the variation in electrical properties for individual nanowires are continuing concerns for these devices.

Herein, a novel nanowire-based gas sensor as shown in **Fig. 4.2**, is presented that circumvents many of the tedious post-processing steps that have been reported in the literature. In this device, CuO nanowires serve as the active material. The copper oxides are grown via simple thermal oxidation of Cu foil at a temperature of 500 °C for 2 hr. Conductive contact pads are pressed atop the tips of the nanowires to electrically access the nanowire array. The key to completing the circuit from one pad to the other is the presence of the electrically conductive Cu substrate. As a result, the total resistance of the system may be measured from one conductive pad through a collection of nanowires down to the substrate, and back up through another collection of nanowires into the other conductive pad. The resistance change of the entire system can primarily be traced to the resistance change of the CuO nanowires and indicate the presence of a reducing gas species. The advantages of this device are:

(1) *Facile, one-step synthesis of nanowires*. No high vacuum processing for thin-film catalyst deposition or nanowire growth is needed. The nanowires can be grown directly from the Cu foil through control of thermal oxidation time and temperature.

(2) *Convenient electrical access to nanowires.* By virtue of the vertically-aligned nanowire array, the nanowires can be contacted at the tips.

(3) No electron beam photolithography. This greatly simplifies the assembly of the device. No intricate photolithographic patterning of catalyst metals for nanowire growth is needed, nor is it needed in the formation of the contact pads.

(4) Usage of large area nanowire arrays. Yield issues resulting from non-ohmic contacts and inconsistent electrical properties from nanowire to nanowire are circumvented.

(5) *Reusability of contacts*. The same contacts pads can be used to characterize entire batches of as-grown nanowire array samples because they are not permanently attached.

(6) *Compatibility with all nanowire arrays grown on conductive substrates*. This architecture is applicable not only to CuO nanowires, but also to any nanowire array attached to a conductive substrate. More generally, any device

applications that depend on nanowires as the active material may also benefit from this facile contact integration process.

In essence, this architecture presents the possibility of harvesting nanowires in a convenient assembly process, thereby capitalizing on the increased sensitivity afforded by the nanowire grain structure and geometry.

CuO nanowire arrays possess several properties that make it an attractive material for integration this top contact gas sensing scheme. The nanowires mostly grow vertically from the oxidized Cu foil, readying them for immediate contact integration. The nanowire geometry also affords large surface area-to-volume ratio, providing more reactive sites on which gas species can be adsorbed. Since Cu foil is the starting substrate, a conductive pathway is automatically provided by the presence of Cu that is not consumed during thermal oxidation. Therefore, no subsequent nanowire transfer is needed; the nanowire array is ready for contact integration immediately after oxidation. Furthermore, the nanowire synthesis process is extremely simple. As opposed to most growth methods requiring the presence of a metal catalyst layer, the nanowire growth is self-sourced. Copper foils can be oxidized immediately without any modification prior to oxidation.

A variety of metal oxide semiconducting materials including ZnO, TiO_2, and SnO_2 have been used for H_2 sensing. Of these materials, ZnO and TiO_2 have garnered the most attention. Tien *et al.* used Pt-coated ZnO nanorods to achieve a threefold current response for room temperature exposure to 500 ppm H_2. The ZnO nanorods were grown from Au catalyst islands in a molecular beam epitaxy process of Zn metal and O_3/O_2 plasma discharge. Subsequently, Pt thin films of ~10 Å thickness were deposited by sputtering. To form electrical contacts to the ZnO nanorods, sputtered Al/Ti/Au top contacts were patterned by lift-off.[62] Rout *et al.* prepared ZnO nanowires exhibiting a sensitivity of ~40 at an operating temperature of 150 °C for 1000 ppm H_2. The nanowires were prepared *via* electrophoretic deposition in anodic alumina membrane templates.[63]

For the case of TiO_2 based H_2 sensors, Mor *et al*. reported a 10^4 decrease in resistance in response to 1000 ppm H_2 concentration at room temperature using TiO_2 nanotubes obtained *via* anodized titanium thin films. Contacts were formed with 10 nm of Pd *via* thermal evaporation followed by 40 nm of Pt *via* sputtering.[64] Varghese *et al.* reported similar findings, and their device required the deposition of Pt contact pads on the nanotube array as well.[64] To date, these TiO_2 based sensors exhibit the largest sensitivities of any H_2 gas sensors. Wang *et al*. reported SnO_2 based H_2 sensors enabled through the physical contact of SnO_2 nanowires growing from neighboring comb-shape interdigitating electrodes. The electrodes were fabricated with a lift-off process consisting of 300 nm of Cr and 100 nm of Au *via* sputtering. Nanowire growth was achieved with carbon and SnO_2 co-evaporation at 950 °C. For a concentration of 1000 ppm, the sensor registered a sensitivity of ~3.3 at an operating temperature of 300 °C.[61] Shukla *et al.* achieved detection of 100 ppm concentration at room temperature using In_2O_3-doped SnO_2 thin films. A sol-gel dip-coating technique was used to deposit the films on glass substrates, and a twofold increase in resistance was measured for 3-4% volume of H_2.[65]

As for CuO nanowire based H_2 sensors, Hoa *et al*. thermally oxidized Cu wire at 400 °C in 0.5 hr and the resulting nanowires were ultrasonically detached, suspended in methanol, and sprayed onto patterned Au/Ta comb electrodes. A sensitivity of ~2 was measured for 6% H_2 concentration at an operating temperature of 250 °C.[59] Another report from the same group used CuO-SWNT nanocomposites synthesized through thermal oxidation of sputtered Cu on a porous SWNT mat.[66] Ohmic contacts were provided by Pt electrodes.

For most of these devices, either the synthesis of the active material or its integration into the gas sensing device required several laborious and expensive fabrication steps. Moreover, it appears that these gas sensors assumed very similar device architectures, and little innovation has been introduced with the goal of simplifying and facilitating the integration of nanowires into devices. Presumably, relaxing the need for fabrication intensive processing, as demonstrated by this novel top contact device scheme, will make nanowire-based gas sensors very attractive and practical commercially, as well as encourage more innovative and elegant device schemes.

3.2 Theory

3.2.1 Circuit Model

Gas sensing using metal oxide semiconductors can be broken down into three fundamental processes: (1) physisorption of impinging gas species onto the semiconductor surface, (2) chemisorption involving electron exchange between the gas species and surface, and (3) resistivity change due to the presence of electrons. In the case of a reducing gas species reacting with a *p*-type semiconductor such as CuO, electrons decrease the majority carrier concentration, thereby increasing resistivity.[67] Carrier concentration is directly related to resistivity ρ through the formula:

$$\rho = \frac{1}{q(\mu_n n + \mu_p p)} \tag{3.1}$$

where μ_n and μ_p are the electron and hole mobilities, n and p are the electron and hole concentrations, and q is the charge of an electron. In a *p*-type semiconductor, the $\mu_n n$ term can essentially be disregarded since $\mu_p p$ is the dominant term, so the injection of electrons serves only to decrease hole concentration p. The resistance of the entire device can be modeled as a sequence of resistances in series as drawn in **Fig. 3.2(a)**. Note that R_{NW1} and R_{NW2} denote the collective resistance of all nanowires contacting each pad, with each collection of nanowires arranged as parallel resistances.

In general, for large concentrations as those tested in **Chapter 3.4.3**, the sensitivity is independent of the number of connections because there is an abundance of H_2 molecules in the environment, sufficient to alter the resistance of every nanowire in the array over time from the gas diffusion process. The expression for sensitivity is:

$$S = \frac{R - R_0}{R_0} = \frac{\frac{xR}{N} - \frac{R}{N}}{\frac{R}{N}} = x - 1 \tag{3.2}$$

where x denotes the resistance change factor due to the absorption of gas under the specific gas concentration. Thus, the sensitivity of the device is determined by the range of gas concentrations to be detected.

3.2.2 Temperature Dependence of CuO

For gas sensing of H_2, it is important to note the conductivity of CuO as a function of temperature. Past reports show that H_2 sensing is normally performed at temperatures exceeding 250 °C.[59, 66] Since CuO nanowires have a band gap of ~2 eV, its electrical conductivity at 250 °C will be significantly increased due to the thermal excitation of carriers across the semiconductor band gap, which increases the carrier concentration. Therefore, the resistance of the device should be noticeably different from the moment it is first assembled at room temperature to the moment it is under operation. For the case of CuO, a *p*-type semiconductor, **Eq. 3.3** can be simplified to the terms pertaining to holes since the terms for electrons contribute negligibly:

$$\rho \approx \frac{1}{q\mu_p p} \tag{3.3}$$

In this expression, both hole mobility μ_p and hole concentration p are temperature dependent parameters. An empirical model is used to obtain values for hole mobility. The expression for p is given by

$$p = N_v e^{-(E_F - E_v)/kT} \tag{3.4}$$

where the effective density of states for the valence band N_v is also temperature-dependent:

$$N_v = 2\left(\frac{2\pi m_p^* kT}{h^2}\right)^{3/2} \tag{3.5}$$

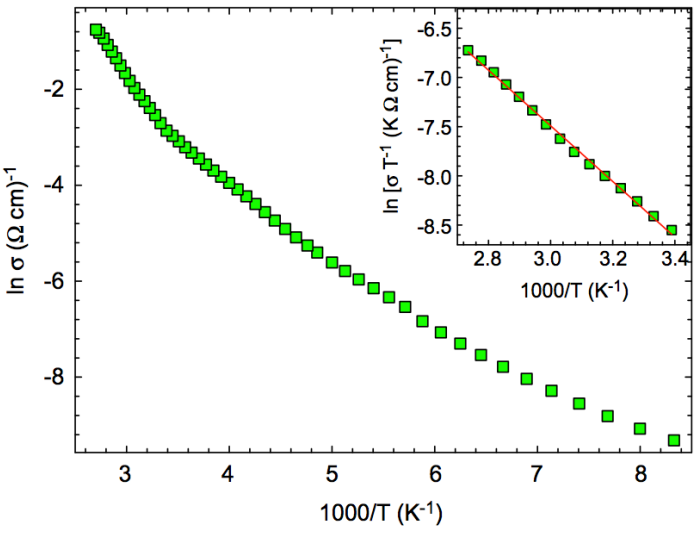

Figure 3.3 Conductivity dependence of CuO on temperature.[68]

This temperature dependence is reflected in measurements performed by Serin *et al*. of electrical conductivity of bulk CuO for a wide range of temperatures, shown in **Fig. 4.5**.[68] Note that these values may be slightly different than those for CuO nanowires grown *via* thermal oxidation, especially because their CuO thin film was grown using solution-based methods. Monitoring the resistance of the device as temperature is increased can offer insight into the quality of the contacts between the pads and nanowires. Ideally, the connections should remain intact throughout the heating process, and this can be confirmed by comparing the total device resistance before and after heating. With knowledge of the resistivity of CuO at both temperatures, the number of connections can be calculated for both cases. A significant change in the number of connections as a result of the heating process will warrant closer examination into possible causes.

3.3 Experimental Setup

The assembly of the CuO nanowire H_2 sensors is as follows. Copper foil of 25 μm thickness, 99.98% purity from Sigma-Aldrich were cut into coupons of size 1 cm × 2.5 cm and tightly wrapped around glass microscope slides. The samples were then thermally oxidized atop a hot plate at 450 °C for 2 hr. At the end of the oxidation process, the samples were removed and placed on a chilling plate to return the samples to room temperature. The samples were

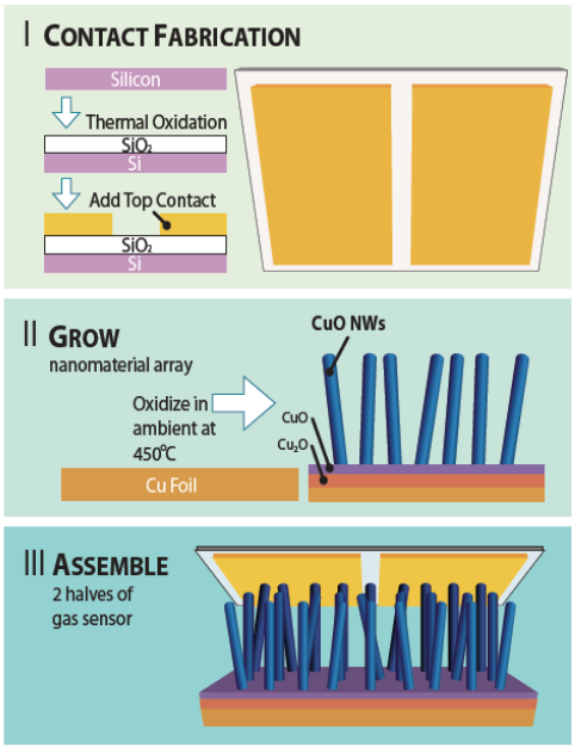

Figure 3.4 Fabrication sequence for the CuO nanowire H_2 sensors consisting of the formation of top contact pads, CuO nanowire array growth *via* thermal oxidation of Cu foils, and gas sensor assembly through mechanical depression of the contacts atop the nanowire array.

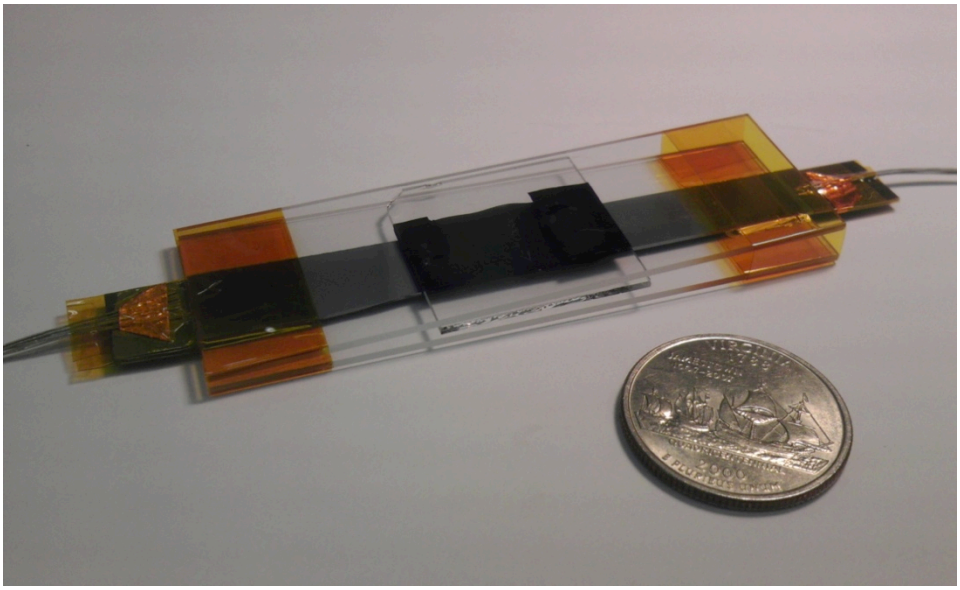

Figure 3.5 Photograph of a completed CuO nanowire H_2 sensor with Sn foils in contact with a CuO nanowire array sample, sandwiched between two glass microscope slides. A U.S. nickel is placed adjacent for size comparison.

Figure 3.6 Photograph of the Lindberg/Blue M three-zone tube furnace that was used for H_2 sensing tests.

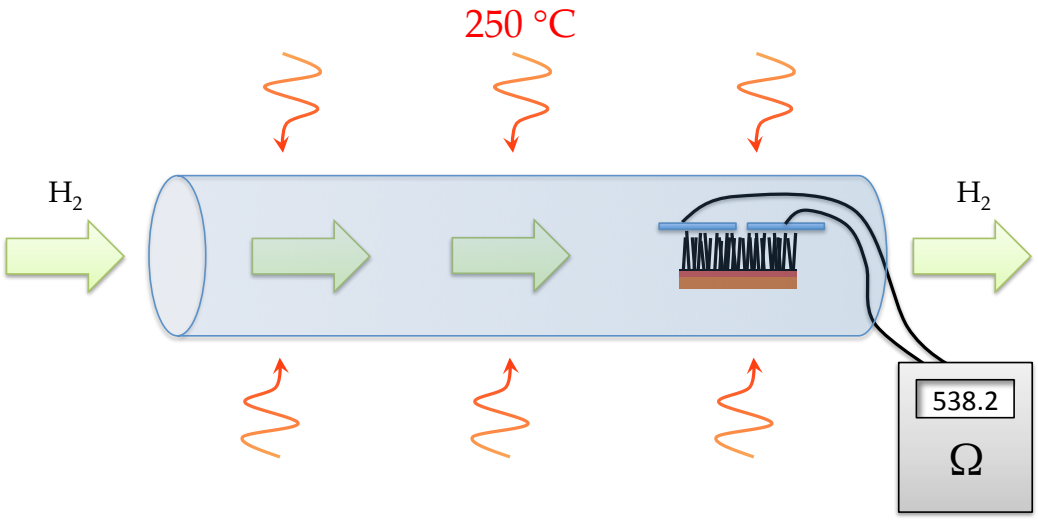

Figure 3.7 Schematic of the H_2 sensing apparatus. The quartz tube is uniformly heated at 250 °C as H_2 is flowed inside at various concentrations. Two electrical wires from the device run through one O-ring seal of the quartz tube to an ohmmeter.

analyzed in a Siemens D5000 x-ray diffractometer to verify the elemental composition of the oxidized foil. Two strips of Sn foil were used as the top contacts to the nanowires. These strips were pressed atop the nanowire array by sandwiching the Sn foil and oxidized Cu foil between two glass microscope slides secured by Kapton® tape. The quality of electrical contact between the nanowires and Sn foils was evaluated through an I-V measurement using a Hewlett-Packard 4156A Precision Semiconductor Parameter Analyzer outputting data to a laptop computer. A customized LabVIEW data analysis program recorded and plotted the data points. Finally, electrical wires were attached to the Sn foils using Ag paste and epoxy. A summary of the assembly process is illustrated in **Fig. 3.4**, while a photograph of a completed CuO nanowire H_2 sensor is provided in **Fig. 3.5**.

Hydrogen sensing measurements were performed inside a Thermo Scientific Lindberg/Blue M three-zone tube furnace as shown in **Fig. 3.6**. The samples were inserted into a

H_2 (sccm)	Ar (sccm)	O_2 (sccm)	H_2 concentration (%)
10	450	112.5	**8.1**
15	425	106.3	**12.4**
20	400	100.0	**16.7**
25	375	93.8	**21.1**
30	350	87.5	**25.5**

Table 3.1 Summary of H_2, Ar, and O_2 gas flows, and the resulting H_2 concentrations.

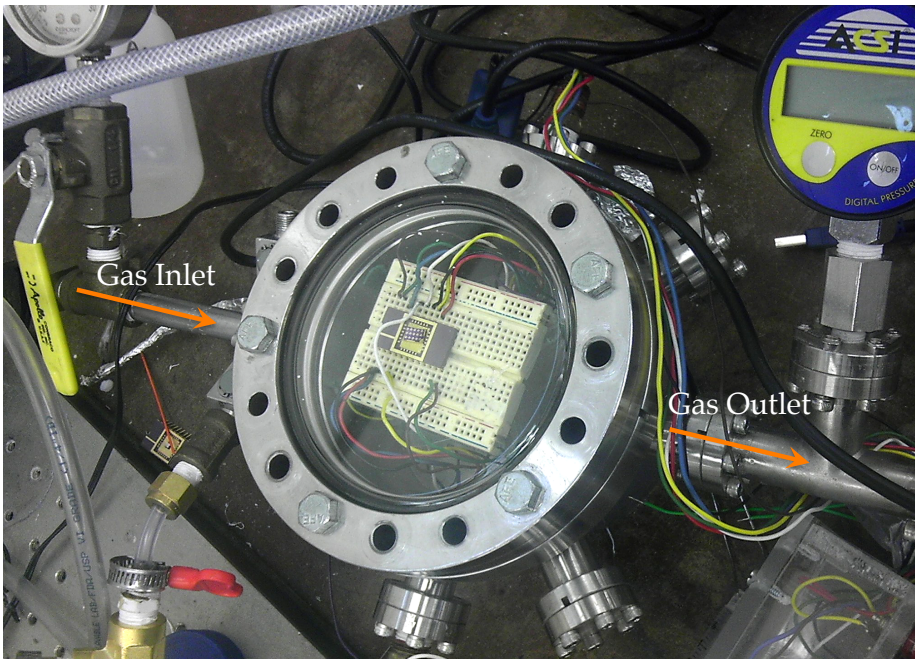

Figure 3.8 Gas sensing chamber equipped with breadboard to provide remote electrical access for localized Joule heating and data acquisition of microheater-integrated gas sensors.

2 in diameter quartz tube resting inside the furnace, and both ends of the tube were closed with O-ring seals in preparation for vacuum pump down and controlled flow of gases. To ensure that gases passing through the device have heated to 250 °C, the samples were positioned in the center of the temperature zone nearest the outlet of the quartz tube. All three temperature zones were set at 250 °C while the system was pumped down. The temperature for all three zones stabilized after approximately 0.5 hr. Combinations of H_2, Ar, and O_2 gas flows were used to mimic the presence of H_2 in air, which was simulated through a mixture of Ar and O_2. With the gas flows as listed in **Table 3.1**, H_2 concentrations of 8.1%, 12.4%, 16.7%, 21.1%, and 25.5% were flowed in sequence with air purging steps in between to return the resistance of the device to its original value before the next H_2 concentration was tested. All measurements were taken with a Hewlett-Packard 34401a digital multimeter.

For preliminary testing of microheaters, a custom-built gas sensing chamber, as shown in **Fig. 3.8,** was used. The gas sensor is secured inside the chamber and connected to the breadboard, and electrical wires are routed from the breadboard to facilitate communication between the gas sensor inside the chamber and power source (Hewlett-Packard E3615A) and digital multimeter outside the chamber. To correlate power input to microheater temperature, the input current and voltage from the power source were monitored along with temperature as measured using a thermocouple. This correlation provided an approximate means of estimating the microheater temperature inside the vacuum-sealed chamber using knowledge of the input power.

3.4 Facile Contact Quality and Performance

3.4.1 Force Dependence of Resistance

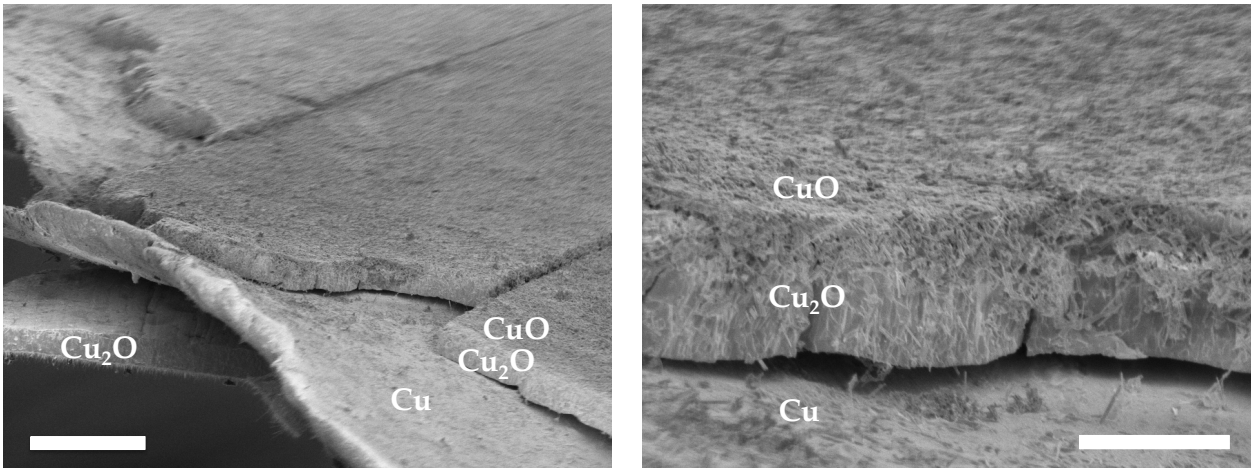

Figure 3.9 SEM micrograph top view of a Cu foil oxidized at 500 °C for 2 hr (*left*) and close-up view showing the compressed nanowire film (*right*). The nanowires were mechanically flattened using a technicloth in a wiping motion. Scale bars: 40 μm and 10 μm.

The facile nature of the assembly process for the CuO nanowire array H_2 sensors naturally arouses questions about the quality of the contacts between the pads and the nanowires. Conceivably, there are both advantages and disadvantages to providing insufficient and excessive force in pressing the pads atop the nanowire array. Insufficient force could lead to the presence of nonohmic contacts, and changes in the electrical conductivity of the nanowires may not be communicated to the contact pads. Conversely, excessive force provides greater assurance that Ohmic contacts are established between the nanowires and pads, but it possibly leads to the situation of flattened and compressed nanowires depicted in **Fig. 3.9**.

Correlations between force applied to affix the contact pads to the nanowires and the resulting device resistance were measured as shown in **Fig. 3.10**. For forces below 0.5 N, the resistance remains in the range of tens of mega-ohms; plausibly, when the device is introduced into operating temperatures, this resistance will decrease substantially as free carriers receive sufficient thermal energy to bridge the band gap. As forces exceed 0.6 N, the resistance takes a precipitous drop into the several hundred kilo-ohm range. For the data point at 0.6 N yielding a device resistance of 600 kilo-ohms, current-voltage measurements were obtained to assess the quality of electrical contact between each top contact pad and the nanowires. The contact pads were probed for this measurement, meaning that this *I-V* response accounts for all the resistances in the entire system. The *I-V* response here is linear, suggesting good quality ohmic contacts formed between the contacts pads and nanowires. Ohmic contacts are critically important for highly sensitive gas sensors, and this result provides confirmation that electrical access to the nanowire array was effectively established.

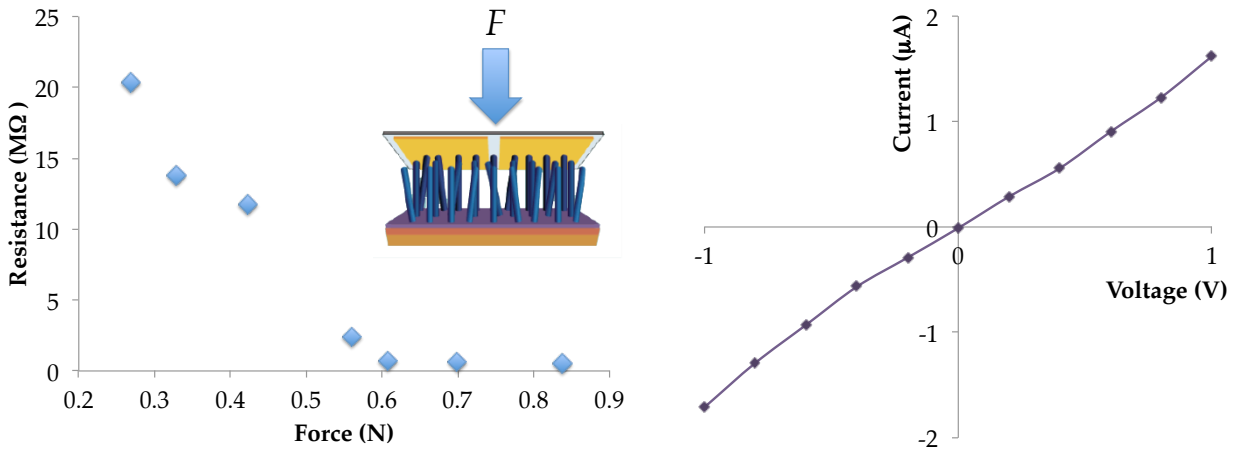

Figure 3.10 Dependence of device resistance on the amount of force applied in pressing the top contacts onto the CuO nanowire arrays (*left*), and the resulting *I-V* response for an applied force of 0.62 N and device resistance of 600 kilo-ohms (*right*). The *I-V* curve shows the desired ohmic response for this applied force, ensuring high quality contacts between the nanowires and contact pads.

Using these two plots, a general strategy for maximizing the sensitivity of this device is as follows. A small quantity of force is applied to affix the contact pads to the nanowire array, and more force is applied until a resistance value can be measured through the entire device. The other requirement afterwards is to observe an ohmic response for the *I-V* characteristic. If the response is not ohmic, the process is repeated until the applied force is sufficient to yield ohmic contacts.

3.4.2 Resistance Change During Temperature Ramp-Up

As the resistance of the CuO nanowires changes significantly with temperature, it is important to monitor the resistance change as the device is brought into operating conditions. This is because subsequent resistance changes of the nanowires in response to impinging H_2 molecules should be compared against the initial resistance of the device at operating temperature instead of the resistance measured immediately following device assembly at room temperature. Resistance was recorded for a device with applied force of 0.7 N over a time period of 400 s as temperature was increased from 25 °C to 250 °C. Regarding the resistances of the collection of nanowires as R_{NW1} and R_{NW2} in series, and as the only significant resistances in the system, while assuming that the same number of connections was made on each pad, the number of connections N can be calculated:

$$R_{total} \approx 2\left(\frac{N}{R}\right)^{-1} \tag{3.6}$$

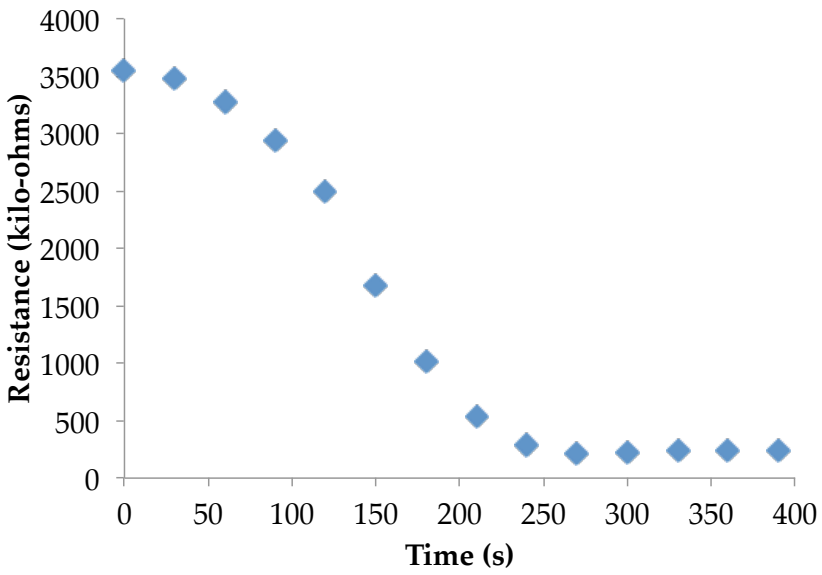

Figure 3.11 Device resistance recorded as the CuO nanowire array H_2 sensor is heated from room temperature to 250 °C. Force applied for this device is 0.7 N.

It is very difficult to analyze the experimental data as each nanowire could be slightly different. Here, a first-order approximation is applied by using results from other works. For CuO nanowires 8 μm in length, 100 nm in diameter, and resistivity of 60 Ω–cm,[69] each nanowire contributes $R_{25°C}$ = ~600 MΩ. Since the initial resistance of the device for the test of **Fig. 3.11** is 3550 kΩ, the number of nanowire connections for each contact pad is estimated as:

$$N \approx \frac{2R_{25°C}}{R_{total,25°C}} = \frac{2*600{,}000\ \text{k}\Omega}{3550\ \text{k}\Omega} = 340 \qquad \textbf{(3.7)}$$

At a steady temperature of 250 °C, the resistance has dropped to 210 kΩ. Assuming the same number of connections, the value of $R_{250°C}$ can be calculated:

$$R_{250°C} \approx \frac{NR_{total,250°C}}{2} = \frac{340*210\ \text{k}\Omega}{2} = 36\ \text{M}\Omega \qquad \textbf{(3.8)}$$

This corresponds to a resistivity of 3.5 Ω–cm. This value is consistent with reports that the resistance should be at least one order of magnitude smaller at 250 °C.[68]

There are several possible reasons for the large resistivity. One contributor, as suggested previously, is the loss of nanowire contacts. The tin foil strips used as the contact pads and the oxidized Cu foil both undergo thermal expansion, and the connections made at room temperature may have been perturbed enough to become disconnected as both elements continued to expand. Alternatively, the CuO nanowires grown for these devices may possess inherently larger conductivity compared to those grown by Tsai *et al*., who used process temperatures of 200 °C, 300 °C, and 400 °C for their nanowire synthesis.[69] Higher synthesis temperature may yield nanowires with greater crystallinity and larger conductivity. Nonetheless, exact measurements of nanowire resistivity at both 25 °C and 250 °C using single-nanowire devices would prove

useful in explaining the heating curve of **Fig. 3.11**, and is a possible task to be undertaken in future work.

3.4.3 Resistance Change *vs.* H_2 Concentration

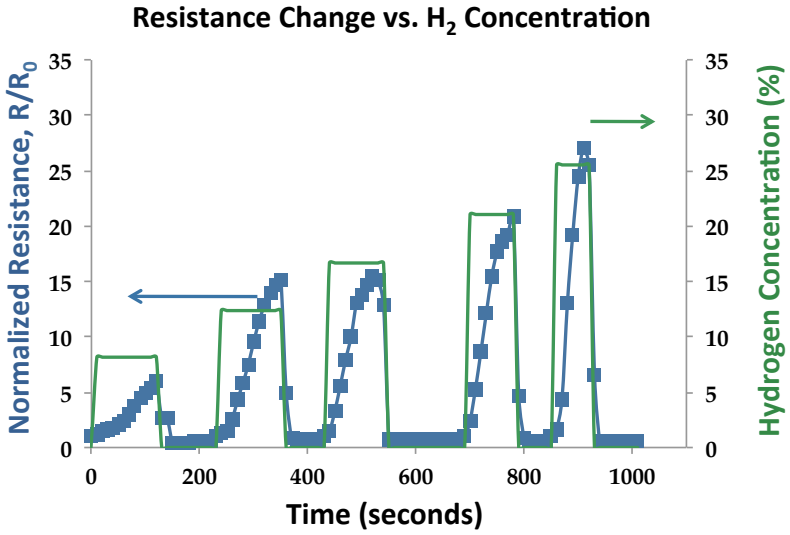

Figure 3.12 Change of resistance in response to increasing H_2 concentration at an operating temperature of 250 °C. As expected, resistance increases with increasing H_2 concentration. Recovery while purging with air is rapid at less than 30 s.

For an initial system resistance of 400 kΩ, the resistance change of the device was measured as a function of H_2 concentration as shown in **Fig. 3.12**. The resistance change increases for increasing H_2 concentration, starting from a resistance change R/R_0 of ~6 at 8.1% concentration and finally reaching ~26 for 25.5% concentration. The tops of the peaks show a linear increase that does not plateau, suggesting the presence of ample reaction sites on the nanowire surfaces for H_2 molecules to adsorb. For reference, Hoa *et al.* report a comparable resistance change of ~5 for a concentration of 6% at the same operating temperature. The recovery time, the period when the chamber is purged with air to return the system to its original resistance, is extremely brief at ~0.5 min or less. In contrast, Hoa *et al*. reported much longer recovery times on the order of 10 min. Their device used the transfer of CuO nanowires from the growth substrate onto a pair of pre-patterned Au/Ta electrodes.[59] This could add difficulties in the gas desorption process. Lastly, upon purging, the resistance consistently returns to the same initial value, showing that the device is completely reversible and does not show any noticeable hysteresis.

One interesting feature of the resistance curve is the asymmetry in rise and recovery times. The time period for resistance rise averaged about 100 s for each concentration tested. One possible explanation for this asymmetry is the method by which gases are introduced into the gas sensing apparatus. The air purging step is merely a venting process in which ambient air rushes into the quartz tube, while the resistance rise is triggered by a controlled introduction of H_2–Ar–O_2 mixture at a limited flow rate. Therefore, a more rapid insertion of H_2 species

could result in an improved rise time. Nonetheless, the rise time is still comparable to the literature.

3.5 Facile Contact with Microheater Integration

3.5.1 Motivation

The implementation of top contacts for CuO nanowire array H_2 sensors as discussed is versatile and suitable for all nanowire-based materials anchored to an electrically conductive substrate. This versatility should suffice not only for gas sensor devices but also for a wide variety of nanowire-based technologies that would benefit from this facile contact strategy. The advantages of instantly harnessing as-grown nanowires for device integration without the need for e-beam lithography and other expensive, labor-intensive processing cannot be understated.

To advance this device paradigm further for gas sensing application, a means of incorporating a microscale heating element into the top contact pads would enable sensing of a more diverse collection of gas species at elevated temperatures. In the case of CuO nanowires, H_2S sensing has been demonstrated at room temperature, but CO and H_2 sensing require temperatures as high as 250 °C for maximized sensitivity. With the addition of integrated heating, all the necessary elements needed for a fully functional gas sensor are engineered into one device that is affixed atop the nanowire array.

A schematic for the proposed device is illustrated in **Fig. 3.13**. The top contact pads are the same as previously discussed with the addition of a serpentine heating element embedded in

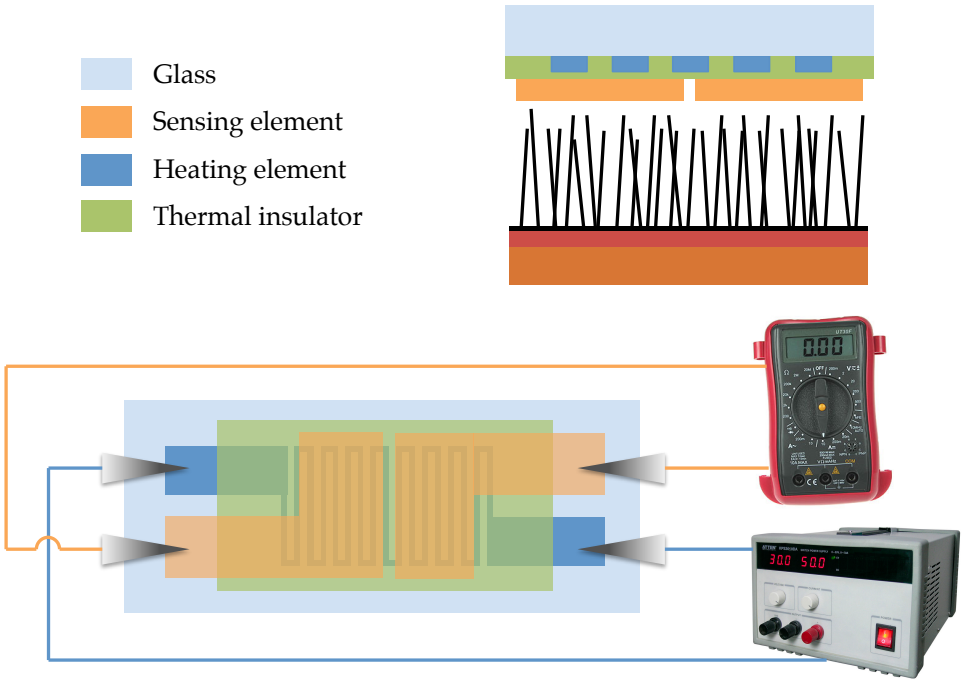

Figure 3.13 Schematic of a microheater-integrated CuO nanowire array H_2 sensor.

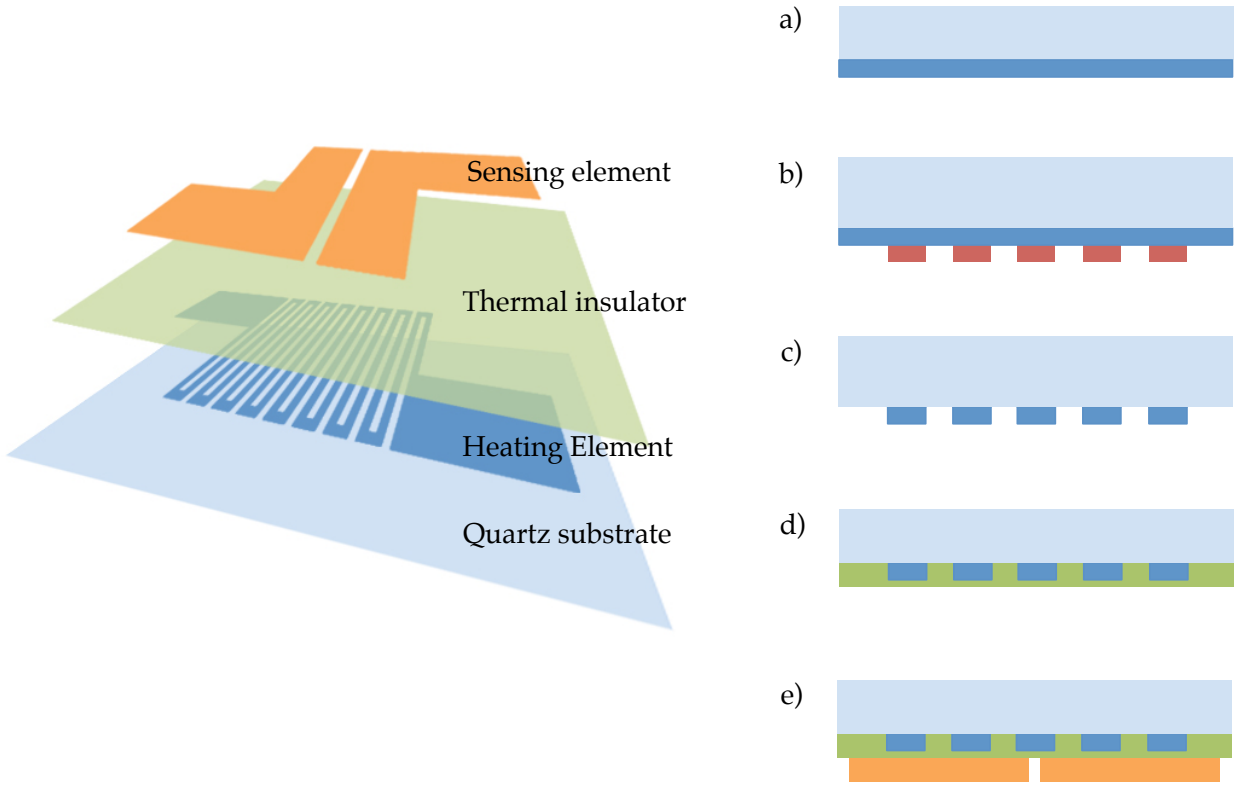

Figure 3.14 The proposed fabrication process involves *a*) photolithographic patterning of a serpentine heating element on glass substrate, *b*) conformal coating with a thermally insulating thin film, and *c*) shadow evaporation of the sensing element.

between the pads and the glass substrate. Two pairs of probes are needed to operate the device: one pair connected to a power supply to provide Joule heating of a serpentine-shaped microheater, denoted in blue, and another connected to a multimeter to monitor the overall resistance change of the device, denoted in orange. A thermally insulating thin film separates the heating and sensing elements. The proposed fabrication process is depicted in **Fig. 3.14**. The heating element is directly formed on the glass substrate *via* photolithographic patterning followed by conformal deposition of the insulating film. Finally, the sensing element is deposited *via* shadow evaporation.

3.5.2 Heat Transfer Model

As a result of the SiO_2 thin film and Au sensing element, energy from the polysilicon heating element will be dissipated in these films, and the temperature of the polysilicon microheater may be significantly different from the temperature of the sensing element, which transfers heat into the nanowires primarily by thermal conduction. It would be helpful, therefore, to calculate the temperature change across the SiO_2 and Au layers and determine the temperature needed at the polysilicon heater in order to obtain a temperature of 250 °C at the surface of the sensing element. A depiction of the system as a thermal resistance network is provided in **Fig. 3.15**. Each film is represented by a resistance, as denoted below each resistor in the network,

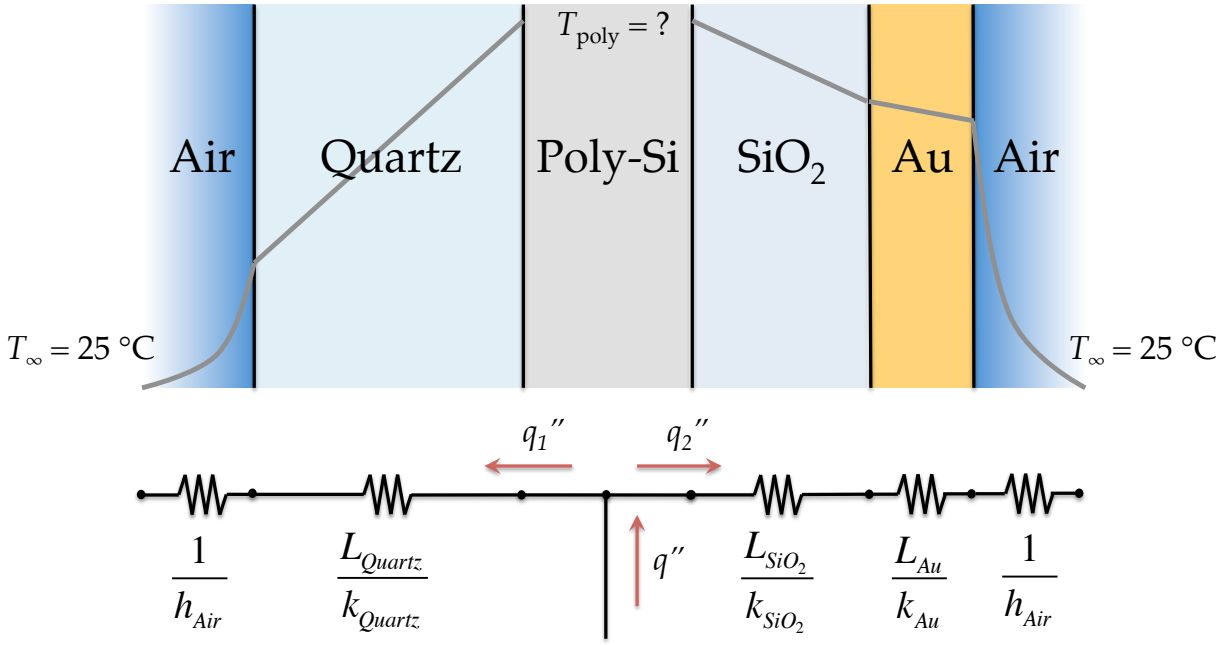

Figure 3.15 Thermal resistance network representation of the microheater consisting of resistance contributions from the air, quartz substrate, polysilicon microheater, SiO_2 insulating thin film, and Au sensing element. The value of each resistor is denoted below each resistor in the network.

and the directions of q_1'' and q_2'' indicate the conduction of heat away from the polysilicon heater, which is heated by the flow of electrical current along the narrow path of the serpentine structure. Air at room temperature brackets the device above and below, directing heat away from the microheater *via* thermal convection. Applying conversation of energy and understanding that the heat flux q_2'' is ultimately dissipated from the surface of the Au sensing element, thermal convection into the air can be analogized to Ohm's law, $V = IR$ of electrical circuit analysis. The driving force across the resistor is represented by the temperature difference; this is analogous to the potential difference across a resistor when analyzing electrical circuits. As for the resistance of convection, this is given by $1/h_{air}$. Lastly, what is transferred through this resistor is heat flux, which is analogous to electrical current. Matching each parameter to its electrical circuit analog and using the formula $I = V/R$, the heat flux q_2'' can be written:

$$q_2'' = \frac{250\ °C - T_\infty}{\frac{1}{h_{air}}} \tag{3.9}$$

In order to determine the temperature of the polysilicon microheater, the same analysis is performed across the SiO_2 and Au thin films. For SiO_2 and Au thin film thicknesses of 500 nm each, T_∞ = 25 °C, h_{air} = 100 W m^{-2} K^{-1}, k_{SiO2} = 1.28 W m^{-1} K, and k_{Au} = 310 W m^{-1} K, the temperature of the polysilicon microheater T_{poly} can be evaluated:

$$T_{poly} = q_2'' \left(\frac{L_{SiO_2}}{k_{SiO_2}} + \frac{L_{Au}}{k_{Au}} \right) + 250\ °C = 250.01\ °C \tag{3.10}$$

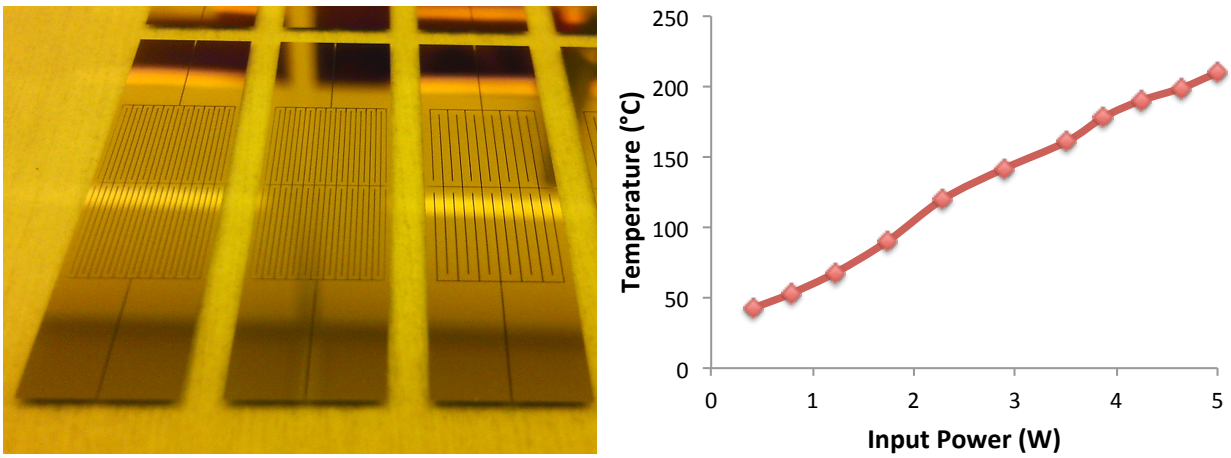

Figure 3.16 Prototype microheaters consisting of Ti/Au deposited on a quartz wafer (*left*). Surface temperature as a function of input power was plotted for the rightmost heater (*right*).

This result reveals that the temperature difference across the SiO_2 thin film and Au sensing element is quite minimal, and the temperature of the polysilicon microheater is virtually identical to the temperature of the surface of the Au sensing element in direct contact with the CuO nanowires.

3.5.3 Microheater Temperature Considerations

As a first step, simplified heaters without the sensing element and thermally insulating thin film were fabricated in the interest of characterizing the surface temperature as a function of input power according to the width of the serpentine heater. A lift-off process was performed to pattern Ti/Au heaters of 200 nm in thickness on a quartz wafer as shown in **Fig. 3.16**. As current and voltage were incrementally increased, the resulting temperature on the surface of the heaters was monitored with a thermocouple until the temperature stabilized. For input power of ~4.6 W, the temperature was measured to be 200 °C. Given that the thermal conductivity at room temperature for Au is 318 $W \cdot m^{-1} \cdot K^{-1}$ compared to 30 – 35 $W \cdot m^{-1} \cdot K^{-1}$ for heavily doped LPCVD polysilicon,[70] a heater of the same geometry and thickness made of polysilicon will demand much larger power input. With this consideration, subsequent heater designs should have serpentine structures with decreased cross-sectional area; a simple way to achieve this is to reduce the thickness of the deposited film.

While this microheater-integrated device poses greater sophistication compared to the original device without microheater, many of the desirable characteristics of the original device remain intact. The nanowires are electrically accessed as before by simply affixing the microheater-contact pad assembly atop the nanowires. Large areas of the nanowire array are still harnessed, giving rise to greater yield than existing single nanowire-based devices. Moreover, the microheater-contact pad assembly is reusable, allowing batch characterization of nanowire arrays using only one assembly. Lastly, this device architecture remains compatible with all nanowire materials anchored to an electrically conductive substrate.

The incorporation of heating introduces new challenges. Existing gas sensing devices with integrated heating usually place the sensing material and heating element in intimate contact

to ensure efficient heat transfer. In the microheater-integrated CuO H_2 sensor, contact between the sensing element and nanowires is limited only to the tips of the nanowires. Additionally, there is considerable volume surrounding the nanowires for incoming gas species to be heated and pass through without absorbing and reacting with any nanowires, resulting in heating losses. For this reason, the disadvantage of this device architecture is inefficient heating of the sensing material.

A possible remedy to reduce power consumption is to monitor and analyze the transient response of the device rather than the steady-state response. Increasing concentrations of impinging gas species should result not only in larger steady-state resistance, but also more rapid rates of increase and decrease in the transient stage. If it is sufficient to analyze only the transient response and correlate the rate of increase to the concentration of gas species, the steady-state response should then be redundant. Therefore, rather than continuously provide heating to the nanowires for the entire duration of operation, it would be sufficient to supply heating only in periodic pulses, and the fraction of power saved can be controlled by the duty cycle. For instance, pulses lasting only microseconds for every second elapsed would result in a thousandfold decrease in power consumption. Although the range of input power for the prototype Ti/Au heaters of **Fig. 3.16** is unacceptably large, efforts to simultaneously optimize the heater film thickness, serpentine geometry, and heating duty cycle will reduce power consumption to levels comparable to state-of-the-art low power gas sensing devices.

3.6 Conclusions

The results presented here validate the promise of this gas sensing device architecture and are worth summarizing. This facile assembly process allows for the utilization of semiconductor nanowires as-grown, directly on the growth substrate. The yield is very good compared to existing technologies, which are susceptible to varying electrical properties from nanowire to nanowire and the difficulty of forming ohmic contacts. The *I-V* characteristic obtained for this device shows ohmic response, suggesting good electrical contact between the pads and the nanowires. The recovery time for this device is excellent, on the order of 0.5 min. Of all the advantages of this architecture, the most intriguing of all is its versatility, which makes this technology applicable to all nanowire materials grown on conductive substrates. Therefore, any number of gas sensitive semiconducting nanowire-based materials can be harvested using this device scheme. For the particular example of CuO nanowire H_2 gas sensors, the overall device assembly is extremely simple. Following a thermal oxidation of Cu foil in ambient air at 500 °C, the device is completed with the application of the top contact pads. As such, this device scheme proves that nanowires can be integrated into gas sensors without expensive, laborious fabrication methods. The possibility of integrating microheaters into the device for localized Joule heating opens up even more possibilities for devices requiring operation at elevated temperatures. In the very least, these results will hopefully encourage more creative approaches toward harnessing the sensitivity of nanowires for cost-effective nanowire-based gas sensors with facile assembly methods.

Chapter 4: Conclusions and Future Work

4.1 Conclusions

4.1.1 Electrocatalysis

The copper oxide based photocathodes obtained *via* thermal oxidation of Cu foils exhibited anomalously large photocurrent without the addition of co-catalyst nanoparticles. For a basis of comparison, the planar Cu_2O photocathodes exhibited larger photocurrent than any reported in the literature. The large photocurrent was attributed to a high degree of crystallinity in the copper oxide films as well as higher carrier concentration, leading to more pronounced band bending at the semiconductor-electrolyte interface, and therefore more efficient transfer of electrons into the electrolyte. Although the performance was not retained after the deposition of a passivating thin film of TiO_2, the large photocurrent of the pristine, planar Cu_2O photocathodes is worth revisiting. The achievement of large photocurrent means there is a large supply of electrons that can be used productively toward the reduction of water to H_2. To carry this work further, a method of rapidly and efficiently shuttling these electrons out of the semiconductor in order to prevent charge recombination and Cu_2O photocorrosion should result in solar to hydrogen conversion efficiencies more closely matching the theoretical maximum conversion efficiency of 18%.

Copper oxide thin films achieved through thermal oxidation of Cu foils served as suitable precursors to CO_2 reduction as Cu reaction sites were recovered during electrochemical reduction of the copper oxides to Cu. The proportion of the reaction products CO, H_2, HCOOH, and CH_3COOH was observed to be dependent on the surface morphology of the oxidized Cu foil, which are in turn dictated by thermal oxidation temperature and time. CO production was more significant when oxidation time was extended from 0.5 to 10 hr at a temperature of 300 °C, and CO dominated over H_2 when temperature was increased to 500 °C. The flexibility of tuning the proportions of reaction products based on the copper oxide growth conditions opens up the possibility that undesired products may be suppressed while desired products may be bolstered. This controllable tuning of liquid fuel products lends copper oxide greater versatility for CO_2 reduction than previously thought, and future studies should elucidate the degree to which these products can be selectively produced in order to address the longstanding problem of low selectivity. For the moment, the dominant production of H_2 and CO gases makes this material an attractive candidate for syngas production.

4.1.2 Gas Sensing

Vertically-aligned CuO nanowire arrays were implemented in a novel gas sensing architecture that harnessed the sensitivity of nanowires while circumventing many laborious, expensive fabrication steps that are common to single-nanowire gas sensing devices. As a result, as-grown nanowire arrays can be integrated into devices immediately. While all nanowire-based gas sensing devices to date invariably require photolithography to pattern metal contacts, this technology bypasses this step completely. Moreover, this architecture can be applied to all nanowire materials anchored to an electrically conductive substrate as well as any other

applications that would benefit from facile device integration of nanowire materials. Despite its simplicity, the CuO nanowire array H_2 sensors employing this facile contact method demonstrated performance exceeding or matching reports in the literature. This demonstration should hopefully encourage more creative approaches toward harnessing nanowire materials for gas sensing as well as other applications.

The integration of microheaters underneath the sensing element opens up a wide range of possibilities for applications. Heating introduced locally and directed to the relevant materials means that these devices can be operated independent of larger heating sources. For gas sensing application alone, localized heating enabled by microheaters allows for the detection of a greater diversity of gas species.

4.2 Future Work

4.2.1 Characterization of Carrier Transport Properties in Cu_2O and CuO

The large photocurrent observed for photocatalytic water splitting suggests that the electronic material properties of Cu_2O *via* thermal oxidation are superior to those of prior work on Cu_2O synthesized by other methods. It is believed that the higher synthesis temperatures and

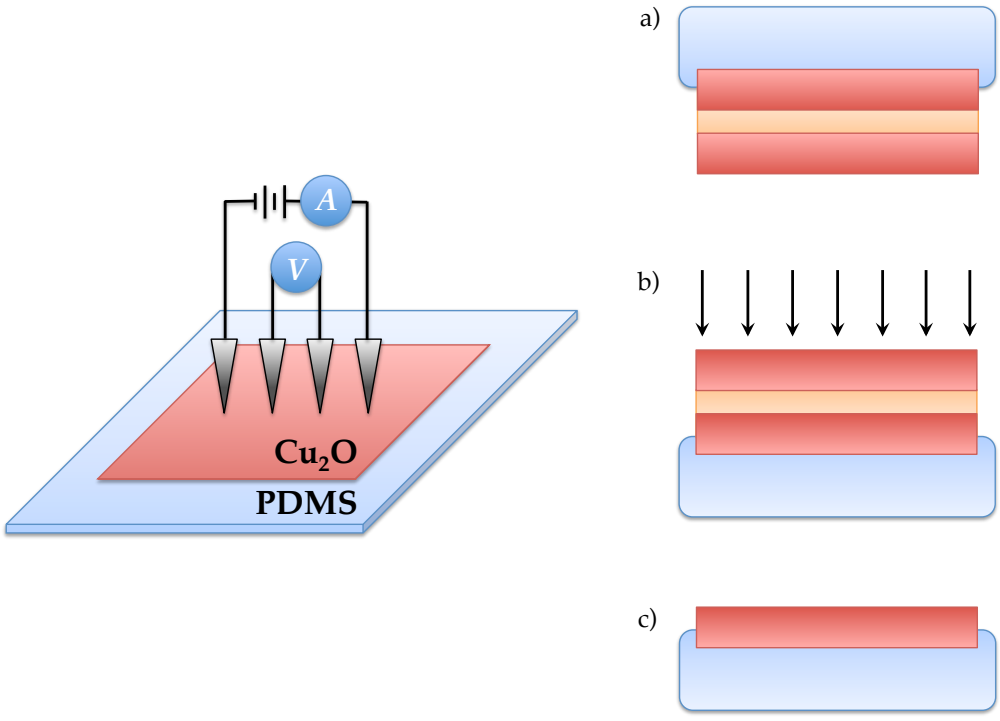

Figure 4.1 Process flow for a Cu_2O thin film adhered to a PDMS substrate for four-probe resistivity and Hall voltage measurements to evaluate Hall mobility. (*a*) PDMS is deposited onto one side of an oxidized Cu foil. (*b*) The back side is gradually milled away with an ion mill through the exposed Cu_2O film and the sandwiched Cu layer. (*c*) The final device retains only one Cu_2O film on the PDMS substrate.

choice of Cu foil as the starting material lead to higher crystallinity and therefore longer minority carrier diffusion length and larger carrier mobility. Moreover, the high carrier concentration measured *via* Mott-Schottky analysis indicates an enhanced electric field on the surface of the semiconductor for improving electron transfer into the electrolyte. Since no prior work has investigated the electronic material properties of Cu_2O derived from thermally-oxidized Cu foil, it would be beneficial to perform such a study for future work. More specifically, understanding the dependence of these electronic properties on the thermal oxidation duration and temperature used to prepare the Cu_2O photocathodes will help explain the current photocurrent results. Priming the Cu_2O thin film for a four-point probe system would allow measurements of resistivity and Hall voltage, which give rise to Hall mobility and carrier concentration calculations.

The challenge of preparing Cu_2O for the four-point probe system is to isolate this film from the Cu substrate. Otherwise, measurements performed on Cu_2O with the supporting Cu substrate intact will also receive contributions from Cu. A proposed process flow for the isolation of Cu_2O thin films is shown in **Fig. 4.1**. A layer of polydimethylsiloxane (PDMS) is poured on one side of the oxidized Cu foil and cured; the PDMS ultimately serves as the supporting substrate for the final device. The exposed surface is then gradually milled away using an ion mill to remove both the Cu_2O layer and the Cu layer. All that remains at the conclusion of this step is a Cu_2O thin film adhered to a PDMS substrate.

4.2.2 Graphene-protected Cu_2O for Stable Photocatalytic Water Splitting

Protective thin films of TiO_2 are the most commonly implemented solution to improving the long-term stability of Cu_2O photocathodes for photocatalytic water splitting. Most reports show perfect stability for TiO_2 films of thickness exceeding 20 nm.[35, 36] However, this stability

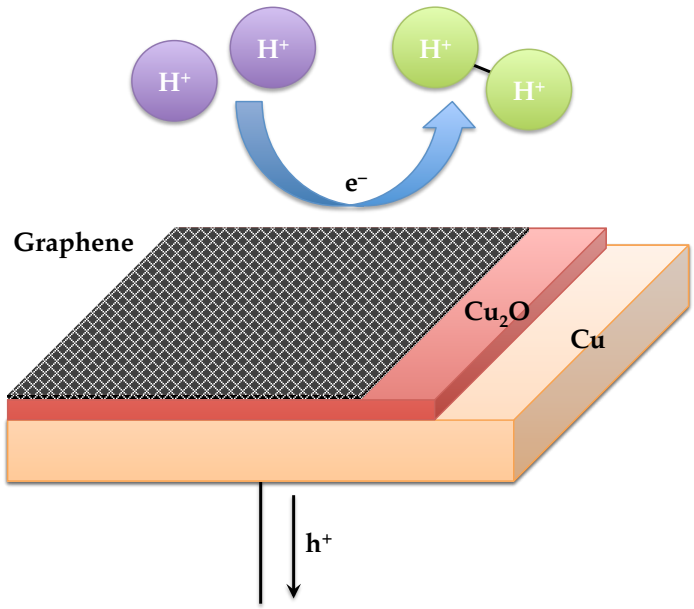

Figure 4.2 Proposed graphene-protected Cu_2O photocathodes.

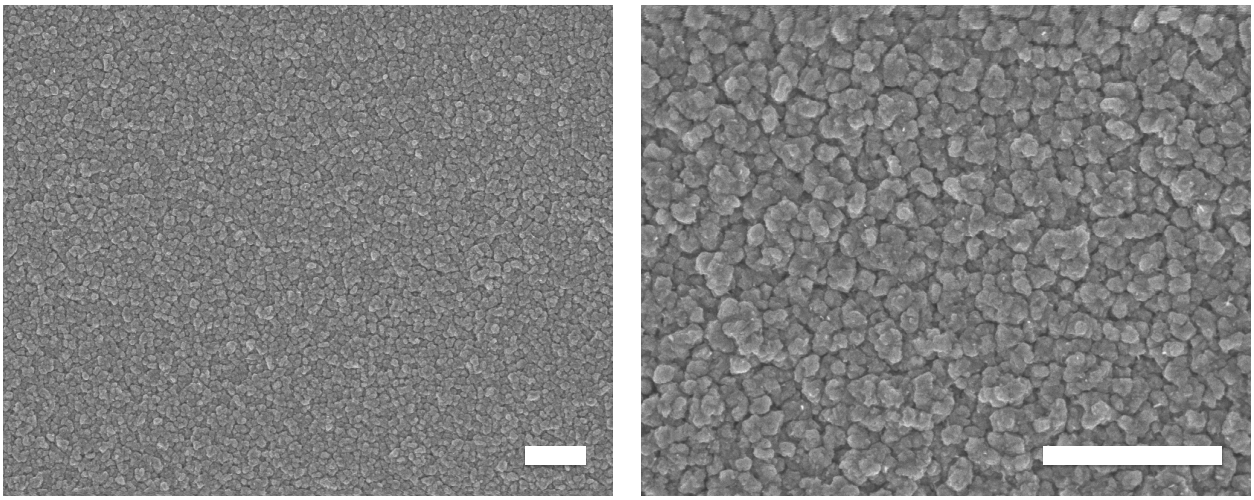

Figure 4.3 SEM micrograph of Cu_2O surface following thermal oxidation of Cu foil at 300 °C for 0.5 hr. Scale bar: 1 μm.

improvement does not come freely: the TiO_2 contributes an additional resistance to the photoelectrochemical cell, and Ti^{3+} trap states in the film eliminate electrons shuttling towards the electrolyte. Ultimately, the stability improvement coincides with a significant reduction in photocurrent. Only in the case of Paracchino *et al*. was the photocurrent enhanced, but the passivation strategy involved five stacks of alternating ZnO and Al_2O_3 thin films coated by a final thin film of TiO_2.[7] Clearly, a simple solution that maintains the high photoactivity of Cu_2O while affording perfect stability remains a challenge.

Zhang *et al*. took a different approach using carbon thin film coatings of 20 nm. Through glucose dip-coating of electrochemically anodized Cu followed by thermal annealing in N_2 atmosphere, Cu_2O nanowires protected by carbon thin film were synthesized. The protected photocathodes exhibited a photocurrent increase from –2.28 to –3.95 mA/cm^2 and a noteworthy stability increase from 12.6% to 80.7%. The photocurrent improvement was attributed to the excellent electrical conductivity of the carbon thin film, which enabled efficient transfer of electrons from Cu_2O into the electrolyte.[41]

A possible improvement upon this approach is to use even thinner carbon films to minimize optical absorption losses. Such films already exist naturally in the form of atomically-thin sheets of carbon: graphene. Since this form of carbon also exhibits extremely high electrical conductivity and electron mobility, it should further enhance the transfer of electrons from the Cu_2O photocathode. An overall device schematic is depicted in **Fig. 4.2** showing the individual layers comprising the device.

Achieving good conformity between the graphene layer and the Cu_2O surface will be challenging. The literature abounds with reports describing graphene transfer onto atomically flat surfaces.[72, 73] Unfortunately, the surface emerging from thermally oxidized Cu contains particles with diameter of several micrometers as shown in **Fig. 4.3**. Interfacing single-layer graphene onto such a surface may lead to poor adhesion and even complete delamination. As a result, graphene transfer may not be a suitable option for achieving good adhesion between graphene and Cu_2O.

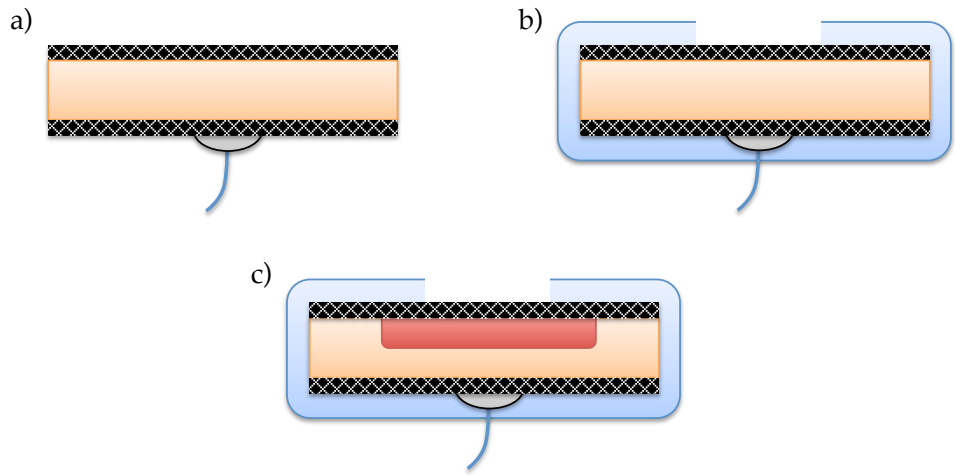

Figure 4.4 Process flow for conversion of graphene on Cu substrate to graphene-protected Cu_2O photocathode. *a*) Electrical wire is attached to the backside with Ag paste, *b*) the foil is masked with epoxy except for a 0.5 cm^2 window where the Cu will be oxidized, and *c*) the Cu is oxidized in 0.1 M KOH at constant current.

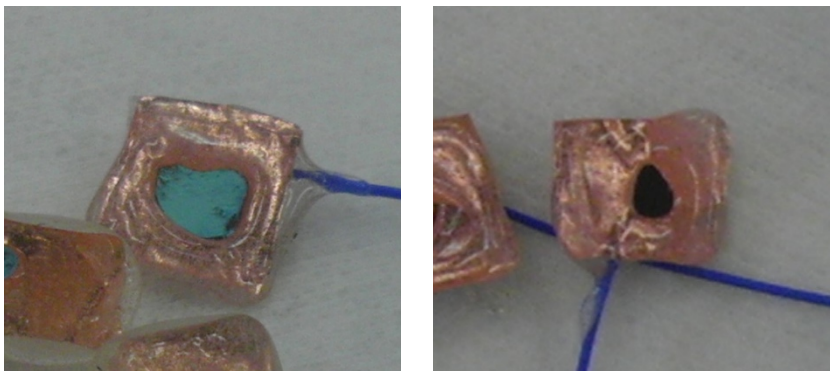

Figure 4.5 Photograph of Cu samples after electrochemical oxidation at constant current densities of 10 (*left*) and 5 (*right*) mA/cm^2, yielding $Cu(OH)_2$ and copper oxide, respectively.

Alternatively, graphene growth on Cu foil may present a possible synthesis pathway that circumvents an additional graphene transfer process. The uncertainty of this strategy lies in finding a process for converting the underlying Cu substrate into Cu_2O without perturbing the protective graphene layer. Thermal oxidation of graphene-covered Cu would likely be ineffective, as it is well known that graphene serves as a corrosion barrier on Ni and Cu.[74] Electrochemical methods have been used to oxidize bare Cu, and it is unknown whether graphene will act similarly in protecting Cu in a reducing aqueous environment as no such studies have been reported.

A proposed process flow using graphene on Cu substrate as a starting point is shown in **Fig. 4.4**. Electrical wire is attached to the underside graphene layer with Ag paste; this serves as the back electrode for both Cu oxidation and subsequent photoelectrochemical testing. Epoxy is applied to seal all regions of the electrode except for a small window to allow electrolyte contact.

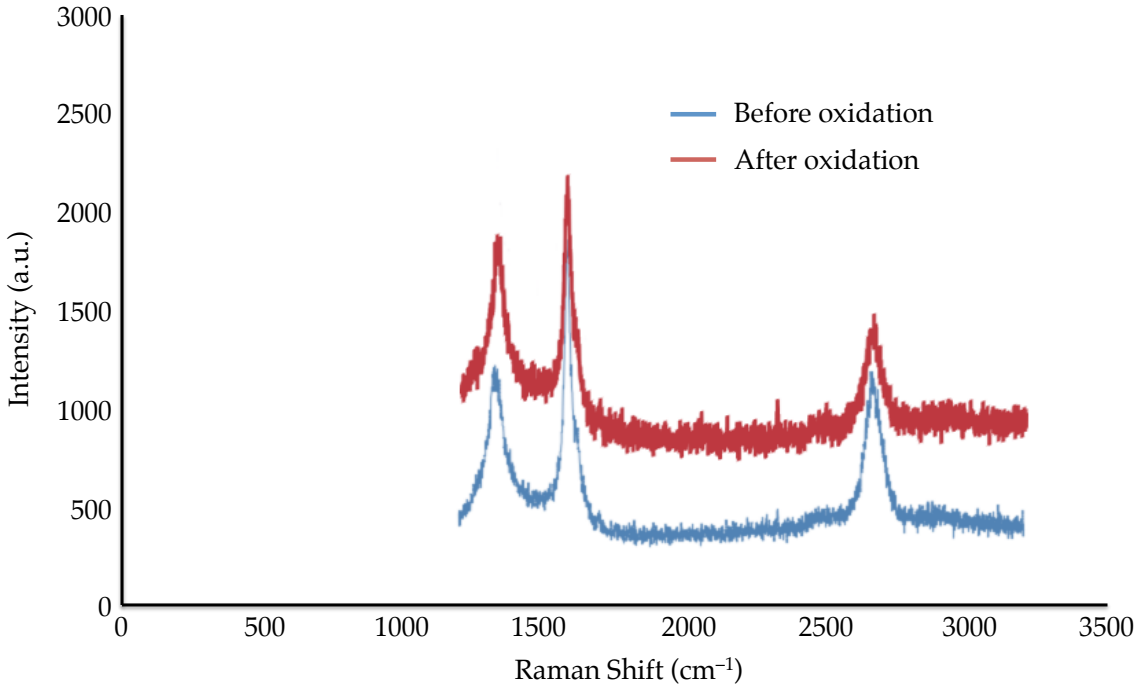

Figure 4.6 Raman spectra for graphene before and after electrochemical oxidation of graphene-covered Cu at 1.5 mA.

The sample is immersed in KOH electrolyte for electrochemical oxidation and then transferred into Na_2SO_4 electrolyte for photoelectrochemical testing. Finally, to confirm the quality of the graphene following oxidation, Raman spectra is gathered and compared against the spectra before oxidation. The features of interest in the Raman spectra are the D-line (1350 cm^{-1}) and G-line (1580 cm^{-1}) peaks; the quality of the graphene is likely preserved if these peaks retain their intensity after oxidation. Notwithstanding, chronopotentiometry under illumination will also directly reveal the performance and stability of the graphene covered Cu_2O photocathodes.

Preliminary electrochemical oxidation results reveal that Cu is indeed vulnerable to oxidation even in the presence of a graphene barrier. One sample oxidized at a fixed current density of 10 mA/cm^2 yielded an aqua green tone as shown in **Fig. 4.5**, characteristic of copper(II) hydroxide, $Cu(OH)_2$. According to previous reports, a larger current density is needed to form $Cu(OH)_2$ compared to Cu_2O and CuO.[41] In light of this, another oxidation was performed at 5 mA/cm^2, resulting in a uniformly dark surface reminiscent of CuO. Further elemental characterization will be needed to verify that the surface is indeed stoichiometric CuO. In the very least, this result confirms that Cu can be electrochemically modified even in the presence of graphene. Moreover, Raman spectra obtained after electrochemical oxidation, shown in **Fig. 4.6**, confirm that the graphene retains its quality: the D-line (1350 cm^{-1}) and G-line (1580 cm^{-1}) peaks appear to be the same height as the corresponding peaks prior to oxidation. These preliminary results show the feasibility and promise of electrochemical oxidation as a synthesis pathway towards creating graphene-covered Cu_2O photocathodes for efficient and stable photocatalytic water splitting.

References

1. Moskovits, M., Kolmakov, A. Chemical Sensing and Catalysis by One-Dimensional Nanostructures. Annual Review of Materials Research 34, 151-180 (2004).
2. Eranna, G., Joshi, B. C., Runthala, D. P., Gupta, R. P. Oxide Materials for Development of Integrated Gas Sensors—A Comprehensive Review. Critical Reviews in Solid State and Materials Sciences 29, 111-188 (2004).
3. Yuhas, B. D., Yang, P. Nanowire-Based All-Oxide Solar Cells. Journal of the American Chemical Society 131, 3756-3761 (2009).
4. You, H., Dai, Y., Zhang, Z., Ma, D. Improved performances of organic light-emitting diodes with metal oxide as anode buffer. Journal of Applied Physics 101, 026105 (2007).
5. Robertson, J. High dielectric constant gate oxides for metal oxide Si transistors. Reports on Progress in Physics 69, 327-396 (2006).
6. Hara, M., Kondo, T., Komoda, M., Ikeda, S., Shinohara, K., Tanaka, A., Kondo, J. N., Domen, K. Cu_2O as a photocatalyst for overall water splitting under visible light irradiation. Chemical Communications 3, 357-358 (1998).
7. Paracchino, A., Laporte, V., Sivula, K., Grätzel, M., Thimsen, E. Highly active oxide photocathode for photoelectrochemical water reduction. Nature Materials 10, 456-461 (2011).
8. Mittiga, A., Salza, E., Sarto, F., Tucci, M., Vasanthi, R. Heterojunction solar cell with 2% efficiency based on a Cu_2O substrate. Applied Physics Letters 88, 163502 (2006).
9. Switzer, J. A., Maune, B. M., Raub, E. R., Bohannan, E. W. Negative Differential Resistance in Electrochemically Self-Assembled Layered Nanostructures. The Journal of Physical Chemistry B 103, 395-398 (1999).
10. Bohannan, E. W., Huang, L.-Y., Miller, F. S., Shumsky, M. G., Switzer, J. A. In Situ Electrochemical Quartz Crystal Microbalance Study of Potential Oscillations During the Electrodeposition of Cu/Cu_2O Layered Nanostructures. Langmuir 15, 813-818 (1999).
11. Figueiredo, V., Elangovan, E., Goncalves, G., Barquinha, P., Pereira, L., Franco, N., Alves, E., Martins, R., Fortunato, E. Effect of post-annealing on the properties of copper oxide thin films obtained from the oxidation of evaporated metallic copper. Applied Surface Science 254, 3949-3954 (2008).
12. "Copper(I) oxide." Wikipedia: The Free Encyclopedia. Wikimedia Foundation (accessed December 2, 2013).
13. "Copper(II) oxide." Wikipedia: The Free Encyclopedia. Wikimedia Foundation (accessed December 2, 2013).
14. de Jongh, P. E., Vanmaekelbergh, D., Kelly, J. J. Photoelectrochemistry of electrodeposited Cu_2O. Journal of the Electrochemical Society 147, 486-489 (2000).
15. Sculfort, J. L., Guyomard, D., Herlem, M. Photoelectrochemical characterization of the p-Cu_2O-non aqueous electrolyte junction. Electrochimica Acta 29, 459-465 (1984).
16. Lin, Y., Yuan, G., Sheehan, S., Zhou, S., Wang, D. Hematite-based solar water splitting: challenges and opportunities. Energy and Environmental Science 4, 4862-4869 (2011).
17. Kaur, M., Muthe, K. P., Despande, S. K., Choudhury, S., Singh, J. B., Verma, N., Gupta, S. K., Yakhmi, J. V. Growth and branching of CuO nanowires by oxidation of copper. Journal of Crystal Growth 289, 670-675 (2006).

18. Gou, L., Murphy, C. J. Solution-Phase Synthesis of Cu_2O Nanocubes. Nano Letters 3, 231-234 (2003).
19. Wang, W., Wang, G., Wang, X., Zhan, Y., Liu, Y., Zheng, C. Synthesis and Characterization of Cu_2O Nanowires by a Novel Reduction Route. Advanced Materials 14, 67-69 (2002).
20. Taneja, P., Chandra, R., Banerjee, R., Ayyub, P. Structure and Properties of Nanocrystalline Ag and Cu_2O Synthesized by High Pressure Sputtering. Scripta Materialia 44, 1915-1918 (2001).
21. Hong, Z.-S., Cao, Y., Deng, J.-F. A convenient alcohothermal approach for low temperature synthesis of CuO nanoparticles. Materials Letters 52, 34-38 (2002).
22. Balamurugan, B., Mehta, B. R., Shivaprasad, S. M. Surface-modified CuO layer in size-stabilized single-phase Cu_2O nanoparticles. Applied Physics Letters 79, 3176-3178 (2001).
23. Borzi, R. A., Stewart, S. J., Mercader, R. C., Punte, G., Garcia, F. Magnetic behavior of nanosized cupric oxide. Journal of Magnetism and Magnetic Materials 226-230, 1513-1515 (2001).
24. Zhou, G., Yang, J. C. Temperature effect on the Cu_2O oxide morphology created by oxidation of Cu(0 0 1) as investigated by in situ UHV TEM. Applied Surface Science 210, 165-170 (2003).
25. Xu, C., Woo, C., Shi, S. Formation of CuO nanowires on Cu foil. Chemical Physics Letters 399, 62-66 (2004).
26. Matsumura, H., Fujii, A., Kitatani, T. Properties of High-Mobility Cu_2O Films Prepared by Thermal Oxidation of Cu at Low Temperatures. Japanese Journal of Applied Physics 35, 5631-5636 (1996).
27. Lewis, N. S., Nocera, D. G. Powering the planet: chemical challenges in solar energy utilization. Proceedings of the National Academy of Sciences U S A 103, 15729-15735 (2006).
28. Lewis, N. S., Crabtree, G. Basic Research Needs for Solar Energy Utilization: report of the Basic Energy Sciences Workshop on Solar Energy Utilization, April 18-21, 2005. US Department of Energy, Office of Basic Energy Science, Washington, DC (2005).
29. U.S. Energy Information Administration, Electric Power Monthly, March 2013.
30. Kim, J. Y., Magesh, G., Youn, D. H., Jang, J.-W., Kubota, J., Domen, K., Lee, J. S. Single-crystalline, wormlike hematite photoanodes for efficient solar water splitting. Scientific Reports 3 (2013).
31. Kronawitter, C. X., Vayssieres, L., Shen, S., Guo, L., Wheeler, D. A., Zhang, J. Z., Antoun, B. R., Mao, S. S. A perspective on solar-driven water splitting with all-oxide hetero-nanostructures. Energy and Environmental Science 4, 3889-3899 (2011).
32. Liu, M., de Leon Snapp, N., Park, H. Water photolysis with a cross-linked titanium dioxide nanowire anode. Chemical Science 2, 80-87 (2011).
33. Wang, G., Wang, H., Ling, Y., Tang, Y., Yang, X., Fitzmorris, R. C., Wang, C., Zhang, J. Z., Li, Y. Hydrogen-Treated TiO_2 Nanowire Arrays for Photoelectrochemical Water Splitting. Nano Letters 11, 3026-3033 (2011).
34. Ding, C., Shi, J., Wang, D., Wang, Z., Wang, N., Liu, G., Xiong, F., Li, C. Visible light driven overall water splitting using cocatalyst/$BiVO_4$ photoanode with minimized bias. Physical Chemistry Chemical Physics 15, 4589-4595 (2013).

35. Ma, L., Lin, Y., Wang, Y., Li, J., Wang, E., Qiu, M., Yu, Y. Aligned 2-D Nanosheet Cu_2O Film: Oriented Deposition on Cu Foil and Its Photoelectrochemical Property. Journal of Physical Chemistry C 112, 18916-18922 (2008).
36. Huang, Q., Kang, F., Liu, H., Li, Q., Xiao, X. Highly aligned $Cu_2O/CuO/TiO_2$ core/shell nanowire arrays as photocathodes for water photoelectrolysis. Journal of Materials Chemistry A 1, 2418-2425 (2013).
37. Zhang, Z., Wang, P. Highly stable copper oxide composite as an effective photocathode for water splitting *via* a facile electrochemical synthesis strategy. Journal of Materials Chemistry 22, 2456-2464 (2012).
38. Hashimoto, K., Irie, H., Fujishima, A. TiO_2 Photocatalysis: A Historical Overview and Future Prospects. Japanese Journal of Applied Physics 44, 8269-8285 (2005).
39. Chen, S., Wang, L.-W. Thermodynamic Oxidation and Reduction Potentials of Photocatalytic Semiconductors in Aqueous Solution. Chemistry of Materials 24, 3659-3666 (2012).
40. Sunkara, S., Vendra, V. K., Kim, J. H., Druffel, T., Sunkara, M. K. Scalable synthesis and photoelectrochemical properties of copper oxide nanowire arrays and films. Catalysis Today 199, 27-35 (2013).
41. Zhang, Z., Dua, R., Zhang, L. Zhu, H., Zhang, H., Wang, P. Carbon-Layer-Protected Cuprous Oxide Nanowire Arrays for Efficient Water Reduction. ACS Nano
42. Murphy, A. B., Barnes, P. R. F., Randeniya, L. K., Plumb, I. C., Grey, I. E., Horne, M. D., Glasscock, J. A. Efficiency of solar water splitting using semiconductor electrodes. International Journal of Hydrogen Energy 31, 1999-2017 (2006).
43. Hagfeldt, A., Björkstén, U., Grätzel, M. Photocapacitance of Nanocrystalline Oxide Semiconductor Films: Band-Edge Movement in Mesoporous TiO_2 Electrodes during UV Illumination. Journal of Physical Chemistry 100, 8045-8048 (1996).
44. Nosaka, Y., Norimatsu, K., Miyama, H. The Function of Metals in Metal-Compounded Semiconductor Photocatalysts. Chemical Physics Letters 106, 128-131 (1984).
45. Lewis, N. S. Chemical control of charge transfer and recombination at semiconductor photoelectrode surfaces. Inorganic Chemistry 44, 6900-6911 (2005).
46. Sekizawa, M., Kudo, A. Photocatalytic H_2 evolution under visible light irradiation on Ni-doped ZnS photocatalyst. Chemical Communications 15, 1371-1372 (2000).
47. Maeda, K., Domen, K. Photocatalytic water splitting: recent progress and future challenges. Journal of Physical Chemistry Letters 1, 2655-2661 (2010).
48. Forgie, R., Bugosh, G., Neyerlin, K. C., Liu, Z., Strasser, P. Bimetallic Ru Electrocatalysts for the OER and Electrolytic Water Splitting in Acidic Media. Electrochemical and Solid State Letters 13, B36-39 (2010).
49. Chen, X., Liu, L., Yu, P. Y., Mao, S. S. Increasing Solar Absorption for Photocatalysis with Black Hydrogenated Titanium Dioxide Nanocrystals. Science 11, 746-750 (2011).
50. Hand, M. M., Baldwin, S., DeMeo, E., Reilly, J. M., Mai, T., Arent, D., Porro, G., Meshek, M., Sandor, D. Renewable Electricity Futures Study. National Renewable Energy Laboratory (2012).
51. Monastersky, R. Global carbon dioxide levels near worrisome milestone. Nature 497, 13-14 (2013).
52. Hori, Y., Wakebe, H., Tsukamoto, T., Koga, O. Electrocatalytic Process of CO Selectivity in Electrochemical Reduction of CO_2 at Metal Electrodes in Aqueous Media. Electrochimica Acta 39, 1833-1839 (1994).

53. Li, C. W., Kanan, M. W. CO_2 Reduction at Low Overpotential on Cu Electrodes Resulting from the Reduction of Thick Cu_2O Films. Journal of the American Chemical Society 134, 7231-7234 (2012).
54. Chen, Y., Li, C. W., Kanan, M. W. Aqueous CO_2 Reduction at Very Low Overpotential on Oxide-Derived Au Nanoparticles. Journal of the American Chemical Society 134, 19969-19972 (2012).
55. Li, W. "Electrocatalytic reduction of CO_2 to small organic molecule fuels on metal catalysts." ACS Advances in CO_2 Conversion and Utilization. Ed. Yun Hang Hu (2010).
56. Kumar, B., Smieja, J. M., Sasayama, A. F., Kubiak, C. P. "Tunable, light-assisted co-generation of CO and H_2 from CO_2 and H_2O by Re(bipy-tbu)$(CO)_3$Cl and p-Si in non-aqueous medium." Chemical Communications 48, 272-274 (2012).
57. Yamazoe, N. New approaches for improving semiconductor gas sensors. Sensors and Actuators B 5, 7-19 (1991).
58. Choi, K. J., Jang, H. W. One-Dimensional Oxide Nanostructures as Gas-Sensing Materials: Review and Issues. Sensors 10, 4083-4099 (2010).
59. Hoa, N. D., Quy, N. V., Tuan, M. A., Hieu, N. V. Facile synthesis of p-type semiconducting cupric oxide nanowires and their gas sensing properties. Physica E. 42, 146-149 (2009).
60. Mickelson, W., Sussman, A., Zettl, A. Low-power, fast, selective nanoparticle-based hydrogen sulfide gas sensor. Applied Physics Letters 100, 173110 (2012).
61. Wang, B., Zhu, L. F., Yang, Y. H., Xu, N. S., Wang, G. W. Fabrication of a SnO_2 Nanowire Gas Sensor and Sensor Performance for Hydrogen. Journal of Physical Chemistry C 112, 6643-6647 (2008).
62. Tien, L. C., Sadik, P. W., Norton, D. P., Voss, L. F., Pearton, S. J., Wang, H. T., Kang, B. S., Ren, F., Lin, J., Jun, J. Hydrogen sensing at room temperature with Pt-coated ZnO thin films and nanorods. Applied Physics Letters 87, 222106 (2005).
63. Rout, C. S., Krishna, S. H., Vivekchand, S. R. C., Govindaraj, A., Rao, C. N. R. Hydrogen and ethanol sensors based on ZnO nanorods, nanowires and nanotubes. Chemical Physics Letters 418, 586-590 (2006).
64. Varghese, O. K., Gong, D., Paulose, M., Ong, K. G., Dickey, E. C., Grimes, C. A. Extreme Changes in the Electrical Resistance of Titania Nanotubes with Hydrogen Exposure. Advanced Materials 15, 624-627 (2003).
65. Shukla, S., Seal, S., Ludwig, L, Parish, C. Nanocrystalline indium oxide-doped tin oxide thin film as low temperature hydrogen sensor. Sensors and Actuators B 97, 256-265 (2004).
66. Hoa, N. D., Quy, N. V., Jung, H., Kim, D., Kim, H., Hong, S.-K. Synthesis of porous CuO nanowires and its application to hydrogen detection. Sensors & Actuators B 146, 266-272 (2010).
67. Kim, Y.-S., Hwang, I.-S., Kim, S.-J., Lee, C.-Y., Lee, J.-H. CuO nanowire gas sensors for air quality control in automotive cabin. Sensors and Actuators B: Chemical 135, 298-303 (2008).
68. Serin, T., Yildiz, A., Horzum Sahin, S., Serin, N. Extraction of important electrical parameters of CuO. Physica B: Condensed Matter 406, 575-578 (2011).
69. Tsai, C.-M., Chen, G.-D., Tseng, T.-C., Lee, C.-Y., Huang, C.-T., Tsai, W.-Y., Yang, W.-C., Yeh, M.-S., Yew, T.-R. CuO nanowire synthesis catalyzed by a CoWP nanofilter. Acta Materialia 57, 1570-1576 (2009).

70. Tai, Y. C., Mastrangelo, C. H., Muller, R. S. Thermal Conductivity of Heavily Doped LPCVD Polysilicon. Electron Devices Meeting, 1987 International 33, 278-281 (1987).
71. Siripala, W., Ivanovskaya, A., Jaramillo, T. F., Baeck, S.-H., McFarland, E. W. A Cu_2O/TiO_2 heterojunction thin film cathode for photoelectrocatalysis. Solar Energy Materials and Solar Cells 77, 229-237.
72. Li, X., Cai, W., An, J., Kim, S., Nah, J., Yang, D., Piner, R., Velamakanni, A., Jung, I., Tutuc, E., Banerjee, S. K., Colombo, L., Ruoff, R. S. Large-Area Synthesis of High-Quality and Uniform Graphene Films on Copper Foils. Science 324, 1312-1314 (2009).
73. Bae, S., Kim, H., Lee, Y., Xu, X., Park, J.-S., Zheng, Y., Balakrishnan, J., Lei, T., Kim, H. R., Song, Y. I., Kim, Y.-J., Kim, K. S., Özyilmaz, B., Ahn, J.-H. Hong, B. H., Iijima, S. Roll-to-roll production of 30-inch graphene films for transparent electrodes. Nature Nanotechnology 5, 574-578 (2010).
74. Chen, S., Brown, L., Levendorf, M., Cai, W., Ju, S.-Y., Edgeworth, J., Li, X., Magnuson, C. W., Velamakanni, A., Piner, R. D., Kang, J., Park, J., Ruoff, R. S. Oxidation Resistance of Graphene-Coated Cu and Cu/Ni Alloy. ACS Nano 5, 1321-1327 (2011).